# A NEW MEMS APPROACH FOR SPIROMETERS

A THESIS SUBMITTED TO
THE GRADUATE SCHOOL OF NATURAL AND APPLIED SCIENCES
OF
MIDDLE EAST TECHNICAL UNIVERSITY

BY

SAHAR HABIBIABAD

IN PARTIAL FULFILLMENT OF THE REQUIREMENTS
FOR
THE DEGREE OF MASTER OF SCIENCE
IN
BIOMEDICAL ENGINEERING

FEBRUARY 2016

Approval of the thesis:

**A NEW MEMS APPROACH FOR SPIROMETERS**

submitted by **SAHAR HABIBIABAD** in partial fulfillment of the requirements for the degree of **Master of Science in Biomedical Engineering Department, Middle East Technical University** by,

Prof. Dr. Gülbin Dural Ünver
Dean, Graduate School of **Natural and Applied Sciences** _____

Prof. Dr. Işik Hakan Tarman
Head of Department, **Biomedical Engineering** _____

Assoc. Prof. Dr. Yeşim Serinağaoğlu
Supervisor, **Dept. of Electrical and Electronics Eng., METU** _____

Assist. Prof. Dr. Mustafa İlker Beyaz
Co-supervisor, **Dept. of Electrical and Electronics Eng., AIU** _____

**Examining Committee Members:**

Prof. Dr. Haluk Kulah
Dept. of Electrical and Electronics Eng., METU _____

Assoc. Prof. Dr. Yeşim Serinağaoğlu
Dept. of Electrical and Electronics Eng., METU _____

Assist. Prof. Dr. Mustafa İlker Beyaz
Dept. of Electrical and Electronics Eng., AIU _____

Prof. Dr. Tolga Ciloglu
Department of Electrical and Electronics Engineering, METU _____

Assist. Prof. Dr. Kivanc Azgin
Dept. of Mechanical Engineering, METU _____

**Date:** **18 Feb 2016**

**I hereby declare that all information in this document has been obtained and presented in accordance with academic rules and ethical conduct. I also declare that, as required by these rules and conduct, I have fully cited and referenced all material and results that are not original to this work.**

Name, Last Name: SAHAR HABIBIABAD

Signature :

# ABSTRACT

A NEW MEMS APPROACH FOR SPIROMETERS

Habibiabad, Sahar
M.S., Department of Biomedical Engineering
Supervisor : Assoc. Prof. Dr. Yeşim Serinağaoğlu
Co-Supervisor : Assist. Prof. Dr. Mustafa İlker Beyaz

February 2016, 102 pages

Measurement of breathing parameters is necessary for a variety of applications ranging from respiration monitoring to breathing-related diseases. In this respect, spirometry is one of the most common techniques used for Asthma and Chronic Obstructive Pulmonary Disease (COPD) patients to detect the type and extent of the lung malfunctions by monitoring the exhaled or inhaled air. The efforts in this work have been focused on the miniaturization of turbine-based spirometers using MEMS (Microelectromechanical Systems) technology for accurate spirometry analysis, improved portability, integration with portable electronics, and lower device cost. Accordingly, this thesis presents the design, simulation, and fabrication of the first turbine-based MEMS spirometer. This work will also enable seamless integration of the MEMS spirometer with cell phones for patient self-monitoring, as opposed to previous demonstrations of larger spirometer modules.

Keywords: Spirometer, MEMS

# ÖZ

SPİROMETRELERDE YENİ BİR MEMS YAKLAŞIMI

Habibiabad, Sahar
Yüksek Lisans, Biyomedikal Mühendisliği Bölümü
Tez Yöneticisi : Assoc. Prof. Yeşim Serinağaoğlu
Ortak Tez Yöneticisi : Yrd. Doç. Dr. Mustafa İlker Beyaz

Şubat 2016 , 102 sayfa

Solunum parametrelerinin ölçümü, solunum takibinden solunumla ilgili hastalıkların teşhisine kadar çok çeşitli uygulamalarda gereklidir. Soluk alıp vermenin izlenmesi ve ilgili parametrelerin ölçülmesi olarak tanımlanabilen spirometri, astım ve Kronik Obstrüktif Akciğer Hastalığı (KOAH) olan hastalarda akciğer sorunlarının türü ve ilerlemesinin tanısında kullanılan en yaygın tekniklerden biridir. Bu araştırmada, Miktoelektromekanik Sistemler (MEMS) teknolojisi kullanılarak türbinli spirometrelerin küçültmesi için çalışılmıştır. Çalışmada hedefler spirometrini analizlerinin doğruluğunu artırmak, taşınabilirliğini kolaylaştırmak, mobil elektrikli cihazlara bağlanabilirliğini sağlamak ve üretim maliyetini de azaltmaktır. Bu tezde ilk MEMS türbinli spirometrenin tasarım, simülasyon ve yapımı için yeni bir yaklaşım sunulmuştur. MEMS spirometreler, büyük boyutlu spirometrelerden farklı olarak gelecekte cep telefonlarına bağlanıp uzaktan hasta takibi yapılabilmesini de sağlayacaktır.

Anahtar Kelimeler: SPİROMETRE, MEMS

*To my parents for their unconditional love*

# ACKNOWLEDGMENTS

Foremost, I would like to express my sincere gratitude to my co-supervisor Dr. Mustafa Ilker Beyaz, whose patience, inspiration, enthusiasm and understanding, added considerably to my graduate experience. He has supported me not only by providing a research assistantship, but also academically and emotionally through the rough road to finish this thesis and reminding that research is fun and exciting in every single meeting we had. I have been amazingly fortunate to have an advisor who gave me the freedom to explore on my own and at the same time the guidance to recover when my steps faltered.

Similar profound gratitude goes to Dr. Yeşim Serinağaoğlu, without whose support I would not have the opportunity to work on my interested topic. Throughout my thesis-writing period, she provided encouragement, sound advice and good company.

I am grateful to Dr. Tayfun Akin for his valuable lecture that helped me to improve my knowledge in microfabrication.

I would like to acknowledge UNAM cleanroom staff, for trying to keep the fabrication facilities operating. And special mention goes to Semih Yaşar and Hakan Sürel for going far beyond the call of duty and their constant trust in my lab work. Appreciation also goes out to Murat Serhatlıoğlu, Talha Masood Khan, and Ersin Hüseyinoğlu, who provided a friendly and cooperative atmosphere at work. I should also thank my college Utku Göreke for his encouragement and practical advices.

I would like to thank The Scientific and Technological Research Council of Turkey (TÜBITAK) for the scholarship and support for me.

Many friends have helped me stay sane through the difficult times. I greatly value their friendship, comraderies, emotional supports, and for all the fun we have had during all these years. I wish to thank Greg Long, Atefeh Lafzi, and Fatemeh Soleimani, whose guidance helped me in all the time of writing this thesis. I am particularly indebted to Majid Biazaran, without whom I would not be able to prepare my thesis before deadlines.

I would like to express my deepest thankfulness and gratitude to my wonderful parents, Nahid Ahmadi and Mahmoud Habibiabad, and my sister, Sepideh Habibiabad. So much of my success is possible because of their endless love, support, and encouragement throughout my life, and for their faith in me. I owe so much to my parents for all of their sacrifice. Thanks to my sister who offered invaluable emotional support

and humor over the years. I could not ask for a better sister.

Last but not the least, I would like to thank my dearest, Reza Soleimani, for his continuous love, faith, and support, who constantly reminded me of life's most important values: "happiness, health, home, and self-confidence". His patience and support helped me overcome many crisis situations and finish this thesis.

# TABLE OF CONTENTS

APPENDICES

# LIST OF TABLES

TABLES

# LIST OF FIGURES

FIGURES

# CHAPTER 1

# INTRODUCTION

Chronic Obstructive Pulmonary Disease (COPD) and Asthma are two of the most common lung diseases worldwide. According to World Health Organization (WHO) estimates, 65 million people have moderate to severe COPD and 235 million people suffer from Asthma. Correspondingly, there is a growing demand for early diagnosis as well as appropriate treatments targeted at these diseases. One of the most common methods in diagnosing and following the progress of such lung diseases is spirometry, which is the practice of measuring exhaled or inhaled air to assess the type and extent of the lung malfunctions. There are variety types of commercial spirometers, which differ in size, performance, and price. The advanced spirometers are more accurate and capable of performing wide variety of tests. However, they are so expensive and can be only found in established health care facilities. There are also simpler spirometers with limited performance available in the market. These simple spirometers are cheaper compared to the advanced ones that can be considered for personal use. However, due to the fact that these diseases are prevalent mostly in highly-populated and low-income countries, there is a high demand for accurate devices but in much lower price. Furthermore, since remote monitoring can result in better medical services along with much less cost for government and patients, even high developed countries are in need of low-cost, reliable and portable spirometers.

The core component of a spirometer is the sensing unit that measures the spirometry parameters, i.e. air velocity and total air volume. Four main types of sensors have been used in spirometers so far, namely thermal sensors, differential pressure sensors, ultrasound sensors, and turbine-type sensors. Thermal sensors, also called hot wire

sensors, usually employ a hot metal or semiconductor piece that exchanges heat with the flowing gas [31]. The resulting temperature drop on the piece is proportional to the air velocity, allowing the measurement of multiple related parameters [32]. Although sensor linearity and accuracy are important advantages in this type of sensors, susceptibility to dust particles as well as ambient pressure severely limit their real-life performance. In addition, their inability to measure bidirectional gas flow due to their design nature prohibits the monitoring of inhalation and exhalation at the same time. Differential pressure sensors, on the other hand, take advantage of Bernoulli's principle, and indirectly determine the spirometry parameters by measuring the pressure difference along a tube with known fluidic resistance [13]. These sensors are bidirectional in nature, and show accurate results especially in low flow rates [13]. However, they are sensitive to temperature variations, and are prone to blockage by solid and liquid particles around the sensor vicinity [33],[34]. Ultrasound sensors are used in pairs located on the opposite sides of a flow tube, transmitting and receiving ultrasonic pulses [7]. The transit time of the acoustic waves is a function of the air velocity. Turbine sensors, on the other hand, operate based on a direct interaction between a rotary turbine and the flowing gas [35]. The resulting turbine rotation speed is a linear function of gas velocity and flow rate, from which the total air volume can be straightforwardly determined. In addition, the turbine based design allows for bidirectional operation while remaining insensitive to humidity, ambient temperature and pressure. A major challenge in this type of spirometers is the turbine rotational inertia problem.

We have adopted a new MEMS approach to turbine-based spirometers that is able to directly measure the velocity air volume. The turbine angular velocity will be detected magnetically by copper coils on the stators embedded on both sides of the rotor. This device would include all the advantages of present turbine sensors. In addition, using MEMS technology will help to decrease sensor cost and dimension. The main idea is to produce a spirophone [36] by connecting this small sensor to the phone that makes it much more portable, cheaper and highly accurate. Furthermore, since it is able to convert the energy of respiration to electrical energy, self-powering is another outstanding feature of this device. This feature enables to use the spirometer whenever and anywhere without worry of recharge or change the batteries.

In summary, scope of the thesis can be defined as:

- Designing the stator coils and magnets.
- Optimizing the pole number using COMSOL simulation file obtained from Dr. Beyaz.
- Designing the turbine blades by Utku Goreke
- Designing the stator masks using AutoCAD
- Microfabrication of the stators
- Testing the electrical characterization of the coils
- Calculating the induced voltage and maximum power based on the test results performed by Utku Goreke on PMMA turbines.

Based on statistics, there is a high demand for spirometers for COPD and asthma patients. Among different types of spirometers, the turbine based sensors possess all the advantages of insensitivity to ambient pressure, temperature, humidity, and gas particles. In this study, we have demonstrated a new technique to approach the first turbine based MEMS spirometer sensor, which owns all the advantages of the conventional turbine based spirometers, in addition to having a lower price and being more portable. Furthermore, this design is capable of converting the energy of the human breath into electrical power. It also can be integrated easily with portable electronic devices like cellphones in order to record and transmit the patient's test results to health care centers for analysis and comments.

This thesis is organized into five chapters as follows:

- Chapter 2 provides background about lung structures and the most common lung diseases, COPD and Asthma. We review different types of spirometry tests followed by discussing the standards that are defined for spirometers reliability. This chapter also reviews two major types of spirometers: volume measure type and flow measure type spirometers.

- Chapter 3 focuses on the theory, design, and simulation of the turbine-based MEMS spirometer sensor. In the theory part, we describe fundamental equations governing the device operation. Simulations on magnetic leakage and saturation are provided for more accurate device performance estimations. Based on this analysis and considering microfabrication limitations, two device designs are presented.

- Chapter 4 describes the process of the masks design and microfabrication of the stators of the device. Stator fabrication steps along with related issues are thoroughly discussed in this chapter. At the end a brief summary and suggestions for future improvements are given.

- Chapter 5 presents the testing procedure of the fabricated stators. The resistivity and inductance of the coils are measured and compared to the theoretical analysis. The induced voltage and maximum delivery power of the sensor are calculated based on practical results.

- Chapter 6 concludes this thesis with a summary of main achievements. Future work for potential improvements on device performance are discussed.

# CHAPTER 2

# LITERATURE REVIEW

Chronic Obstructive Pulmonary Disease (COPD) and Asthma are two of the most common lung diseases worldwide.Correspondingly, there is a growing demand for early diagnosis as well as appropriate treatments targeted at these diseases. One of the most common practices in diagnosing and following the progress of such lung diseases is spirometry test, which is able to detect the type and extent of the lung malfunctions by measuring the exhaled or inhaled air.

In this chapter (Section 2.1), we will first discuss the lung structure and the most common lung diseases, COPD and Asthma. Sections 2.2 and 2.3 describe the spirometry test and the spirometer parameters, respectively. Sections 2.4 and 2.5 present the basic and modern kinds of spirometers.

## 2.1 Respiratory system

The biological system responsible for processing respiration by the use of specific organs and structures is known as the respiratory system. This process is done by supplying the body with oxygen via breathing in (known as inhalation) and then expelling out carbon dioxide by breathing out (known as exhalation).

### 2.1.1 Respiratory anatomy

The respiratory tract is composed of the alveoli, which are where cellular respiration occurs and the trachea is an airway that divides into tree-like branches that are both

symmetrical and asymmetrical. Each branch of the airway along the trachea becomes smaller, however the total area of the airways increases which allows the airflow resistance to decrease as the air moves into the bronchioles. Inhalation, also known as inspiration, makes use of the muscles in the chest, such as the diaphragm, to pull air in. Meanwhile exhalation, also known as expiration, passively expels air from the lungs. The alveoli, of which there are 300 million, have the combined surface area of a tennis court and this is where the oxygen and carbon dioxide exchange occurs (see Figure 2.1).

There are two kinds of arteries moving from the heart to the lungs called the pulmonary and bronchial. The pulmonary artery transports deoxygenated blood from the heart to the lungs. After passing through the lungs the blood becomes oxygenated and is pumped through the pulmonary veins into the heart, which then pumps it to the other organs in the body. Oxygenated blood is also circulated through lung tissue via bronchial circulation. The lungs also serve other functions such as protection against infectious agents and pollutants, metabolism and detoxification of substances, and synthesizing important compounds that help with inflammatory reactions [3].

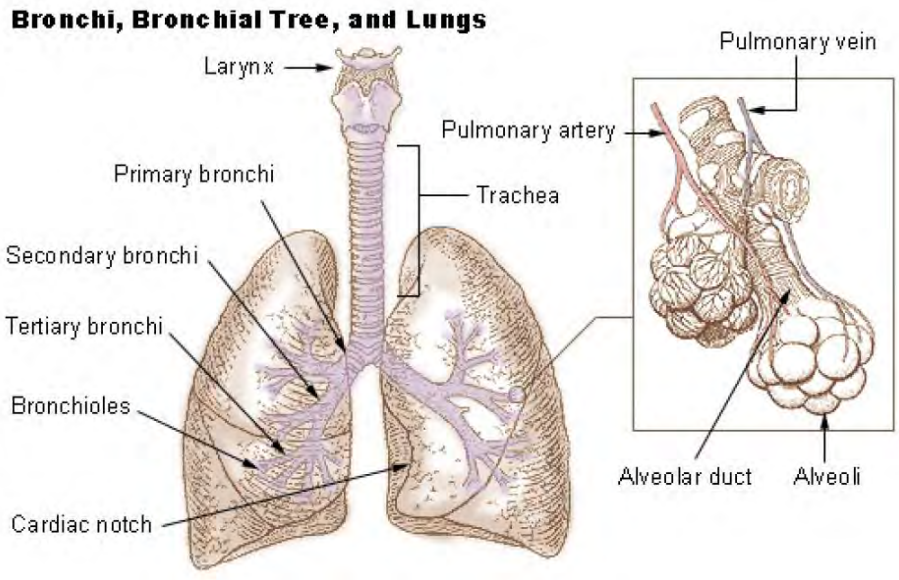


Figure 2.1: The respiratory tract [2].

The spirometry test does not directly quantify the oxygen transferring rate inside the lungs, but instead it measures the major factors influencing the oxygen transfer process which are the air flow rate and volume of air during exhalation and inhalation.

This test is mostly used for COPD and asthma patients. Asthma and COPD are two types of chronic lung inflammation, however, these two diseases are not the same across individuals and as such will affect different people in different ways. This requires a broad range of treatments in order to account for the differences found between individuals.

### 2.1.2 Lung Volumes

To help with explaining the pulmonary ventilation system the air in the lungs has been broken down into four volumes and four capacities [3]. The diagram in Figure 2.2 represents the average volumes and capacities of pulmonary ventilation. All volumes and capacities are explained follows:

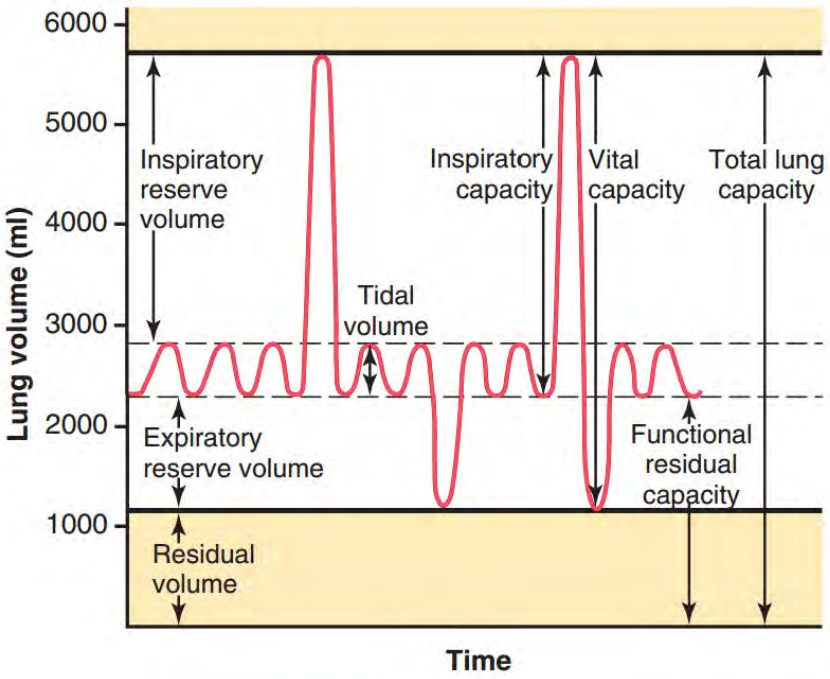


Figure 2.2: A diagram showing respiratory excursions during normal breathing and during maximal inspiration and maximal expiration [3].

- Tidal Volume (TV): The TV is the volume of air that is brought in and pushed out with each normal breath that a person takes. In an adult male the TV average is 500 milliliters.

- Inspiratory Reserve Volume (IRV): The IRV is the extra amount of air that goes above the normal TV when a person breaths in with full force. In an adult male the IRV averagee is 3000 milliliters.

- Expiratory Reserve Volume (ERV): The ERV is the extra amount of air that goes above the normal TV when a person breaths out with full force. In an adult male the ERV averagee is 1100 milliliters

- The Residual Volume (RV): The RV is the amount of air that remains in the lungs after it is forcefully expelled from the lungs. . In an adult male the RV averagee is 1200 milliliters.

- The Inspiratory Capacity (IC): The IC is equal to the TV plus the IRV, thus it is the amount of air that a person can breathe in (the IRV) and then distend the lungs to its maximum amount (TV). In an adult male the average is 3500 milliliters.

- The Functional Residual Capacity (FRC): The FRC is equal to the ERV plus the RV, thus it is the amount of air that remains in the lungs after a normal breath. In an adult male the average is 2300 milliliters.

- The Total Lung Capacity (TLC): The TLC is the maximum volume that the lungs can be expanded to with the greatest amount of effort. The TLC is equal to the VC plus the RV. This amount increases when the lungs lose their elasticity, such as with COPD and emphysema. In an adult male the average is 5800 milliliters.

- The Vital Capacity (VC): The VC is equal to the IRV plus the TV plus the ERV. This is the maximum amount of air that a person can push out of their lungs after filling their lungs to its maximum. In an adult male the average is 4600 milliliters.

### 2.1.3 COPD

COPD stands for chronic obstructive pulmonary disease and according to the Center for Disease, Control and Prevention more than 15 million Americans are diagnosed

with COPD, making it the third leading cause of death in the United States [4]. Two common conditions related to COPD are chronic bronchitis and emphysema which may happen either together or individually. Both of these conditions obstruct the airways irreversibly, but their pathological mechanisms are different [4]. Chronic bronchitis is caused when there is an airflow restriction in the bronchi due to excessive mucus and inflammation. Meanwhile emphysema is caused when there is destruction of the elastic tissue in the respiratory part of the lungs, typically in the alveoli as depicted in Figure 2.3. This results in difficulty in breathing due to smaller and narrower airways. While genetics does play a factor in COPD, most cases develop from environmental factors or cigarette smoking. Therefore COPD is preventable [2].

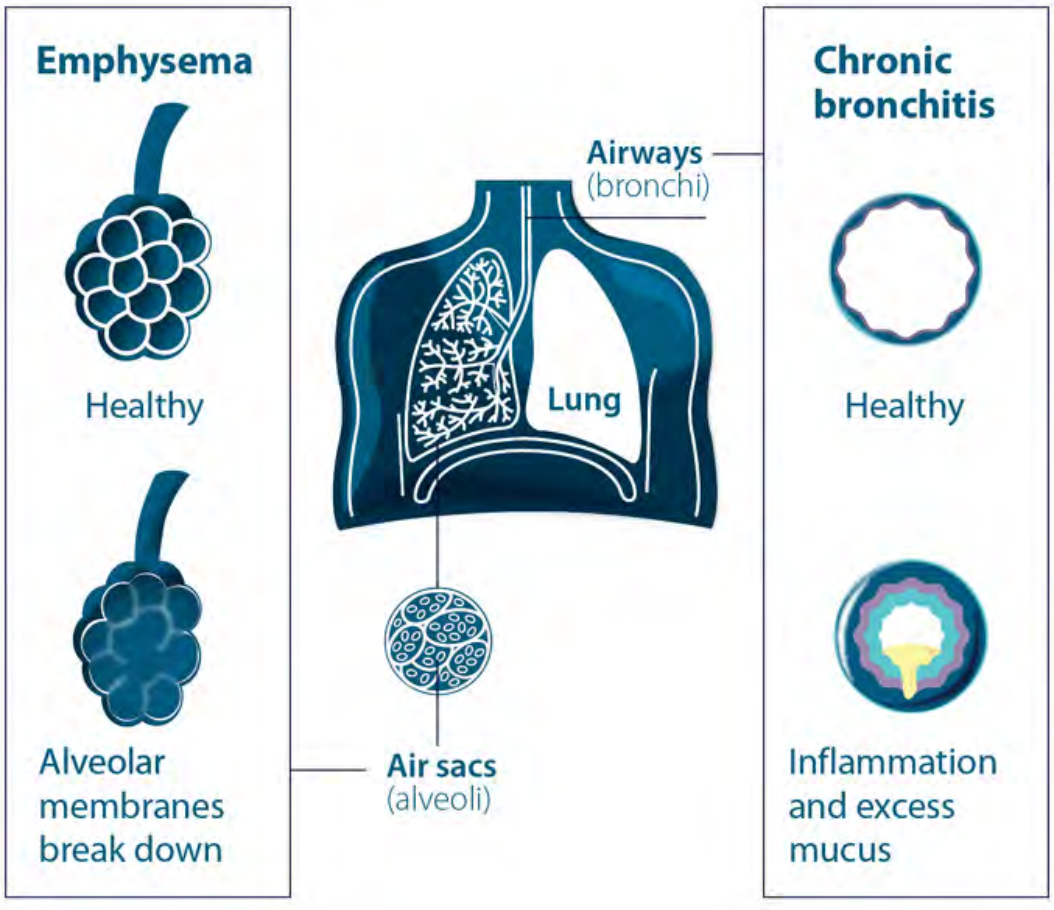


Figure 2.3: The diagram shows how emphysema and chronic bronchitis affect the lungs [4].

### 2.1.4 Asthma

Asthma is a fairly common long-term pulmonary disease, affecting more than 235 million people in the in the world [37]. Asthma is a chronic and long term condition in which a person's airways become narrow and inflamed with the end result being difficulties in breathing (see Figure 2.4). While it can manifest in different ways it tends to appear as an obstruction of the airways, bronchial hyper-responsiveness, and inflammation of the airways. Asthma resembles COPD in that it can be caused by genetic and environmental factors. It differs from COPD in that the inflammation caused in asthma may also be due to an allergic reaction, the resultant asthma attack having been caused by breathing in an allergen [2].

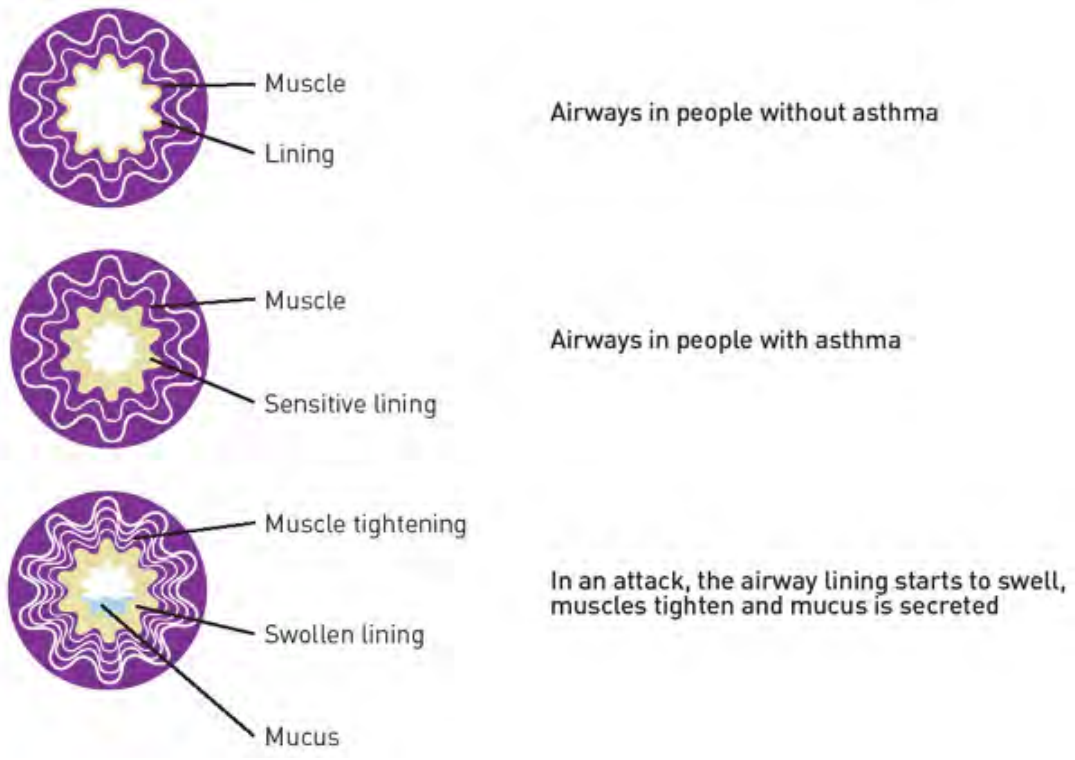


Figure 2.4: The changes to the airways that occur in asthma[5].

Asthma can be treated by the use of B2-adrenergic inhalants (bronchodilators) which work to open constricted airways swiftly. However, B2-adrenergic inhalants are not as effective when used on patients with COPD. This makes it possible to test if a patient has COPD or asthma by observing whether they respond to the B2-adrenergic inhalant or not. By using testing devices it is possible not only to diagnose if a patient

suffers from COPD or asthma but also to chart how far it has developed as well as charting any patterns in patient's symptoms [2].

### 2.1.5 Basic pulmonary function testing

As the most common test devices, the peak flow meter measures the maximum speed of exhalation. The peak flow meter is a kind of simplified version of spirometer that measures not only the flow rate during exhalation but also is able to measure the volume of air that goes in and out of the lung during inspiration and expiration. A digital peak flowmeter is shown in Figure 2.5(a).

Spirometry, however, is a more developed test that can also be used to diagnose the type and the extent of the lung function. Several distinctive tests can be run by spirometers to quantify lung volumes, the FVC (Forced Vital Capacity), the VC (Vital Capacity or Slow Vital Capacity) and the MVV (Maximum Voluntary Ventilation) are the most common ones. A computer-based spirometer is illustrated in Figure 2.5(b).


(a) Peak flow meter [38]. (b) Computer based spirometer [39].

Figure 2.5

## 2.2 Spirometric Measurements

A standard measurement set of protocols exist to assist in evaluating lung function and capacity. Each time a person is spirometrically measured the results are compared to a set of standards that have been established by the health community. These standards account for a person's age, height, sex, and race/ethnicity. Research has

shown that factors such as body size and demographic groups can have an effect on the diagnostic thresholds for such obstructive lung diseases. The following are the standard measurements used by the spirometry test.

### 2.2.1 Forced Vital Capacity

This test is conducted by having the patient breath in fully and then pushing all the air out of their lungs as fast as they can. The results are then shown on a graph and are compared to a predetermined set of values based on the general measurements composed by the health community. These measures, as stated above, take into account factors such as height, sex, and age. For instance, a healthy adult can typically push all the air out of their lungs in about 6 seconds. Taking significantly longer may indicate the presence of COPD [2].

The graphs used for displaying spiromteric results are called the spirograms. Spirograms display volume in liters, time in seconds, and airflow rates in liters per second. There are two types of spirograms, the Volume-Time and the Flow-Volume Curve. The curves and spirometric parameters are illustrated in Figure 2.6.

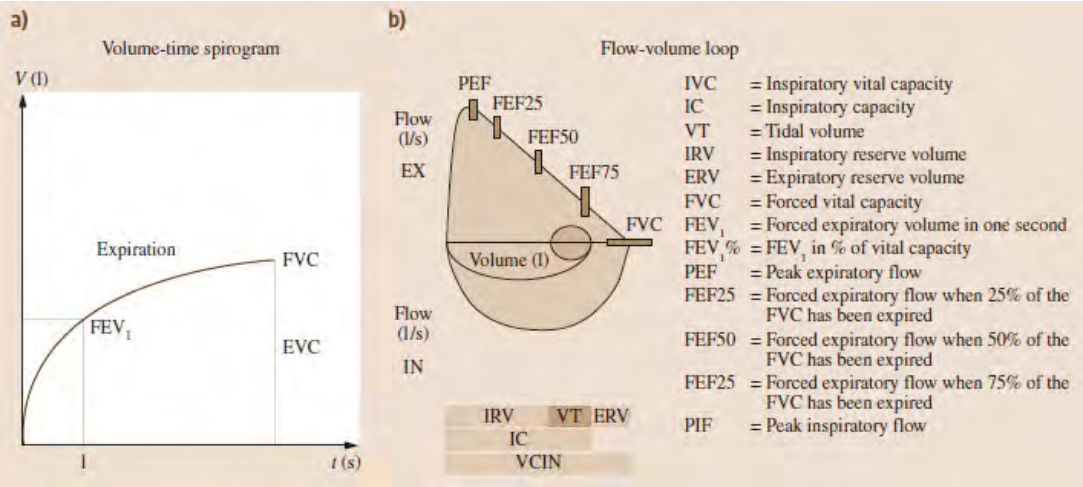


Figure 2.6: (a) Forced spirogram, (b) flow-volume loop [6].

#### 2.2.1.1 The Flow-Volume Curve

The VTC, which can be seen in Figure 2.6(b), is composed of the expiratory flow vs the volume curve and displays the airflow rates in relation to the amount of air that are being pushed out of the lungs. The curve created also has points that contain the PEF and the FVC.

The Flow Volume starts on the X-axis; this is known as the volume axis. When the test starts the flow and volume are at zero. After the test starts the point of the cover begins to rise and peak, this is known as the Peak Expiratory Flow (PEF). The PEF will fall as air is pushed out of the lungs. For a healthy set of lungs the FV will descend in a straight or convex line, going from the top (PEF) to the bottom (FVC). The Forced Vital Capacity (FVC) is the maximum volume of air forcefully pushed from the lungs at the height of breathing it in. The forced inspiration that follows the forced expiration has roughly the same morphology, but the PIF (Peak Inspiratory Flow) is not as distinct as PEF.

#### 2.2.1.2 The Volume-Time Curve

The VT is the volume of air vs the time curve and it corresponds to the FEV1 and FVC. The amount of air pushed out of the lungs during the first seconds of the FVC is called the FEV1. The curve is shown in 2.6(b). Time and flow start at the (0,0) on the graph. Since most of the air is pushed out of the lungs at the start of the test when the large airways of the lungs are emptied the graph will swiftly rise. 80% of the total volume of air in the lungs is pushed out within the first second of the test. As air empties from the lungs the expired volume that was rising will level off into a horizontal line.

### 2.2.2 (Slow) Vital Capacity (SVC)

This test is conducted by having the patient breathe in fully and then pushing all the air out of the lungs slowly or by having the patient push all the air out of their lungs fully and then breathing in slowly until their lungs are full. This test can be used

to measure the TV, IRV, ERV, and IC. The SVC is closely related to the FVC and differences between the two can suggest a possible collapse in small airways. This has been attributed to COPD and is believed to be due to a loss of elasticity in the lungs.

### 2.2.3 Maximum Voluntary Ventilation

This test is done by having the patient breath in and out as rapidly and hard as possible into the spirometer for 12 seconds. The total volume of the gas moved by the lungs is recorded. The value is multiplied by 4 to produce the maximum volume that the patient breathed per minute by voluntary effort. This test can be dangerous for some patients, thus it is no longer commonly given.

## 2.3 Spirometer parameters

In order to obtain reliable measurements through spirometry tests, some standards are defined for spirometers. Moreover, other parameters such as spirometer calibration and hygienics are important factors that should be considered as well.

### 2.3.1 Measuring range

There are several conditions that have been defined over the years as standards to guarantee the spirometer results. These are called the medical, technical requirements or the MTR. The MTR typically includes:

1. Resistance of spirometer to breathing
2. Volume of airflow sensor (known as dead space)
3. Response threshold of airflow rate
4. Measure of the range of airflow rate
5. Limits of Measurements error

6. Non-linearity of the frequency response in the range of relevant frequencies

Starting in 2005 the American Toracic Society (ATS) and the European Respiratory Society (ERS) introduce a mutual standard form as the MTR [40] (see Table 2.1).

Table 2.1: Parameters of MTR for spirometers, standardized in 2005 [1].

| Standardized parameter | Values |
|---|---|
| Resistance to breathing, Pa.s/l | $\leqslant 150$ |
| Threshold of response on airflow rate, l/s | $\leqslant 0.050$ |
| Upper limit of volume measurements, l | 8.0 |
| Upper limit of airflow rate measurements, l/s | 14.0 |
| Limits of volume measurement errors, % | $\pm 3$ |
| Limits of airflow rate measurement errors, % | $\pm 3.5$ |
| Nonlinearity of dynamic characteristics in frequencies range till 15 Hz, % | $\pm 5$ |

Furthermore, [1] published a paper that includes more standards of the MTR [1]. These standards were based on analyzed requirements for spirometers across different deviances and are hierarchy ranked. See Table 2.2 for more details.

Table 2.2 has been divided into two subgroups, one for adults and one for children. Each subgroup has different requirements. The three levels also have more details as follows:

1. 1st level is for simple devices measuring 1-3 forced breaths for the PEF, FVC, and FEV1. Spirometers of this level have simple design and operation along with minimum weight and size requirements, known as “home medicine" devices.

2. 2nd level is used for clinical testing and the screening of large populations.

3. 3rd level devices can achieve maximum level of accuracy and sensitivity to measure parameters of spontaneous breathing patterns, the vital capacity structure and maximal voluntary ventilation.

Table 2.2: Prospective MTR for spirometers [1].

| Parameter | Application of spirometer | | | | | |
|---|---|---|---|---|---|---|
| | For adults | | | For children till 12 years | | |
| | Levels of hierarchy | | | | | |
| | 1 | 2 | 3 | 1 | 2 | 3 |
| Resistance to breathing, Pa.s/l | 40.0 | | | 20.0 | | |
| "dead space" volume, ml | 100.0 | | | 50.0 | | |
| Response threshold on volume, l | 0.05 | | | 0.02 | | |
| Response threshold on airflow rate, l/s | 0.1 | 0.07 | 0.05 | 0.05 | 0.03 | 0.02 |
| Upper limit of volume measurement, l | 8.0 | | 10.0 | 5.0 | | |
| Upper limit of airflow rate measurement, l/s | 12.0 | 15.0 | 20.0 | 8.0 | | |
| Limits of volume measurement error, % | ±7.5 | ±3.0 | ±1.5 | ±7.5 | ±3.0 | ±1.5 |
| Limits of airflow rate measurement error, % | ±7.5 | ±3.0 | ±1.5 | ±7.5 | ±3.0 | ±1.5 |
| Nonlinearity of dynamics characteristics in frequencies range till 20 Hz, % | ±5.0 | ±2.0 | ±1.0 | ±5.0 | ±2.0 | ±1.0 |

### 2.3.2 Verification and Calibration

To verify the accuracy of a flow sensor and calibrate it if need be, an optional verification and calibration routine should be carried out in any spirometer. To calibrate the spirometer you can either use a manual pump or a motorized one that can be connected to the spirometer. A known volume will then be pumped into the spirometer with different flow rates, typically between -10 l/s and +10 l/s, which covers most flow ranges. So long as the flow pumps into spiromter, it will measure the instantaneous flow rates and then find the volume using these measured data. The results can then be compared to the pump parameters to discover if the flow rates have been accurately measured [6].

### 2.3.3 Hygiene

Use of the spirometer can be a source of cross infection. To reduce the risk of infection the spirometer comes with in-line filters and replaceable sensors. The filters are a good way to prevent bacterial infection so long as the sensors are fixed; however, their resistance should be negligible to have no effect on the measurements. The filters should be replaced after each use. One can also use interchangeable flow sensors that should be changed after each patient uses the spirometer. The sensors can also be sterilized for use in future tests or disposable sensors can be used. It should be noted that low cost sensors can lower the accuracy of the spirometer.

## 2.4 Volume measure types spirometers

Before evolution and widespread use of electronic devices very basic types of spirometers were being used, in which the volume of lungs were measured directly. Nevertheless,in recent years the sensor paradigm has shifted towards the flow measure types. The three different types of basic spirometers are discussed in the following sections.

### 2.4.1 Water-sealed spirometer

Gas volume can be directly measured by several volume displacement spirometers. The water-sealed spirometer is the simplest and oldest design made of an inverted counter weighted bell, cylindrical water reservoir and an upright. As it can be seen in Figure 2.7, the bell is placed on top of a known volume of gas, which is trapped inside the chamber.

Inspiring or expiring into the tube results in gas volume changing, and so the bell moves vertically up or down. A pen is connected to the bell which writes on a rotating drum called Kymograph. As a result of such movements, a graph is printed on the paper that covers the Kymograph which can depict the tidal volume. Unfortunately this device can only work properly if the respiration is performed slowly. Consequently, it would not be able to measure forced expiratory volume. Plus it would

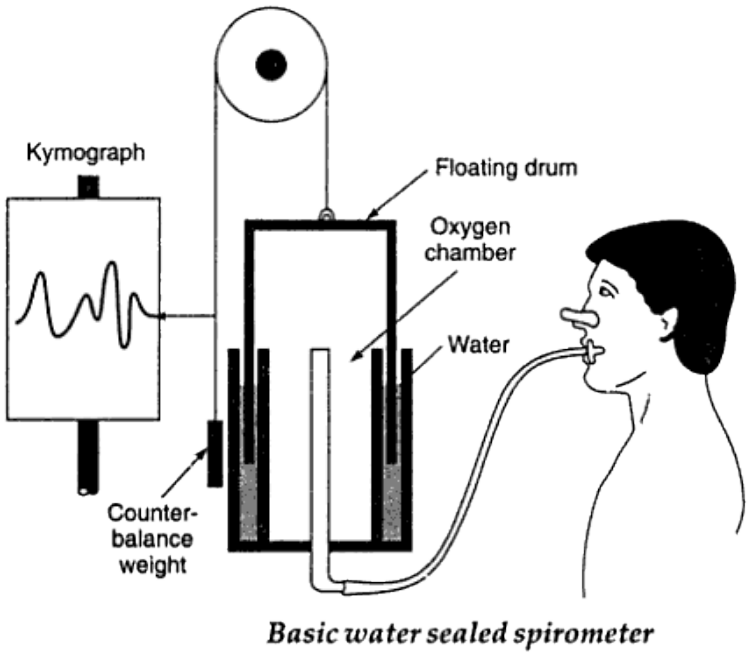


Figure 2.7: Basic water sealed spirometer [7].

be difficult to design the device to be able to reach the exact same gas volume after each filing or sinking during the breathing. In addition, expiratory volume may be overestimated due to the inertia and the bell oscillation, which are other common problems of the instrument. To lessen these problems a large and light bell is being used and the bell covers a smaller area of water than that of the water tank [7]. The air flow enters the spirometer and the result emerges as volume displacement same as a mechanical integrator. By connecting a linear potentiometer to the pulley part, the volume changes can be converted to an electrical signal.

### 2.4.2 Dry-seal spirometer

In the dry-seal spirometer, a thin layer of latex (or other flexible material) is used to seal the bell to its base. When gas enters the bell, like the water-sealed spirometer, the latex keep the gas and forces the bell to move. The dry-seal spirometers can be mounted vertically, and instead of a moving bell, a moving piston may be employed. As with the water-sealed spirometer both electrical and manual recording are achieved. Also in rolling seal spirometers, which is shown in Figure 2.8, a plastic or rubber bellows is utilized which contracts and expands as the patient breathes. Water-

seal displacement spirometers tend to be somewhat more accurate than those that are dry-sealed that is because of the inherent resistance in the bellows. The dry-seal spirometers, however, need less maintenance since they do not contain water [41].

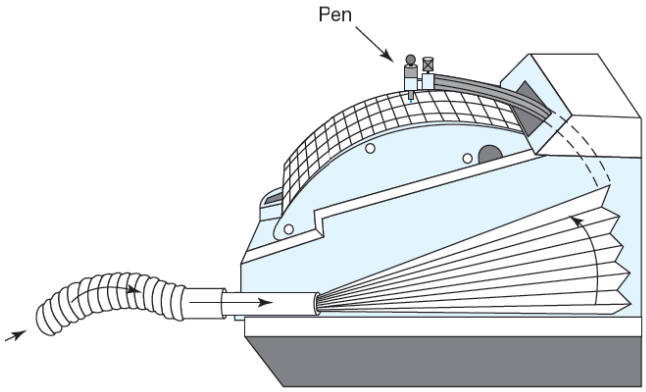


Figure 2.8: A rolling seal spirometer [8].

The tests run by water and dry seal spirometers depend a lot on patient cooperation and technician performance. Moreover, the graphical results need to be calculated manually which consumes a lot of time.

### 2.4.3 Wedge Spirometer

This is a waterless spirometer built of two parallel large square plates hinged at one edge, as whown in Figure 2.9. While one of the plates is fixed to the stand, the other plate can swing along the hinge freely. A vinyl bellows is used to seal airtight the space between two plates. The bellows is designed to not expand inward or outward while having high flexibility in the plate motion direction. This prevents any distortion due to pressure difference between the interior and exterior of the wedge. Breathing into the spirometer changes the volume inside the spirometer which results in the free pan displacement. Attaching two linear transducers to the plates' edges enables converting the displacement into the electric signal. One of transducers' signal output is proportional to the volume and flow rate is calculated from output of the other one. The outputs are sent to an electronic unit including amplifier, power supply and inbuilt calibration system.

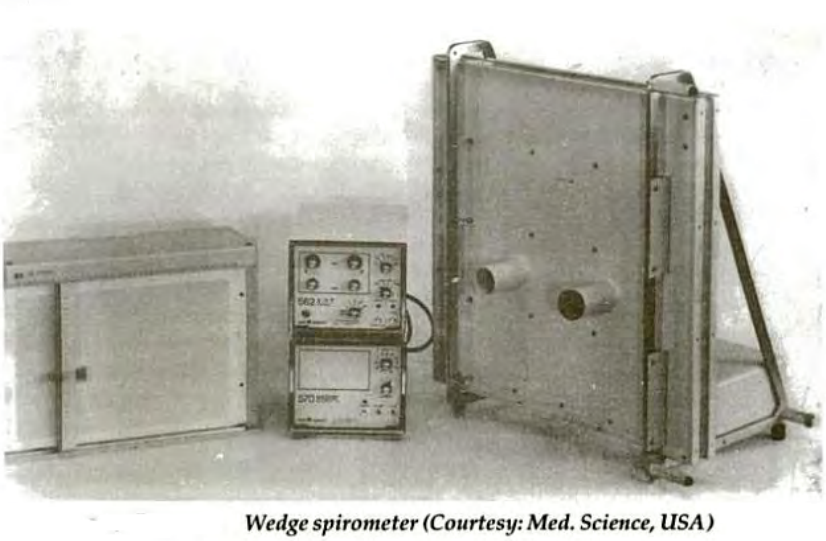


Figure 2.9: Wedge spirometer [7].

### 2.4.4 Volume displacement spirometers advantages and disadvantages

Volume displacement spirometers benefit from the advantage of simple use and construction. No processors or computers are required for simple volume and time measurements. May be most importantly, the gas compositions do not affect the measurements and they are easy to calibrate. Nonetheless, they suffer from several disadvantages. First, the volume displacement spirometers are bulky. Especially when the water-sealed spirometers are filled with water, can be heavy and spill when tipped. Second, Due to their mechanical action, their response frequency lies within a limited range and hence they are not well suited to rapidly changing signals (although they have acceptable frequency response for most common measurements). Last, the maximum volume they can measure is limited by their size. Therefore, for a test in which tidal volume is quantified over a period of five minutes, it would be difficult to employ the volume displacement spirometer, without a series of complicated valves, as it would be filled before the experiment was over [42].

## 2.5 Flow measuretypes spirometers

To achieve further and detailed information in a short time, electronic spirometers have been developed. Such spirometers have an outcome as electric signals that can

compute the numerical results electronically. Consequently, more precise data in a less period of time would be achieved. An increase in accessibility to low cost personal computers allows amateurs to get accurate results using a well-designed software program.

There are various types of spirometers in the market that vary in size and performance. Their prices range from about $175, which are very simple and measure only some limited parameters, to $3,500 for the more complicated ones. Advanced spirometers usually contain a very good monitor or even printers and can perform all spirometry tests with high accuracy. In the following two spirometers are from different companies and can be taken as examples of the types available.

SP-10 laptop style spirometer by the Welch Allyn company is one of the most expensive spirometers, which has a large screen and printer and can perform using both disposable and reusable differential pressure sensors (Figure 2.10.a). It possesses a lightweight and well-packed design but it has been designed for the clinical use in the office and so it is not portable. It can perform all FVC, SVC, MVV and MV tests and meets all industry standards [43].

An example f a cheap spirometers, is the Spirocheck spirometer from Micro Direct Company shown in Figure 2.10.b. This device is very simple, light and compact but it only measures the FEV1 and FEV1%. This spirometer uses stator/rotor sensor that needs to be cleaned after each test [44].

In spite of the availibility of spirometers in markets, very few devices have been purchased demonstrated for personal use. Due to the fact that asthma and COPD are becoming more prevalent mostly in highly-populated developing countries, remote monitoring can result in better medical services along with much less cost for governments and patients. Accordingly, significant efforts have been dedicated to develop low-cost, reliable and portable spirometers [46] insensitive to temperature, humidity and ambient pressure [47], [48].

(a) Welch Allyn, SP-10 Laptop Style Spirometer [45].


(b) Micro Direct SpiroCheck Spirometer [45].

Figure 2.10

### 2.5.1 Electronic spirometer sensors

Independent of the cost and sizet of any pulmonary function device, from a hand-held peak flowmeter to a body plethysmograph, the flow sensor always plays for the core element. Therefore most of the research to develop spirometers focuses on their flow sensors. Especially nowadays micro-machined sensors play a very important role in developing new spirometers compared to large-scale ones due tolow power consumption, better dynamic characteristics, reduced mass, low cost, and small size [49]. There are many kinds of flow rate sensors but the thermal sensor, differential pressure sensor and turbine sensor are the most famous ones for spirometers.

#### 2.5.1.1 Thermal flowmeter

The operating principle employed in thermal flowmeters is based on heat convection between the sensor and fluid [31].The flowmeter includes two temperature sensors, one senses the fluid temperature and other one is an electrically heated sensor. . There are three different modes of operation for hot film/wire sensor: constant current (CC), constant voltage (CV), and constant temperature (CT) [50]. CT mode possesses a faster frequency response along with a higher resistivity that makes it the most preferable one among these three modes [10]. All the modes function is based on the

cooling effect of the flow stream on heated hot film sensor.The faster gas flows, the more strike between the sensor and gas molecules occur, and so the higher energy transfers from hot wire sensor to the fluid.Consequently, we can easily measure the flow rate by measuring the amount of voltage that is used to heat up the hot film [32]. However, it should be considered that not only the flow rate but also the gas density can affect the result as well. In the circuit, anemometer is implemented in one arm of the Wheatstone bridge with a negative feedback as shown in Figure 2.11 [32].

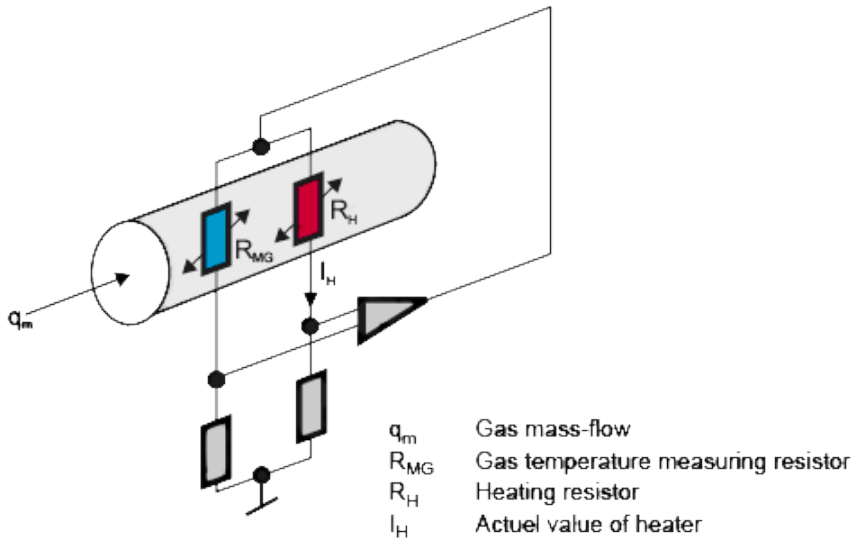


Figure 2.11: Diagram of a thermal flowmeter components and its simplified circuit. [7].

Although hot film and hot wire sensors work similarly, each has its own merits and flaws. On the one hand, a hot film sensor, with a larger surface area, results in more strike of gas molecules with the film that enables an easier heat transfer, and hence results in a higher output voltage. In addition, hot film provides better stability and less sensitivity to the micro particles effect on its calibration curve. On the other hand, hot film sensor responses in lower frequency and need more energy supply. On the overall, the hot film advantages overcome its cost in case of spirometers and that is why hot film anemometers are recommended as spirometer sensors [51].

The micromachined hot-wire and hot film sensors have a wide range of use in spirometers, which is due to possessing high accuracy in low flow rates, broad measurement range, fast frequency response, good mechanical properties, low pressure drop and small probe size [52], [53]. Both micromachined hot-wire and hot film sensors are

shown in Figures 2.12 and 2.13 [51].

Unfortunately due to having a non-linear calibration curve, certain operational and environmental factors, like the ambient pressure and ambient temperature along with its variations, cause errors in the hot-wire/hot-film calibration curve. Furthermore, the presence of dust particles in the vicinity of the sensor can result in a drift in its calibration curve. That is why it may be required to recalibrate during its operation. Moreover, it has been reported that if the thermal sensor operates in a high wind field, its accuracy and sensitivity decreases. Also thermal flow sensors are not able to distinguish between forward and backward flows and so they cannot work individually as bidirectional sensor [54], [55].

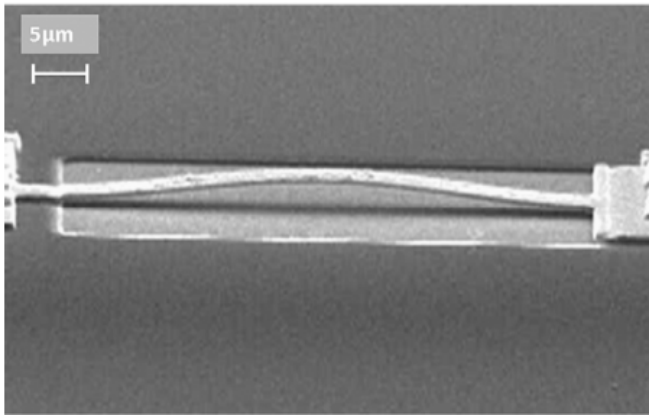


Figure 2.12: A micromachined hot-wire sensor obtained by [9].

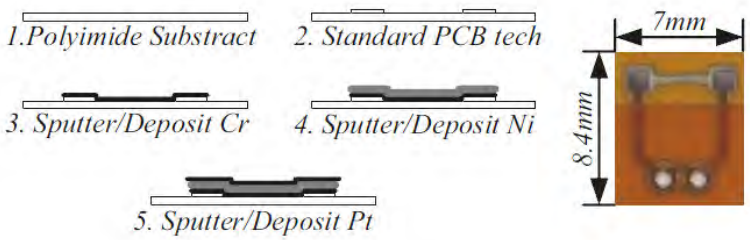


Figure 2.13: A micromachined hot film sensor obtained by [10].

#### 2.5.1.2 Differential pressure sensor

This is one of the classical ways to measure respiration rate. In order to measure the flow rate using differential pressure sensor, a laminar flow and drop of pressure

is required. To achieve this, we need to use a resistive element which its type will characterize the principles of sensor [6]. In this method, gas flow rate is obtained by measuring the drop pressure across the flow tube. Due to the fact that gas pressure along the tube decreases during exhalation and increases during inhalation, the sensor is able to determine the flow direction. The velocity of gas is calculated by means of Bernoulli's principle which leads us to the equation $v = k\sqrt{p}$, where $v$ is the gas velocity, $k$ is a constant and $p$ is the pressure [48]. And finally, the gas volume is achieved by multiplying the velocity by time.

The pneumotachograph functional properties are based on geometric structure of pneumatic resistance. The Venturi tube, FleischPitot tube and mesh screen are such resistive elements.

**The Fleisch pneumotachometer** This is one of the more common flowmeters being used in spirometers. As its name implies, its principle is based on Fleisch and includes a Fleisch Pitot tube. This tube consists of a bundle of capillaries, typically a roll of z-folded sheet metal acting as a fixed resistor to cause a linear relation between the pressure difference and flow rate (see Figure 2.14). The major problem is that even very small droplets would be able to block or obstruct the holes and affect their resistivity [56]. Consequently, its calibration can change and thus errors occur in the measured rate and volume of the flow.

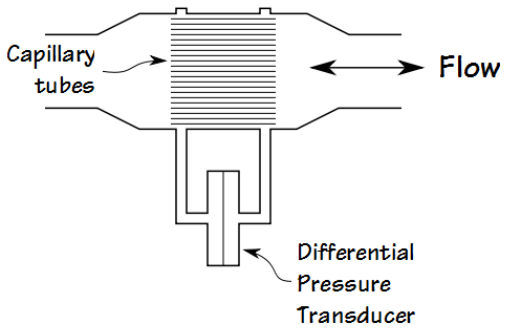


Figure 2.14: The Fleischpneumotach consists of a set of narrow capillary tubes as the resistor [11].

**The Lilly pneumotachometer** Here the close-mesh screen has been used to resist the flow in order to enable differential pressure measurements. With respect to the desired results, one or more mesh screens can be used. To achieve a higher linearity, more mesh screens are required; however, this increases breathing resistance, which is undesired. As illustrated in Figure 2.15, one of the main features of the Lilly pneumotachometers is the large difference between the mesh and tube diameter.

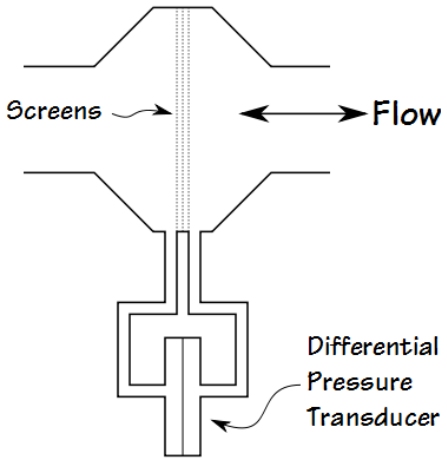


Figure 2.15: The Lilly pneumotachometer using mesh screens as resistor [11].

**Diaphragm pneumotachometer** In this type of pneumotachometers, a specially slotted foil diaphragm is used to provide the desired resistivity. The advantage of this design is its lack of sensitivity to humidity and impurities, which make it easier to be cleaned. Its sensitivity to low or high pressure is flexible and it depends on the diaphragm design, which makes it possible to produce a more differential pressure at lower velocities or vice versa [6].

**Venturi-type pneumotachometer** Venturi-type PTM operate similar to the Fleisch PTM, but it substitutes a Venturi throat for the linear resistance element of the Fleisch PTM (see Figure 2.16). The resulting pressure drop is proportional to the square of volume flow. Because of their open geometry, Venturi PTM's are less prone to the problem of liquid collection and present less resistance to flow. Their drawbacks are the nonlinearity of the calibration and the requirement for laminar flow. In addition,

the flow head is asymmetric so we cannot measure bidirectional flow [17].

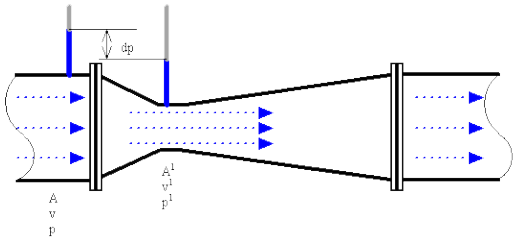


Figure 2.16: The diagram of a venturi type pneumotachometer [12].

As general disadvantages of differential manometers, we can refer to their sensitivity to humidity, temperature and atmospheric pressure which may result in a frequent need of recalibration [57]. To boost its reliability, in the most commercial pneumotachographs, a thermostat is used to minimize the humidity and maintain the sensor in a constant temperature [7]. Furthermore, qualification tests, reliability and operating characteristics of the pressure sensors are mostly based on the use of dry air as the pressure media [10]. As mentioned before, the screens pores and capillary tubes that are used in this kind of spirometers can easily be blocked by solid or liquid particles in the patient's breath. Consequently, the effective cross-sectional area of the flow element is reduced and the mechanical resistance of the device changes. To mitigate these effects, some tube designs own a bend between mouth and the sensor to retain the sputum droplets.

To overcome problems of accuracy in high and low pressure, which prevents the flowmeter from being sensitive in all the required ranges, some researchers have employed several sensors in one device. The following examples are such combinations.

[13] have coupled two differential pressure sensors into the same device, as illustrated in Figure 2.17. In their research they take different size diaphragms, made from piezoresistive pressure sensor, are implanted. The larger one will allow sensitivity to low pressure gas flow while the smaller one would have a better sensitivity in high pressure flow [13].

Additional research is performed by Que et al. which is a combination of a micro hot film sensor and a micro differential pressure sensor to capture the low and high airspeed respectively. Both sensors transfer their signals in digital form to a micro-

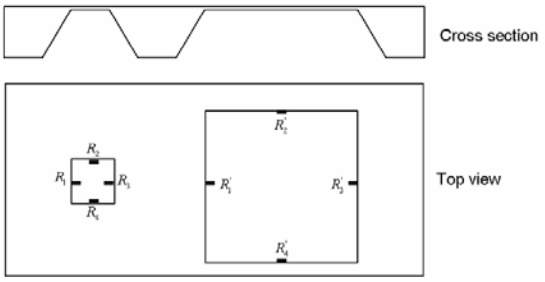


Figure 2.17: Implementation of two different size of piezoresistive pressure sensor to manage the all pressure range [13].

processor and so a wide range of measurement can be detected [10].

#### 2.5.1.3 Turbine flowmeter

**Conventional turbine flowmeters** In conventional turbine flowmeters, the mechanical energy of the breath rotates the blades of a fixed turbine. Since in this method the fluid energy is converted to the rotational energy, the gas flow rate is obtained by measuring the number of rotations per unit of time. As can be seen in Figure 2.18, in commercial turbine flowmeters, a light-emitting diode (LED) and a photodiode sensor is being used to detect the vane velocity by converting its rotational speed into electrical impulses. By means of a microprocessor in control unit, the gas volume can be calculated from the gas flow rate, which is proportional to the vane speed. The advantages of this system are its insensitivity to gas composition, water vapor, turbulent flow and gas temperature. In addition, the relation of gas flow rate and turbine speed is perfectly linear. Also the sensor can be easily taken out and cleaned. A disadvantage of a turbine flowmeter is its inertia [58], which can be minimized by employing very lightweight vanes, a deflector, and lowering the bearing resistance [6], [35].

**Static turbine** In this kind of turbine, unlike to the conventional one, the turbine wheelsdo not rotate. In this case, the flow of the gas generates a torque on the turbine blades, which is measured by a torque sensor. A micromachinedpiezoresistive cantilever beam is employed to act as the torque sensor. As illustrated in Figure 2.19, the torque sensor includes stiffness reduction beams, in which two polysillicon strain gages are embedded on both sides of the beams. In case of flow, the starin gages

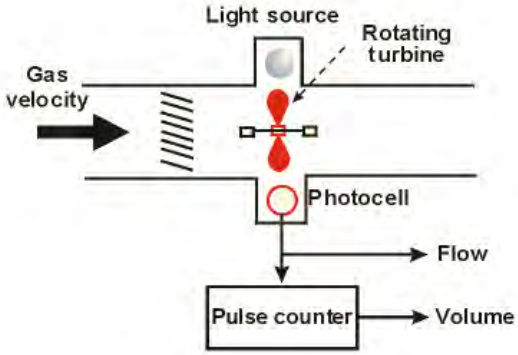


Figure 2.18: Illustraion of a conventional turbine flowmeter [14].

experience tension and compression proportional to the flow rate and so the torque is measured. Due to the perfectly symmetrical structure, the sensor is able to sense the axis of the flow.Since it is not rotating, the turbine does not go through any bearing or wear friction. However, as the sensor is made of piezoresistive (especially in $10^{16}$ dopant), it would be sensitive to temperature variables [15].

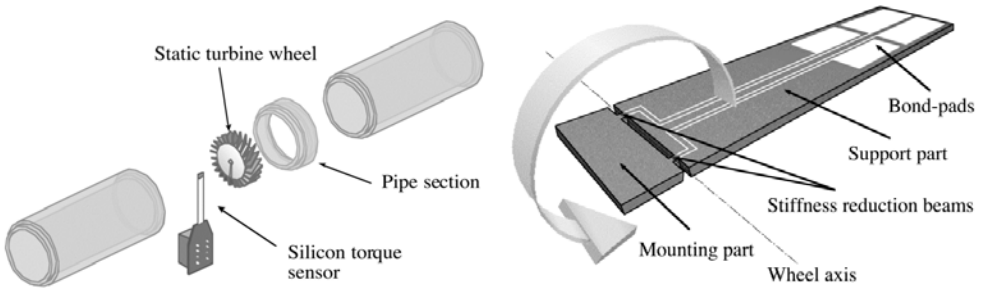


(a) (b)

Figure 2.19: (a)The static turbine includes a turbine wheel mounted on a torque-sensing device. (b) The torque-sensing element composing of three parts: the supporting part, the mounting part and two stiffness reduction beams [15].

#### 2.5.1.4 Ultrasound (Transit Time) Flowmeter

Ultrasound sensors consist of twin transducers placed in the flow tube but on opposite sides and transmit ultrasonic wave toward each other. The diagram of the ultrasonic sensors is depicted in Figure 2.20. Mostly piezoelectric types of transducers are used

and they possess the capability of both sending and receiving the ultrasound signals. The pulse transit time between transducers are measured. In the case that fluid passes through the sensor, transit time of the pulse in the direction of the gas flow decreases while the pulse transit time in the opposite direction increases. Since the transfer time variations are proportional to the fluid velocity, by some calculations the flow rate can be obtained [59].

To reach a better efficiency, the mounted piezoelectric transducers are operated at their resonant frequency. 40 to 200 kHz range of frequency is known the best for gas flowmeters since using higher frequencies leads to the higher absorption losses in gas whilst the frequencies less than 40 kHz are audible and so annoying [7].

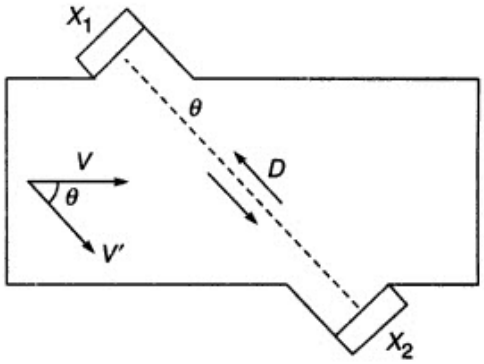


Figure 2.20: The diagram of flow tube and the position of ultrasonic transducers used in transit-time based ultrasonic spirogram [7].

The gas density, viscosity, and temperature do not affect the results in ultrasonic spirometers. To use the ultrasound sensors as spirometer sensors, the tube size must be at least 15 mm in radius. Hence, the total transfer delays are mostly measured in microseconds and so the accuracy of a directly single delay measurement must be in nanoseconds. Such small time differences make the measurements difficult using ultrasonic technique [7].

The transducers used in such flowmeters are disc-shaped flat ones that are placed at an angle on both sides of the tube walls inside the recesses. This arrangement not only protects the transducers from fluid contaminations but also avoids flow disruption. Although for liquid fluids some transparent windows are being used to enhance impedance matching to the media and protect the transducers, to obtain good acous-

tic transmission in respiratory gas flows the medium must be in close contact with the transducer. That is why for spirometer use the recess is kept open and hence undesirable turbulence and moisture collection can occur.

The geometry of open tubular wells can lead to fluid accumulation, which interferes with or obliterates coherent ultrasonic transmission. In addition to the unwanted dead space and condensation issue, the zero flow base line signals demonstrates drift and is discovered to show oscillations with temperature variations. The situation deteriorates when the transducers are applied to patients on a ventilator because of fluid accumulation which can cause highly inaccurate signals. In 1975 some modifications to the ultrasonic pneumotachometer construction were made by Blumenfeld et al that led to the design of coaxial version shown in Figure 2.21 [16]. In their design, the crystals are mounted midstream in the line of flow, with their transmission axis on the center line of the tubular housing. The principle of measurement of flow is that of measuring transit times, which is a function of the linear gas velocity and hence of flow.

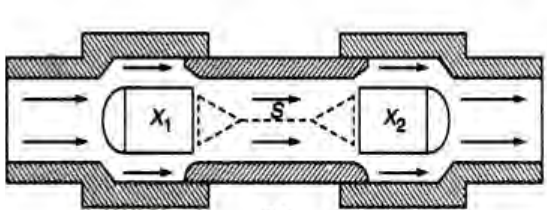


Figure 2.21: The Coaxial ultrasound pneumotachometer designed by [16].

Unfortunately this design is reported to have several problems as well. For instance, large amount of artefacts can be created in case of the combination of the reflected and primary ultrasonic transmission. Similarly, there could be alterations in the effective joint path length of flow and ultrasound transmission as a function of gas velocity and composition.Moreover, the temperature, humidity and composition of the gas can also affect the ultrasound velocity, which results in variation of estimation of flow velocity.

Plaut and Webster designed an ultrasonic pneumotachometer in 1980, shown in Figure 2.22, that unlike coaxial transducer and cross-the-stream configurations, not only the flow disruption, reduced sensitivity, fluid collection and dead space issues are

solved but also the favorable features of open tube geometry are preserved. [17]. They used cylindrical shell transducers with their inner surfaces flushed with the walls of the flow tube to prevent flow disruption and fluid accumulation. The ultrasound transmission axis is parallel to that of flow causing a boost in device sensitivity.

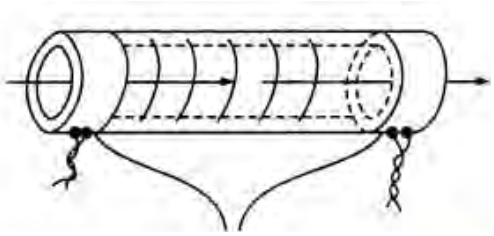

Figure 2.22: The configuration of ultrasound pneumotachometer showing the cylindrical Shell transducer and the airway obtained by Plaut and Webster [17].

It is claimed that even in the presence of little obstruction to breathing, qualitative parameters associated with respiration can be measured (It can also measure qualitative parameters associated with respiration while presenting little obstruction to breathing). However, they have also reported that highly accurate data would be achieved if the temperature and composition of the gas are varying within a narrow range. They caution that a poor understanding of the nature of the ultrasonic field and how it interacts with moving gas remains the most troublesome problem for the successful development of ultrasonic pneumotachometers. The other problems are the poor acoustic efficiency of ultrasonic transmission through gases, the wide variation in gas composition, temperature and humidity and the need for high accuracy and wide dynamic range.

#### 2.5.1.5 Vortex flowmeter

In this kind of flowmeters, a resistance, which is called bluff body, is placed in the middle of the path of the flow to create vortices.One type of bluff body and resulted vortices can be seen in Figure 2.23. The vortices happen at a defined frequency that is proportional to the velocity of the fluid. By measuring the number of vortices via piezoelectric elements, optodes or thermistors, we would be able to calculate the flow rate. However, it is not able to sense the direction of the gas and so is a unidirectional sensor [6].

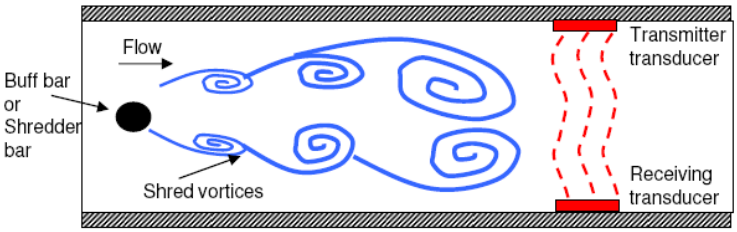


Figure 2.23: The diagram of a vortex flow meter [18].

Owing to the drawbacks of current spirometers, further research is focused on improving spirometer sensors that some of these sensors are discussed in the following sections.

#### 2.5.1.6 Amorphous Ferromagnetic Materials based sensor

This sensor is introduced by Nakesch et al. and contains two amorphous FeNi-based ribbon glued to a plastic film that works based on magnetostriction principle. The sensor components are illustrated in Figure 2.24. The airflow makes a compression or tension in FeNi ribbon proportional to the flow velocity and finally results in output voltage variation on the coils. This is due to changes in amount of permeability ($\mu$) and coupling factor ($k$). For its disadvantages we can refer to too complex nonlinear relation between the flow rate and the output voltage in addition to suffering from problematic mechanical adjustment. The sensor is so simple and affordable and can be changed easily while they need to be calibrated after they are changed. Moreover, good solidity and hygienic properties have been reported for these spirometer sensors [19].

#### 2.5.1.7 Cantilever based sensor

In 2010, Wei et al introduced a new spirometer sensor. As it can be clearly understood from its name, it is made from a number of cantilever beams, shown in Figure 2.25.a, which are deformed under pressure of the gas flow (see Figure 2.25.b). The deformation results in variation in the sensor resistance and hence the gas velocity can be detected. The sensor is unidirectional and the relation between the flow rate

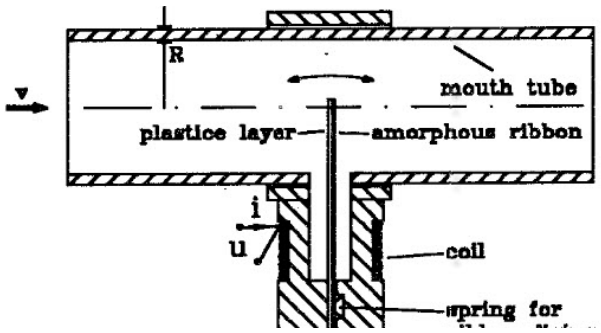


Figure 2.24: The Amorphous Ferromagnetic Materials based spirometer sensor obtained by [19].

and the output voltage is linear. However, the effects of temperature, humidity and density of flow are not discussed in this paper [20].

#### 2.5.1.8 Gas Flow Sensor Based on Sound Generated by Turbulence

This sensor was designed using the principle that locating a tiny obstacle in the flow direction makes turbulence [21]. The turbulences results in pressure variations containing a wide range of frequency components. Since the ultrasonic and audio frequencies are included as well, the idea of detecting the pressure variation using a microphone or an ultrasound transducer emerged. As can be seen in Figure 2.26, a T-shaped tube is used for this sensor and the capacitor type microphone- setting besides the obstacle- receives the audio frequencies which are made by obstacle turbulence. The output of the microphone, AC signal, is amplified and passed through a narrow-band filter. After the signal has passed through a full-wave rectifier and buffer, the average voltage is read by an integrator. Gas flow rate value can be derived from the average voltage after doing linearization and further analysis by means of a computer or microprocessor.

The advantages of this sensor are lack of moving parts, possibility of blocking by existing water drops existing in the expiratory flow, and temperature independency. This sensor, nevertheless, is unidirectional with difficult mathematical modeling. Many parameters, such as tube diameter, size of the obstacle, smoothness of the surface around the microphone, and quality of the microphone affect the turbulence should be considered carefully for calibration. In addition, although the sensor is covered

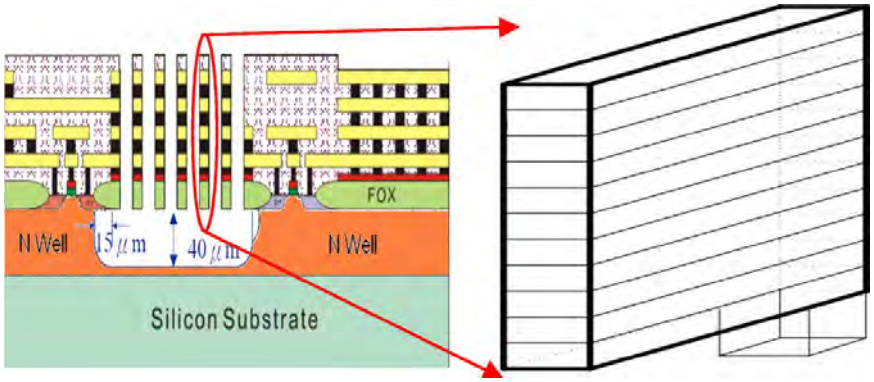


(a)

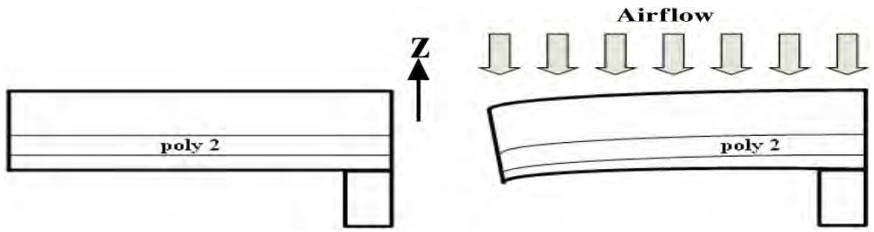


(b)

Figure 2.25: (a) Physical structure of proposed sensor with exaggerated thickness and (b) Deformation of cantilever [20].

by foam to decrease ambient sounds and vibration effects, other noises can result in error and so the test should be performed in a quiet place.

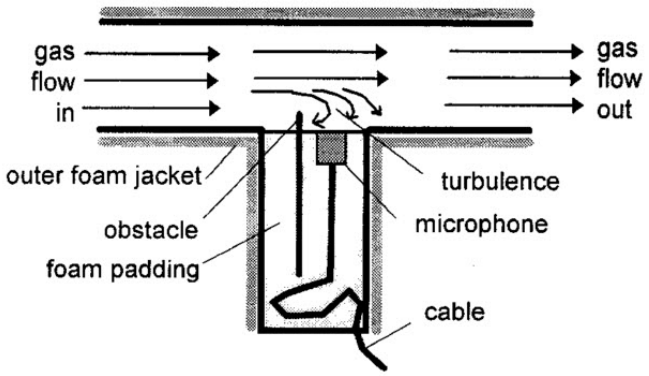


Figure 2.26: Schematic diagram of the flow sensor based on sound [21].

#### 2.5.1.9 Lung Capacity Estimation through Acoustic Signal of Breath

Further research is done to find the lung capacity by means of microphone and breathing sound [60], [61], [62]. In these studies the acoustic signal of respiration is recorded by a microphone. The inspiration and expiration are differentiated through silence detection and so the length of each segment can be measured. The energy of the signal, on the other hand, is being used to detect the flow rate inasmuch as it is a consequence of power and depth of the breath [63]. Figure 2.27 depicts the procedure.

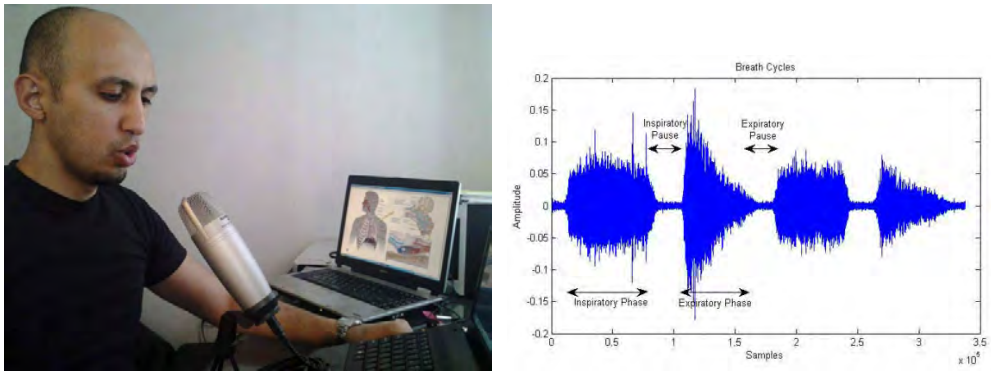


(a) (b)

Figure 2.27: (a) Recording a breathing signal for a subject and (b) Breath cycles showing different phases[63].

The difficulties of this method are its heavy reliance on the voice activity detection algorithm, type/sensitivity of the microphone, and distance from the microphone.

#### 2.5.1.10 Self-power peak expiratory flowmeter

In 2013, Wang et al introduced a peak flow meter based on electromagnetic induction which is shown in Figure 2.28 [22]. The device is made of a small turbo generator through which the air flows and a small amount of electric power is generated. The signal frequency is proportional to the turbine speed. And the speed of turbine is directly related to the air velocity. So using an AVR microcontroller which detects the generator frequency enables measuring the flow rate. The significant feature of the device is that the produced electrical signal can be used to repower the device

batteries simultaneously.

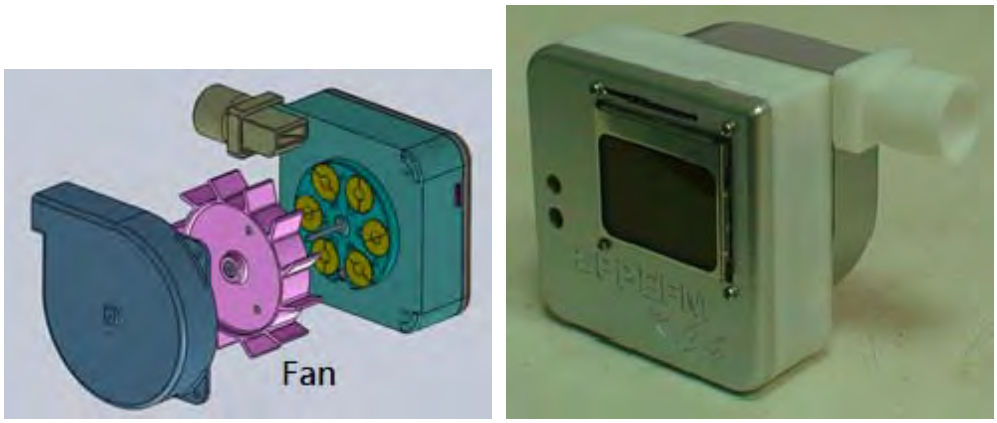


(a) (b)

Figure 2.28: The diagram of the self-power peak expiratory flowmeter. (a) structure and (b) final version of the device [22].

# CHAPTER 3

# THEORY AND DESIGN

This chapter begins with basic design parameters of the first turbine-based MEMS spirometer sensor. In Section 3.1, a general description of theory of operation and governing physics is provided. These concepts are applied to a MEMS frame to design the general device structure. The details of the design of the stator, magnets, turbine blades, and microballs are described in sections 3.2, 3.3, 3.4, and 3.5, respectively.

## 3.1 Principle of Operation

The spirometer sensor described in this thesis is a turbine based MEMS sensor composed of three main components: (i) a turbine with integrated permanent magnets, (ii) two stators with micro-fabricated planar coils for converting turbine rotation into induced voltage through electromagnetic induction, and (iii) ball bearings (Figure 3.1). This would be the first turbine based MEMS spirometer sensor acting as a MEMS-generator simultaneously.

The turbine is designed as tangential, which means that the blades sit on the sides. This design makes the optimum use of the gas momentum since the flow hits only the turbine blades and so enables the rotation in low flow rates. Besides, it permits employing double-layer permanent magnets which are placed inside the trenches on the bottom and top faces of the rotor. Such design enables electro-magnetic transduction using two stators placed below and over the rotor, facing the two permanent magnets layers. This permits exploitation of magnetic flux lines on both rotor sides

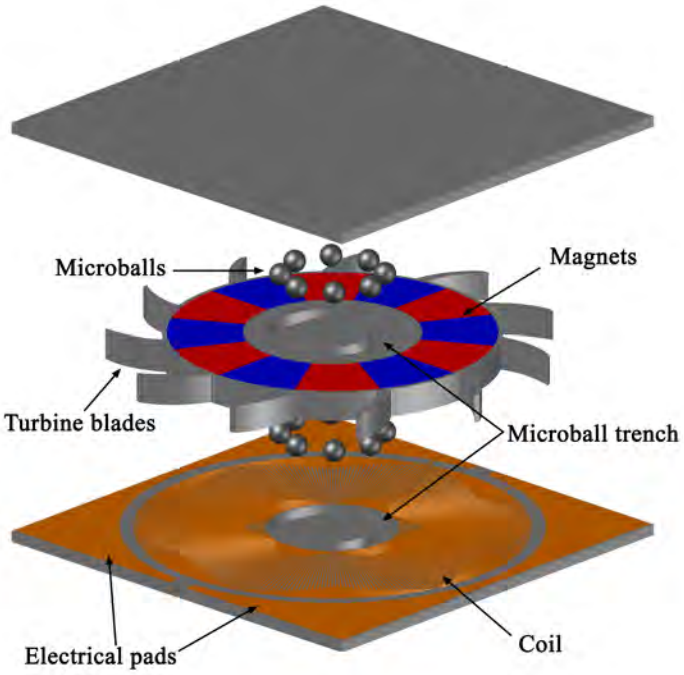


Figure 3.1: Exploded view of the device containing the stators with micro-fabricated coils, the rotor with embedded ring-shaped magnets, microballs, and microball trenches.

at once, and therefore, leads to higher volumetric power density and enhanced performance. Furthermore, in comparison with single-layer magnets with two stators in [64], double-layer design does not need to be secured with heat treatment or compliant rotor substrates, and provides a robust scheme for magnet integration. The magnets are set to be ring-shaped with multiple magnetic poles pairs to supply axial flux to the stator.

In the presence of air flow the turbine rotates and so do the magnets. This rotation around the rotor axis results in a magnetic field along the rotation direction (see Figure 3.2). While the rotor is turning, the stator is fixed, and due to the relative velocity between them a time varying magnetic field will be created, which induces a time varying electric field in the windings. The windings are designed gear-shaped composed of radial and arc-shaped segments.

Due to the fact that the direction of the magnetic flux and arcs are parallel, the voltage

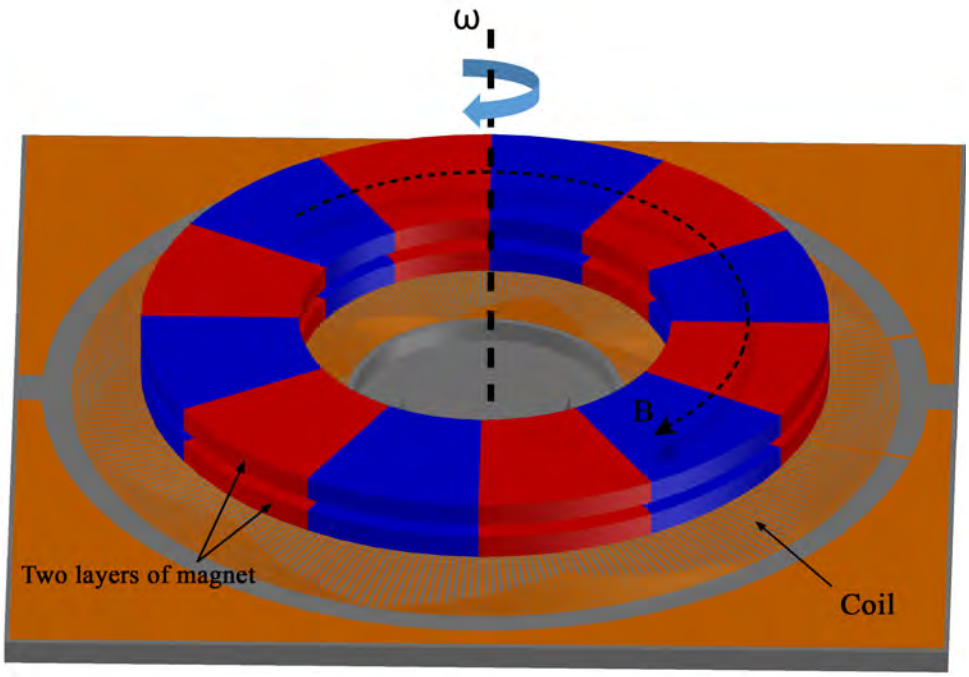


Figure 3.2: The illustration of the two layer magnets n top of the stator coils. When the turbine rotates, a time varying magnetic field (B) along the rotation direction will be created.

is only induced on radial parts. Regarding Faraday's law the generated voltage is calculated by means of the given equation:

$$V = -\frac{d\phi}{dt} \tag{3.1}$$

where $\phi$ is the total magnetic flux crossing the coil and can be obtained as follows:

$$\phi = \int B.ds \tag{3.2}$$

where $B$ is the effective magnetic flux density on the coils. Furthermore, since induction is due to the moving magnetic field, it can be written as:

$$V = \int (v \times B).dl \tag{3.3}$$

This equation is referred to as motional electromotive force or flux cutting electro-

motive force, where $v$ is the relative velocity of the magnetic field with respect to the coils and $L$ is the length of radial lines covered by magnets.

As mentioned before, the magnets are arranged in an alternate polarity. Neglecting the leakage flux, the magnetic flux density along the rotor rotation can be considered as a square wave. Consequently, the induced voltage on radial lines would be a triangular waveform (Figure 3.3).

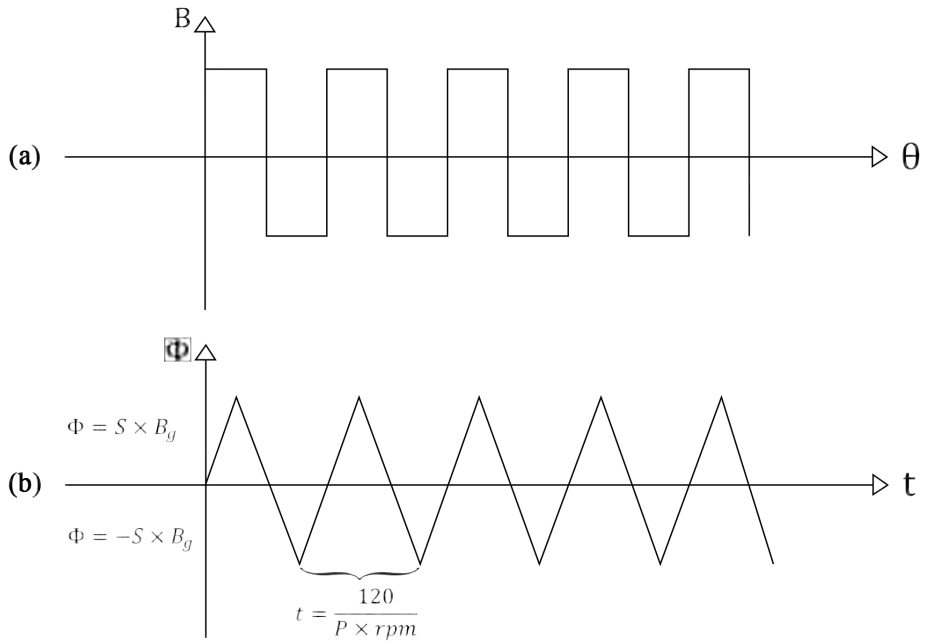


Figure 3.3: (a)Magnetic flux density around the rotor surface (b)Variation of magnetic flux acting on one radial line.

where $S$ is one magnet area, $P$ is the number of poles, and $rpm$ is the turbine angular velocity in rotations per minute. Since there will be $\frac{P}{2}$ triangles in every rotation, the period would be $\frac{120}{(P \times rpm)}$. As a result, eq. 3.1 for one loop in one turn of a pole becomes

$$V_1 = 2 \times S \times B_g \times P \times \frac{rpm}{60} \tag{3.4}$$

The magnet area $(S)$ can be written as $\frac{\pi(r_2^2 - r_1^2)}{P}$ that $r_2$ and $r_1$ are the outer and inner radii of the magnets. Considering the fact that there are $\frac{(P \times N)}{2}$ loops in a coil ($N$ determines number of turns in a coil), the pick voltage of the coils would be equal to:

$$V = \frac{PNB\pi(r_2^2 - r_1^2) \times rpm}{60} \tag{3.5}$$

The same formula can be derived from eq. 3.3. Assuming the turbine rotates with $\omega_r$ angular velocity, the generated voltage on any radial conductor under one pole would be

$$V_1 = \int (v \times B).dl = \int_{r_1}^{r_2} (\omega_r r \times B).dr = \frac{1}{2} B\omega_r(r_2^2 - r_1^2) \tag{3.6}$$

Replacing the angular velocity with revolution per minute ($\frac{rad}{s} = \frac{60}{2\pi} rpm$), 3.6 becomes:

$$V_1 = \frac{B\pi(r_2^2 - r_1^2) \times rpm}{60} \tag{3.7}$$

All these radii are connected to each other in series and as a result, the total voltage of the coil with $N$ turns and $P$ poles will be obtained as eq. 3.4.

The radial lines are designed as the radii of a circle and therefore are arranged physically in different angles. This angular difference results in phase difference of generated voltages on radial parts which lead to the voltage with a gradually increasing profile rather than a square wave, as shown in Figure 3.4, the total voltage will be appeared as a sine wave. The peak voltage of the sine wave will be as given in eq. 3.5.

Both the amplitude and frequency are directly related to the velocity of the blades; nonetheless, it is more common to find the flow rate using signal frequency using:

$$f = KQ \tag{3.8}$$

where $f$, $Q$ and $k$ are output frequency, volumetric flow rate, and $K$ factor of the turbine element, respectively. Finally, the total volume is calculated as the time-integral of volumetric flow rate over a period of time from $t = 0$ to $t = T$:

$$V = \int_0^T Q dt \tag{3.9}$$

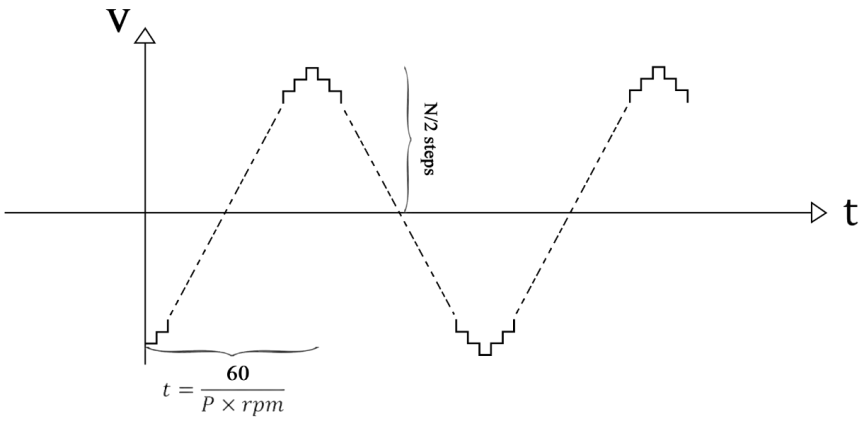


Figure 3.4: Generated voltage waveform of an entire coil under the assumption of perfect magnetization of magnets.

As sensor would be able to convert the mechanical energy into electrical energy, and the delivered power can be calculated as:

$$S = \frac{V_{rms}^2}{Z_L + Z_{coil}} \times Z_L \tag{3.10}$$

where $Z_L$ is the electrical load connected to the coils with $Z_{coil}$ impedance and $rms$ value of induced voltage $V_{rms}$. Due to the Thevenin's power transfer theory, at $Z_L = Z_{coil}$ the maximum power transfer on the load occurs which equals to $\frac{|V|^2}{8R_{coil}}$.

## 3.2 Stator design

The stators are made of a silicon substrate with copper micro coils on the top. And in middle of the coils a circular trench is etched to contain the microballs. Silicon is chosen as the substrate since many surface and bulk silicon micromachining techniques are developed. In addition, Silicon possesses appropriate material properties such as good stability. The micro coils are made of copper which is one of the most common metals being used in MEMS. Furthermore, copper has a low electrical resistivity and hence higher power and voltage can be obtained.

A variety of microcoil shapes have been already developed for in-plain micro-generators. Simple fabrication is one of the most important factors that has been considered in our design and that is why the three phase copper coil pattern [23], [65], [66], as shown

in Figure 3.5, is not chosen for our device.

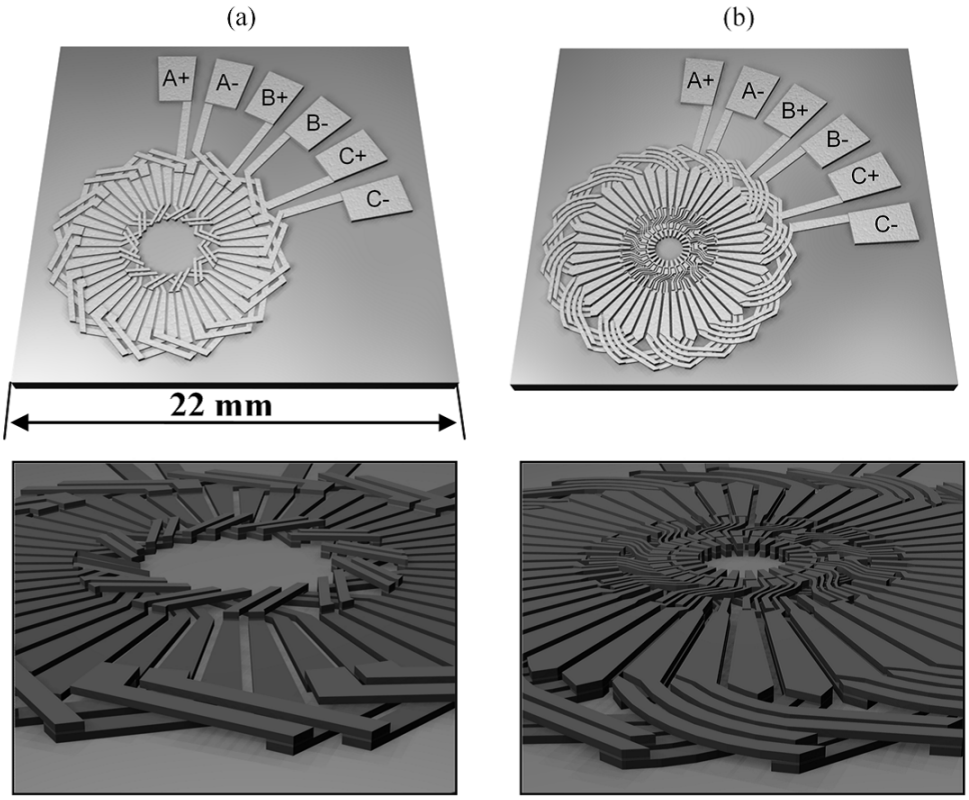


Figure 3.5: Renderings of the three phase stator winding patterns for (a) 2-turn/pole, and (b) 4-turn/pole designs in [23].

The conventional coil patterns have a more simple design that have been used in previous work [67]. Three different shapes of conventional designs (circle-shaped, square-shaped, and sector-shaped) is studied by [24] and the sector-shaped coil is reported as the most efficient one (Figure 3.6).

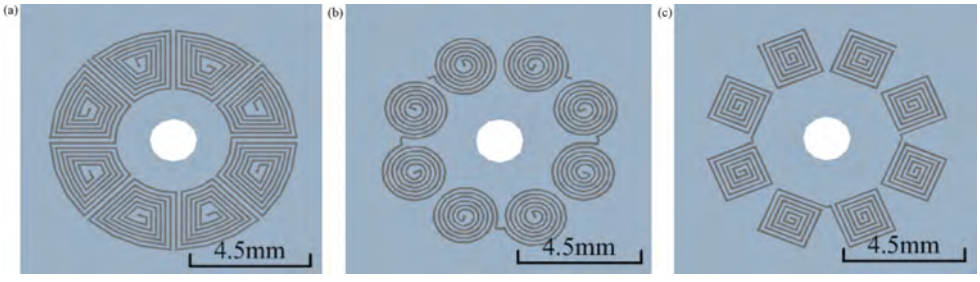


Figure 3.6: Schematic illustration of three kinds of conventional designed micro-coils [24].

The gear-shaped designs are the next generation of microcoils, which are very similar

to the conventional ones. However, due to having less electrical connections the gear-shaped designs benefits from simpler design and easier fabrication [25] (see Figure 3.7).

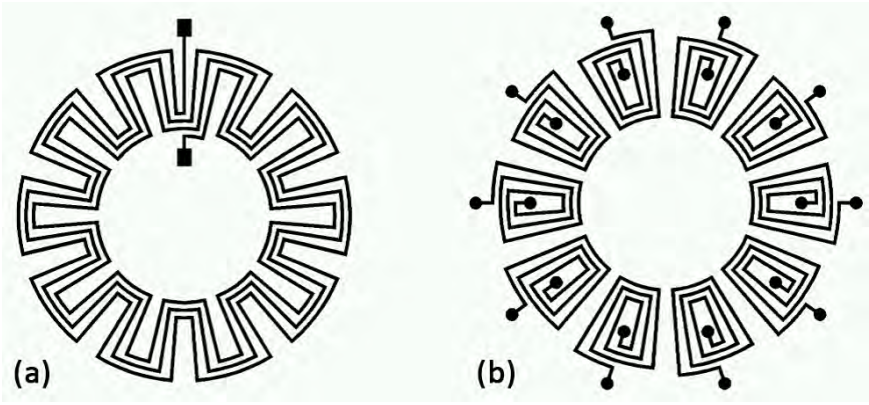


Figure 3.7: The diagram of 3-turn coil designs (a) gear-shaped (b) traditional design [25].

R. Cordero et al have also introduced three different end-turn geometries for gear-shaped coils: sector-shapes, semicircular, and triangular end turns. Patterns of these coils are illustrated in Figure 3.8.

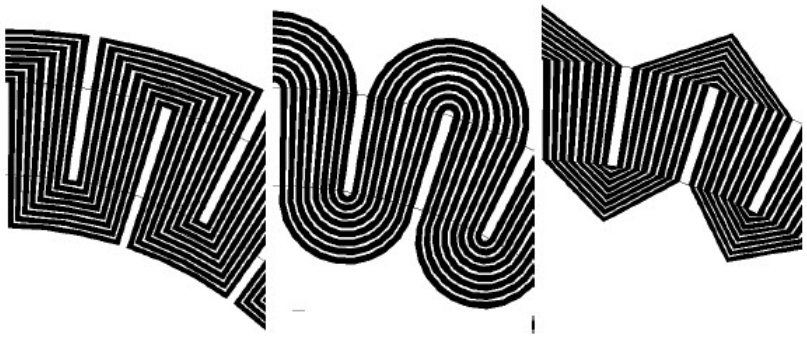

Figure 3.8: Illustration of end turn patterns in gear-shaped coils (a) sector shape (b) semicircular (c) triangular designs [25].

In our study, among the three different end-turn geometries shown in Figure 3.8, sector-shaped is selected due to possessing a more well set structure. Consequently, the coils are designed as gear-sector-shaped, which is one of the standard coil designs in MEMS and has the advantage of precisely controlled geometry. Due to its planar structure, which is adjustable with MEMS principles, it would have an easier fabrication especially in case of electroplating. As seen in Figure 3.7 two electrical pads are

connected to the two ends of the coil to extract the electrical signals.

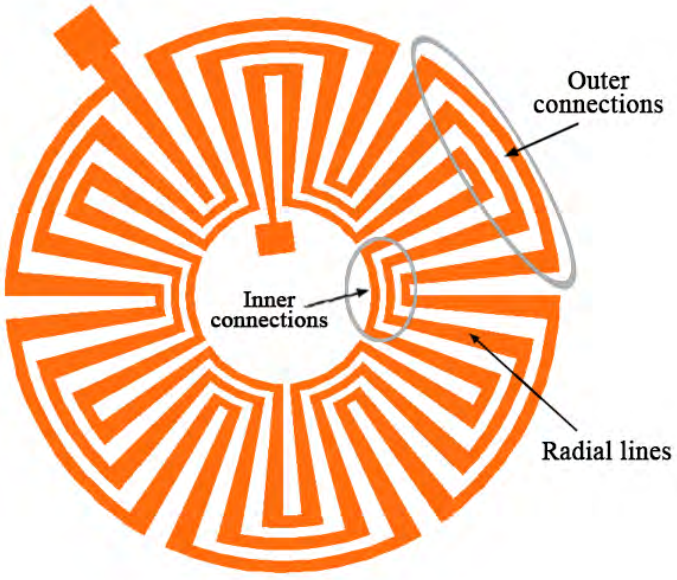


Figure 3.9: The three different segments of the schematic coil.

As shown schematically in Figure 3.9, the microcoils contain radial and arc-shaped parts. When the rotor is rotating, the induced magnetic flux crossing the radial segments will induce electromotive force (EMF) voltages. However, the directions of the arc-shaped segments are parallel to the flux, which will not produce any voltage. The radii are connected to each other by means of arcs and hence the induced voltages are all connected in series that leads to a greater total voltage.

As stated in the eq. 3.5, the induced voltage is proportional to the number of pole-pairs ($p$), wire turns ($N$), turbine velocity, the remanent magnetization ($\beta_z$), and radial lines longitude.

Increasing the number of $P$ and $N$ results in higher voltage amplitude. Nonetheless, incrementing the number of poles also leads to magnetic leakage growth and so decline in the magnetic flux density. Hence, an optimum amount should be found which will be discussed in magnets section.

Moreover, to achieve higher number of turns in coils, the longer and narrower wires should be used which consequently increases the electric resistivity in coils. Due to the electric power formula (3.10), by increasing the number of turns in a limited space, the coil impedance goes up as well. Therefor the greater $N$ would have no

effect on the output power. However, it is best to maximize this product within the fabrication limitations in order to generate power at high voltage and a low current. This will result in less power loss (due to diode voltage drops and $I^2R$) in power conversion and/or extraction electronics.

On the other hand, fabrication limits do not permit to design too narrow wires. Considering the limits, the narrowest part and the smallest gap between the wires are both designed to be $10\mu m$ which belongs to the inner connections. The outer connections are designed as $15\mu m$-thick wires. These considerations lead to have 50-turn coil. Nevertheless, 25-turn coils are also designed with twice wire width to lessen the fabrication risks.

Regarding eq. 3.5, longer radial lines $(r_2^2 - r_1^2)$, the yield greater voltage; nonetheless, fabrication limits would not allow us to increase the radii longitude a lot. Plus, lengthening the radii would raise the coil resistivity but in the lower proportion than that of the voltage. At large, concerning the portability of the device, $r_2$ is limited due to the device size while $r_1$ is limited mostly because of microballs' trench radius. Thus, $r_1$ and $r_2$ are the range of 2.95-3.95 mm and 7.3-8.8 mm, respectively.

## 3.3 Coil design

To model the coil circuit and calculate the generated voltage on the stator coils, the corresponding coil resistance and inductance should be taken into account.

### 3.3.1 Coil resistance

As seen in the Figure 3.9, there are three different segments that should be considered separately when it comes to resistivity calculations. Not only the resistance of radial parts and inner and outer connections need to be calculated separately but also their lengths vary in each turn. Consequently, the resistance of each section should be calculated for each turn distinctively.

While $\int_{r_1}^{r_2} \frac{\rho dr}{2\pi t r \frac{\theta}{360}}$ is used to find the resistance of the radial parts of the coil, the resis-

tance of the inner and outer connections can be found by the formula $\frac{2\pi\rho r\frac{\theta}{360}}{t(r_2-r_1)}$ where $\rho$, $\theta$, $t$, $l$, $r_1$, $r_2$ are the resistivity, conductor angle, thickness, length, inner and outer radii respectively. Therefore the resistance of one loop will be:

$$R_{loop} = \frac{p}{2} \times \Big((2 \times R_{radial}) + R_{innerarc} + R_{outerarc}\Big) \tag{3.11}$$

That is equal to,

$$R_{loop} = \frac{p}{2} \times \Big((2 \times \int_{r_1}^{r_2} \frac{\rho dr}{2\pi t r\frac{\theta}{360}}) + \frac{2\pi r\rho\frac{\theta}{360}}{t(r_{in2}-r_{in1})} + \frac{2\pi r\rho\frac{\theta}{360}}{t(r_{out2}-r_{out1})}\Big) \tag{3.12}$$

Adding all loops resistivites will be resulted in the total resistance of the coil. However, to simplify the calculations while having a good estimation of the coils resistivity, we can obtain the mean length of each segment to avoid repeating the calculations for each turn.

While precise calculation is very time-consuming, using mean length for arcs and radii would lead to an accurate enough estimation of coil resistances. As mentioned, the inner and outer connection radii vary from 2.95 to 3.95 and 7.3 to 8.8 mm respectively. Therefore, we can consider 3.45 and 8.05 mm as mean for inner and outer radii. The copper wire thickness is designed to be $20\mu m$. Consequently, each segment resistivity would be:

$$R_{innerarc} = \frac{2\pi \times 3.45 \times 10^{-3} \times 1.68 \times 10^{-8} \times \frac{30}{360}}{20 \times 10^{-6} \times 20 \times 10^{-6}} = 45.5\Omega \tag{3.13}$$

$$R_{outerarc} = \frac{2\pi \times 8.05 \times 10^{-3} \times 1.68 \times 10^{-8} \times \frac{30}{360}}{20 \times 10^{-6} \times 20 \times 10^{-6}} = 53.1\Omega \tag{3.14}$$

$$R_{radial} = \frac{1.68 \times 10^{-8}}{2\pi \times 20 \times 10^{-6} \times \frac{1/3}{360}} \times (\ln 8.05 - \ln 3.45) = 73.4\Omega \tag{3.15}$$

Due to the fact that the 50-turn coil contains 600 radial segments and 300 inner and outer connection segments, the total coil resistivity will be $45.5\Omega + 53.1\Omega + 73.4\Omega = 172\Omega$. And the 25-turn coils resistance will be $43\Omega$.

### 3.3.2 Coil inductance

The inductance of the coils can be found by calculating the inductance of each loop of the coil and multiplying it by total number of loops using following equation:

$$L_{loop} = \frac{\phi}{I}$$

where $\phi$ is amount of the flux passing through the loop generated by the coil current. However, due to complex geometry of the loops, which have different size in each turn of the coil, it is difficult to calculate the coils inductance. In addition, to the inductance of each loop, there are mutual inductances between different loops. Therefore, since both the calculation and the simulation of this effect is computationally complex, the total inductance will be determined experimentally.

### 3.3.3 Coil capacitance

In order to calculate the highest possible capacitance of the coil, here we have assumed that all coil lines are in parallel, which yields;

$$C = \frac{N\epsilon A}{d} \approx 2.5\text{fF}$$

where $N = 50$, $A = 20 \times 10^{-6} \times 300 \times 10^{-9}$, and $d = 30\mu m$. Considering 10kHz as the maximum frequency will be obtained with the device, the corresponding parallel impedance will be;

$$Z = \frac{1}{2\pi f C} \approx 6.4 \times 10^{9}$$

,

As can be seen this is ten orders of magnitude higher than that of calculated impedance, and hence negligible.

### 3.4 Magnets design

The permanent magnets are chosen to be off-the-shelf NdFeB components which can supply 1.4T magnetic flux density. The pole pairs are embedded inside the ring-shaped trenches on both sides of the turbine. Number of magnetic poles is a crucial factor for an efficient transduction and hence obtaining the maximum flux density in a given device geometry. High pole numbers increase the total leakage flux between adjacent poles that do not penetrate through the stator, while low numbers of poles result in a long azimuthal flux path, and consequently a significant magnetic reluctance (see Figure 3.10). Therefore, using lower or higher than an optimal number of poles would cause a decrease in the average flux density acting on the stator surface. Because of the nonlinearity of the problem and its three dimensional geometry, $B_{avg}$ maximization and pole numbers optimization by means of analytical solution for magnetic flux density is difficult. That is why in order to reveal the magnetic flux density distribution within the device, numerical analysis has been conducted in AC/DC module of the COMSOL finite element simulation software.

Specifically, magnetic fields —no currents interface was used, which solves the general equation:

$$\bigtriangledown.(\mu_0 \bigtriangledown V_m - \mu_0 M_0) = 0 \tag{3.16}$$

where $\mu_0$ and $V_m$ are permeability of free space and scalar magnetic potential respectively. And $M_0$ is the magnetization vector within the corresponding material domains. Subsequently, the average flux density on the stator surface that is provided by one magnet pole was then obtained by

$$B_{avg} = \frac{1}{A} \int B_z \times dA \tag{3.17}$$

where $B_z$ is the axial magnetic flux density obtained by simulations and $A$ is the projection of one magnet area on the stator surface. Due to the fact that the problem possesses azimuthal symmetry, all other magnets provide the same $B_{avg}$ with alternating polarity under their corresponding $A$.

The simulations have been performed to find the optimum $p$ in range of the design geometry, where the varying parameters include the thickness and inner and outer radii of the ring-shaped magnets. Based on a recent work by [36], for a given magnet area the thinner the magnets are, the higher number of poles are desirable. That is why the thickness of magnets is chosen to be $500\mu m$. Consequently, the best $p$ has been revealed for different combinations of $r_{out}$ and $r_{in}$. The parameter values used in the simulations are listed in Table 3.1.

To boost $B_{avg}$, the air gap between the magnets and coils on the stator is desired to be as small as possible. That is why concerning the manufacturing and testing constraints, it is set to be $50\mu m$.

Table 3.1: Parameters used in the simulations

| Parameter | Value |
|---|---|
| Magnet thickness, $t_m$ | $500\mu m$ |
| Outer radius, $r_{out}$ | 7.25-7.5-7.75 mm |
| Inner radius, $r_{in}$ | 3.25-3.5-3.75-4 mm |
| Air gap | $50\mu m$ |

The simulation first is done on the most basic model with two poles ($r_{out}$=7 mm, $r_{in}$=3 mm). It shows that the highest flux density is equal to 0.409 T whilst the average flux density decreases to 0.137 T (see Fig. 3.10). This difference is mostly due to the large reluctance which has the maximum value in central part of the magnets. Figure 3.11 depicts the diminishing effects of leakage fluxes and large reluctance on average flux density, and shows that the resulting optimum pole numbers for the same geometry is 34.

The same simulations were performed for all the parameters listed in Table 3.1, and the resulting optimum pole numbers with their corresponding $B_{avg}$ are listed in Table 3.2.

Regarding the simulation results maximum $B_{avg}$ is obtained as $0.452T$. In addition at optimality, $r_{in} = 4mm$ and $r_{out} = 7.25$, in which the maximum $B_{avg}$ is drived by the least number of $P$ .

However, the company were not able to provide the required number of magnet poles.

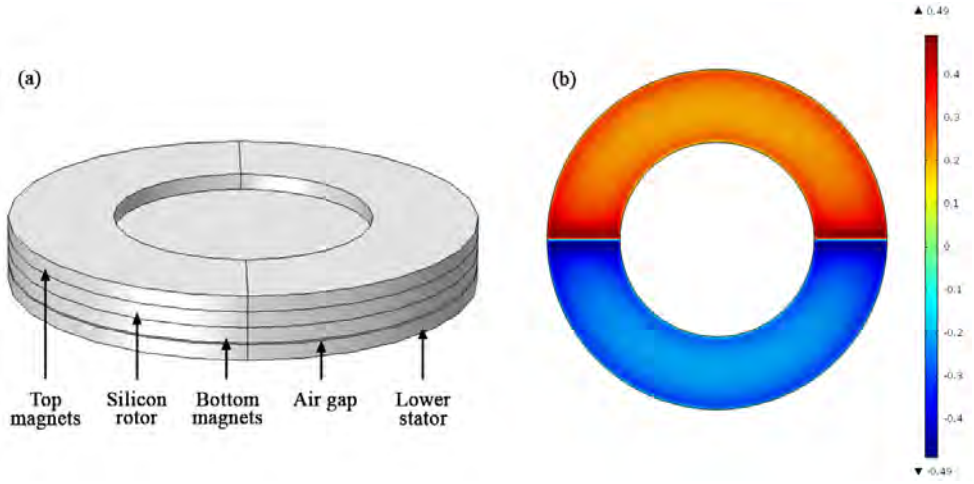


Figure 3.10: (a) Simulation model for $P = 2$, $t_m = 500mm$, $r_{out} = 5mm$, $r_{in} = 2mm$. (b) distribution of flux density above the stator surface.

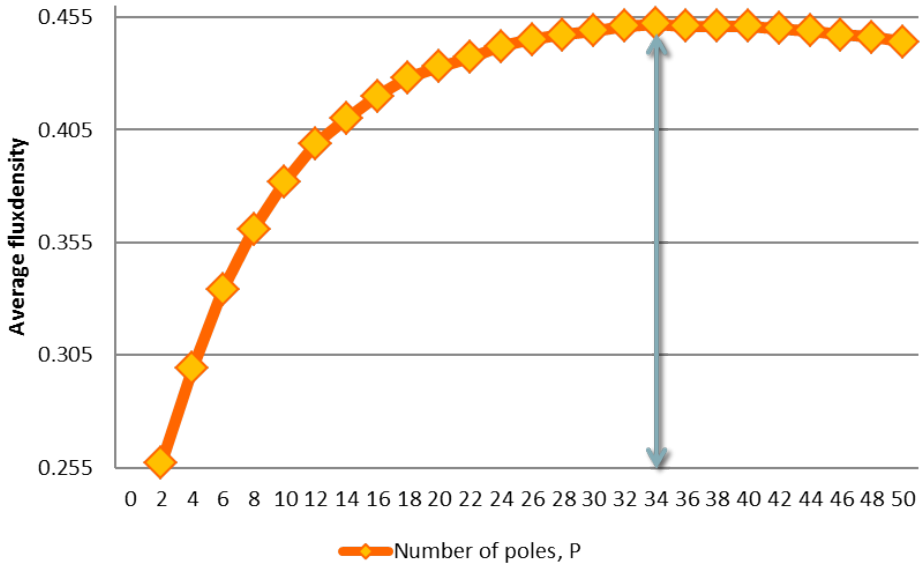


Figure 3.11: $B_{avg}$ versus $P$ showing the ranges where flux leakages and large reluctance are dominant and the number of poles at which the $B_{avg}$ is maximum.

Therefore, the highest number of poles that could be acquired and fit into our design, considering its size and geometry, is 12. Moreover, magnets with smaller inner radius would cover longer radial lines that would result in a higher induced voltage in coil. However, due to the fact that narrow boundary wall between the ball grooves and magnet trenches on the rotor can complicate the rotor fabrication process, the magnet inner radius is chosen to be 4mm. The magnet outer radius, on the other hand, are

Table 3.2: Simulation results for maximum $B_{avg}$ and corresponding optimum number of P in range of Device geometry.

| $r_{in}$ | $r_{out}$ | Optimum $P - B_{avg}$ |
|---|---|---|
| 3.25 mm | 7.25 mm | 34 - 0.451T |
| | 7.5 mm | 36 - 0.451T |
| | 7.75 mm | 36 - 0.451T |
| 3.5 mm | 7.25 mm | 38 - 0.451T |
| | 7.5 mm | 38 - 0.452T |
| | 7.75 mm | 36 - 0.451T |
| 3.75 mm | 7.25 mm | 38 - 0.452T |
| | 7.5 mm | 40 - 0.451T |
| | 7.75 mm | 36 - 0.451T |
| 4 mm | 7.25 mm | 34 - 0.452T |
| | 7.5 mm | 40 - 0.451T |
| | 7.75 mm | 38 - 0.452T |

chosen to be 7.25mm to have a longer turbine radial blades, which inhances the fluidic performance of the device.

### 3.5 Turbine blades design

The shape, length, and number of turbine blades have been optimized to maximize the induced moment and rotational speed at normal breathing flow rates and hence improving the voltage induction and sensor resolution. Based on the stator and magnets design reported in previous sections, the turbine blades are located between $r_{in} = 7.5mm$ and $r_{out} = 10mm$, leading to a radial blade length of $r_l = 2.5mm$, which is shown in Figure 3.12. The turbine blades parameters have been optimized using COMSOL finite element analysis and have been determined to be circular, straight and involute-type with 12, 8, and 11 blades respectively.

### 3.6 Microballs design

Microballs are one of the different types of bearings in MEMS which possess a low wear and friction (less than $10^{-4}$ $\mu$Nm/rpm, coefficient of friction torque) compared

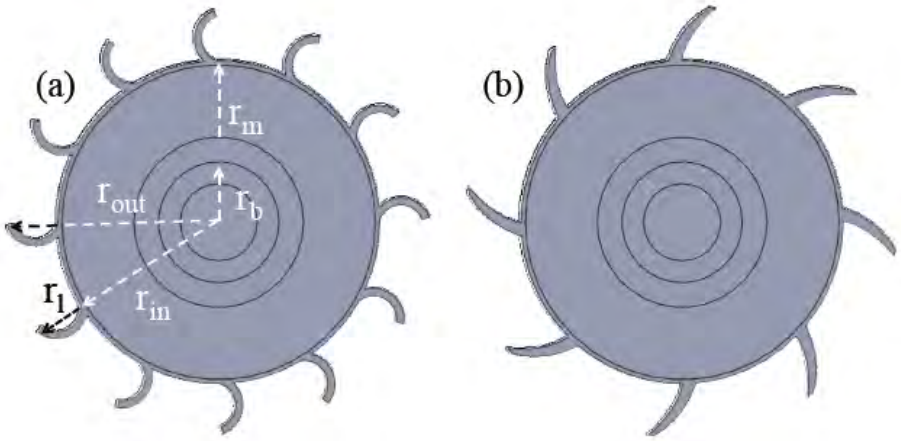


Figure 3.12: Turbine designs with (a) circular-type blades showing relevant dimensions, and (b) involute-type blades with the same dimensions [26].

to contact and liquid film bearings. In addition, since microballs contact directly with both the stator and rotor, they provide a strong support and a better stability than gas lubricated bearings or magnetic/electrostatic levitations. These factors are all crucial for the performance and lifetime of dynamic MEMS devices.

To minimize the wear problem, the microballs should have a close Young's modulus to that of the silicon. While steel is a very good choice regarding the Young's modulus, the microballs are selected to be made of SiN due to its magnetic property. In our study off-the-shelf SiN microballs with a diameter of 1mm are being used.

# CHAPTER 4

# FABRICATION

This chapter illustrates the microfabrication details of the sensor and related issues. Fabrication has been one of the most challenging aspects of this work due to the lack of pre-experiences and frequent microfabrication tool breakdowns. The MEMS sensor shown in Figure 3.1 is fabricated from two stators and a rotor in the middle along with microball bearings, which are sandwiched between the rotor and stators. The process flow of the sensor used a total of 7 masks. The stator and rotor part are separately fabricated through 5-mask and 2-mask micromachining process respectively. In this project I have worked on the stator part of the sensor which its fabrication benefits from both bulk and surface micromachining.

Section 4.1 introduces thebasic microfabrication processes. Sections 4.2 and 4.3 describe the designed fabrication steps of the stators and design process of the stator masks respectively. Sections 4.4, 4.5, 4.6, 4.7, and 4.8 present the details of the each step of the fabrication process which are patterning the alignment marks and stators' outer frame, deposition of the coils, deposition of the insulation layer, deposition of the electrical pads, and balls groove etching respectively. Finally a brief summary and suggestions for future improvements are given in Section 4.9. Detailed process travelers are listed in Appendix.

## 4.1 Introduction to the basic microfabrication

The term micromachining refers to the fabrication of microelectromechanical devices and, in particular, miniaturized sensors and actuators. And silicon micromachining as

the most advanced micromachining technologies consists of two main technologies: bulk micromachining, in which structures are fabricated through etching techniques to remove part of the silicon substrate and surface micromachining, in which the micromechanical layers are made from deposited thin films on the surface.

Bulk micromachining is one of the most commonsilicon micromachining technologies that permitsselectively etching into the silicon wafer to form microstructures such as a variety of trenches and holes. There are several silicon etching methods, which can be divided into wet etching and dry etching based on the phase of etchants. While vapor and plasma etchants are referred to as dry etching, wet etching is done by liquid etchants. Wet etching, known as conventional etching method, is mostly applied to the back side of the wafer whilst the plasma etching is done in the front side. Both wet and dry etching of the silicon can be considered to be either isotropic etching or anisotropic etching.

Wet etching is done by putting the silicon wafer into an etching bath or spraying the etchants over the substrate. Isotropic wet etching is not directional, which means, the etch rates are the same for all directions in the silicon. However, anisotropically etching speed is determined by the crystal's orientation, in which the etch rate decreases considerably at the (111) planes, relative to other silicon planes. Different etching structures of isotropic and anisotropic wet etching are illustrated in Figure 4.1.

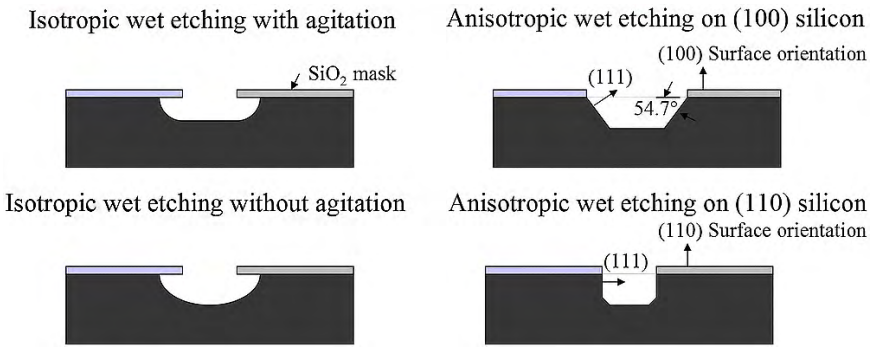


Figure 4.1: Illustration of the etched profiles using isotropic and anisotropic etching retrieved by [27].

Dry etching occurs through physical and/or chemical interaction between the gas ions and the atoms of the substrate. Plasma etching and reactive ion etching (RIE) are the most common dry etching techniques of bulk silicon. Due to less chemical contami-

nation and geometry flexibility anisotropic dry etching technique is broadly employed in MEMS. DRIE process is cyclic, consisting of a brief etch step followed by side-wall passivation which enables high aspect ratio deep silicon microstructures. DRIE employ the same basic RIE technology, but also uses special gas chemistry to form a thin layer of polymer on the sidewalls to prevent lateral etching. Figure 4.2 depicts anisotropic DRIE process.

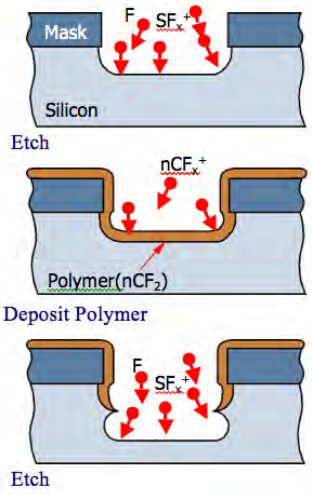


Figure 4.2: Illustration of how deep reactive ion etching works [28].

Unlike the bulk micromachining, which fashion the bulk silicon, in surface micromachining the microstructures are built on the surface of the substrate. The process is done by depositing and patterning thin film of “structural layers" on top of “sacrificial layers". The sacrificial layers are eventually removed to release the structures. Figure 4.3 briefly describes the basics of surface micromachining.

Metals are one the most versatile classes of materials that are used in various MEMS devices. Thin metallic films can be deposited via many different techniques. We can categorize the metal deposition techniques into chemical vapor deposition (CVD), physical vapor deposition (PVD), and electrochemical deposition (ECD). However, since PVD is being performed in lower process temperature compare to PVD and a wide range of materials can be deposited via PVD technique, the CVD method is not discussed.

PVD methods are based on the physical transference of metal atoms from a metal source to the wafer substrate. Thermal evaporation, e-beam evaporation, and sputter-

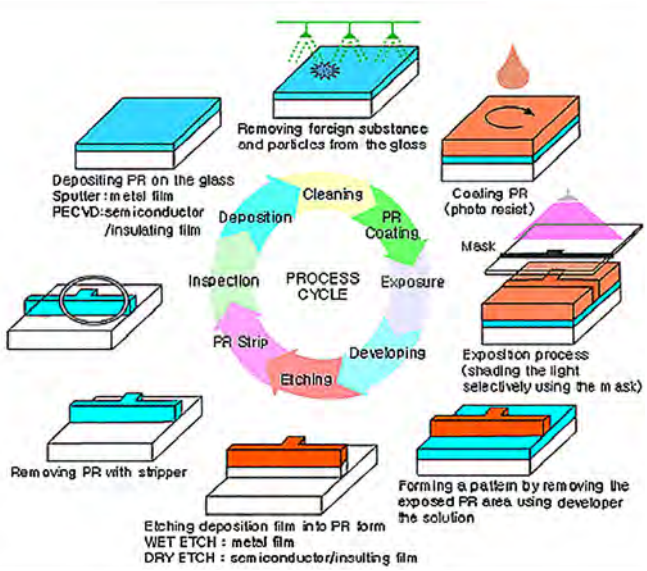


Figure 4.3: Illustration of a surface micromachining process [29].

ing are known as the common metal deposition methods in MEMS fabrication where deposition is done physically. While in thermal evaporation the metal evaporation is done through heating the metal source up, in e-beam evaporation this is done through bombarding the metal source by means of electron beams. In sputtering, however, target is bombarded by accelerated ions; usually Ar+ that are ionized via applying bias voltage between the cathode and the anode. As a result, momentum exchange occurs between the atoms of the target surface and the ions and so the metal atoms are evaporated. All these processes are mostly performed inside a vacuumed chamber. In contrast to the evaporation method, sputtering can provide good step-coverage which means the wafer surface along with sidewalls can be covered more uniformly. Nevertheless, evaporation causes higher film purity than that of sputtering. The uniform and non-uniform coverage are shown in Figure 4.4.

Unlike PVD techniques, ECD methods, which invlove electroless plating and electroplating, are based on chemically growing the metals that allows selective deposition. While electroless plating and evaporation are more preferable methods for thinner films deposition, sputtering and electroplating are better suited for thicker films. In electrochemical deposition an electric current is applied to two electrodes placed inside an electrolyte. Consequently, reduction occurs at the cathode, and oxidation takes place at the anode. In electroplating the wafer substrate plays as the cathode,

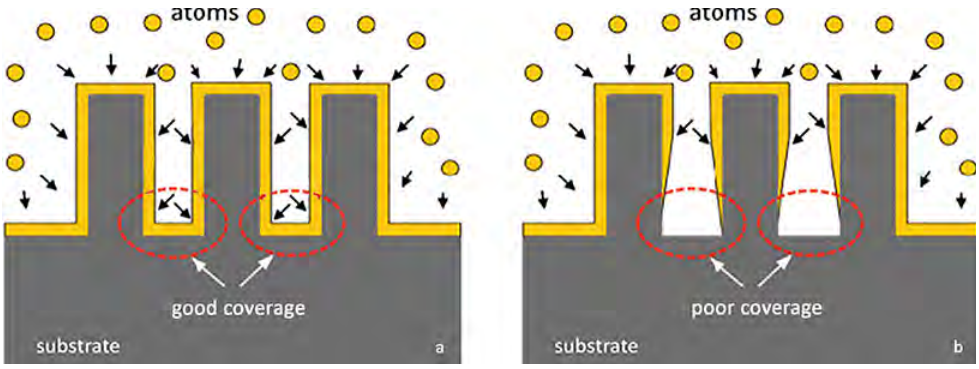


Figure 4.4: Step coverage of deposited films with (a) uniform coverage (b) nonconformal step coverage [30]

and metal ions are reduced to make a solid lattice. A simple diagram of electroplating process is shown in Figure 4.5.

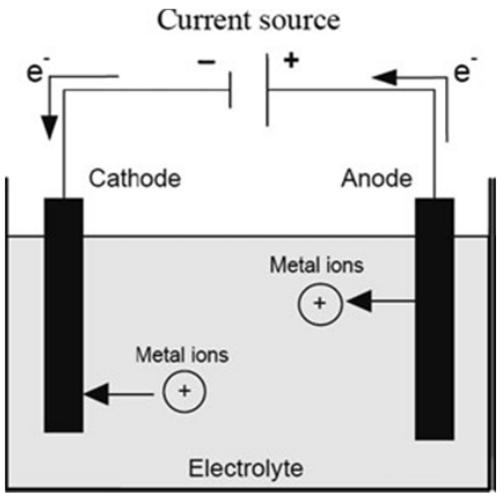


Figure 4.5: Schematic of a general electrochemical deposition cell [30]

In addition to the etching process for metal layers, lift-off process is also employed for patterning the deposited films. During this process, metal is deposited on top of a patterned sacrificial layer. The sacrificial layer is then dissolved in a solvent and hence parts of the deposited layer on top of the sacrificial layer will float away as well. Therefore the film is patterned without any etching process. To achieve a proper lift off, the deposited layer need to be discontinuous at the edges of the opening in the patterned photoresist.Hence the sidewall profile of the photoresist should be undercut. That is why, positive photoresists with image reversal or negative photoresists, which inherently have undercut profiles, work best for liftoff applications. This is illustrated

in Figure 4.6.

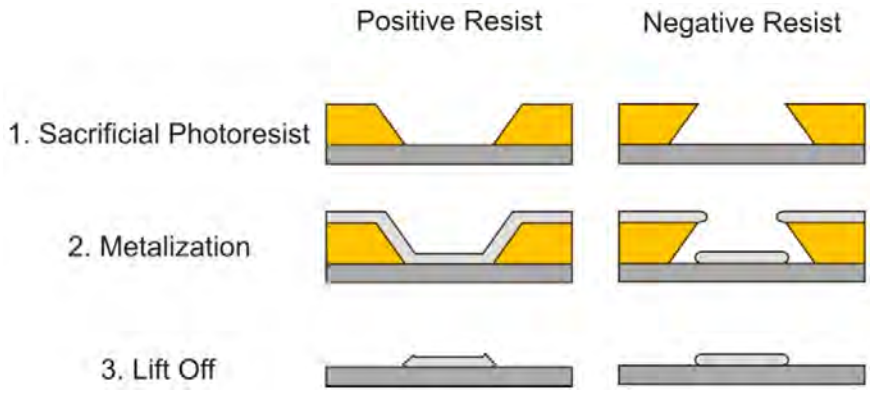


Figure 4.6: A schematic outlining the stages of the lift off process with both positive and negative photoresists with exaggerated sidewall angles [27]

## 4.2 Designed fabrication steps

The aim of the fabrication is to achieve two stators that contain copper coils,electrical pad connections on top of an isolation layer connected to the two ends of the coil, and the microballs groove at the center (Figure 4.7).

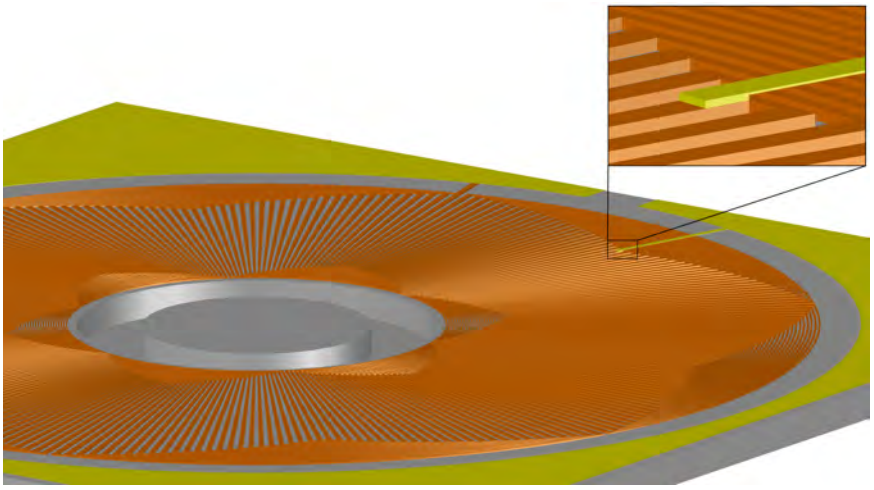

Figure 4.7: An illustration of the stator contains in-plain coils, electrical pads, and the microballs trench. Also a close view of the connection of the pad to one end of the coil is shown.

The stator fabrication was designed to be carries out through 5 main processes: Etching the alignment marks and stators' outer frame, electroplating the copper coils,

Lithography the isolation layer, depositing the copper pads, and DRIE etching the microballs' groove. The fabrication steps are shown in Figure 4.8. The designed process flow is described in details in following.

The starting substrate is a $500\mu m$-thick single-side polished silicon wafer with $2\mu m$ SiO2 on its both sides (see Figure 4.8(a)). The first mask pattern contains the alignment marks and stators' frame. The first step is etching and patterning the SiO2 layer and front side of the Si wafer. To achieve this, the wafer is first coated with a photosensitive material (photoresist) as the sacrificial layer (see Figure 4.8(b)). The photoresist is then exposed through the mask to UV light and developed in developer solution (see Figure 4.8(c)). Afterwards, the SiO2 layer is etched through an isotropic wet etching, in which the patterned photoresist acts as a mask during the process (see Figure 4.8(d)). To etch the Silicon, DRIE method is used to provide anisotropic vertical etching (see Figure 4.8(e)). Finally, the sacrificial layer (photoresist) is removed in Acetone (see Figure 4.8(f)).

The next step includes coils deposition. This step begins with deposition of a thin layer of chromium and copper as seed layer (see Figure 4.8(g)). The chromium is deposited under copper to boost the copper adhesion to the wafer's surface. Since sputtering provides a better uniformity, it is preferable to employ sputtering for metal deposition. A thick layer of photoresist is then deposited and patterned by exposing through the second mask (see Figure 4.8(h)). Next copper coils are electroplated (see Figure 4.8(i)). This step finishes with removing the sacrificial layers by stripping the photoresist in Acetone and wet etching a thin layer of copper to remove seed layer (see Figure 4.8(j)).

Third step is deposition of an insulation layer. A thick layer of SU-8, which is a photosensitive material, is deposited via spin coating and patterned in developer solution after UV exposure through the third mask (see Figure 4.8(k)).

During the next step, first of all a thin layer of copper is coated via sputtering (see Figure 4.8(l)). This layer is shaped via wet etching, in which a photoresist layer is used as the mask during etching process (see Figure 4.8(m)). The electrical pads mask is employed to pattern the photoresist at this step. The mask layer is removed at the end. Finally, ball grooves and outer frames are etched deeply into the silicon. Since

anisotropic etching is required, DRIE method is utilized to achieve vertical trenches. A very thick layer of photoresist acts as the mask for DRIE process. These steps can be seen in Figures 4.8(n), 4.8(p) and 4.8(q).


(a) The Si wafer with $2\mu m$ SiO2 layer


(b) The positive PR is spin coated on top of the wafer.

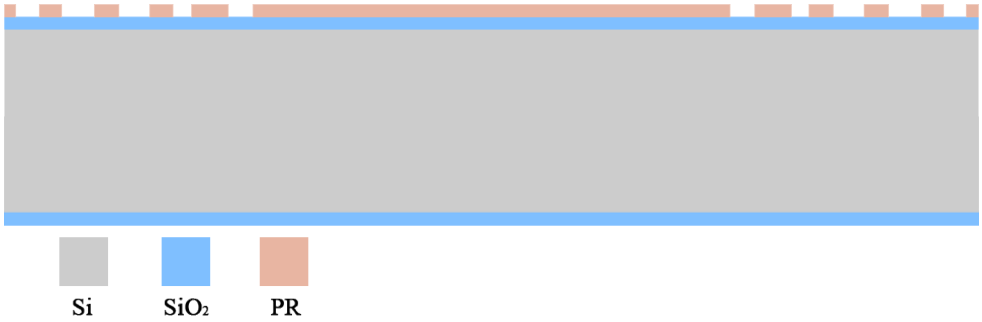


(c) The PR is pattern by UV exposure through 1st mask.

Figure 4.8: Designed fabrication flow process

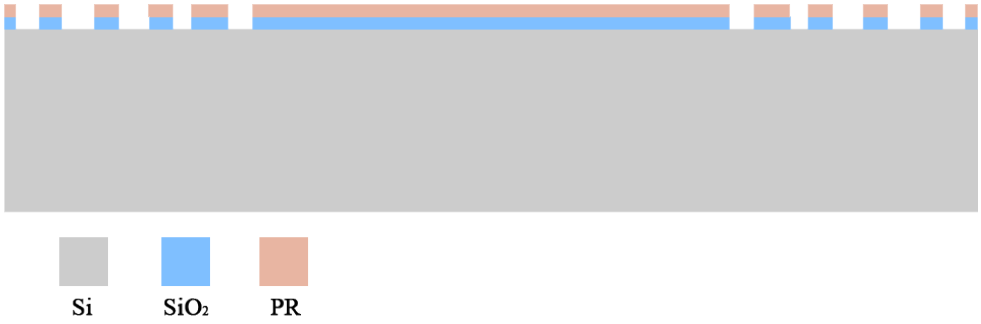


(d) The $SiO_2$ is patterned using wet etching.

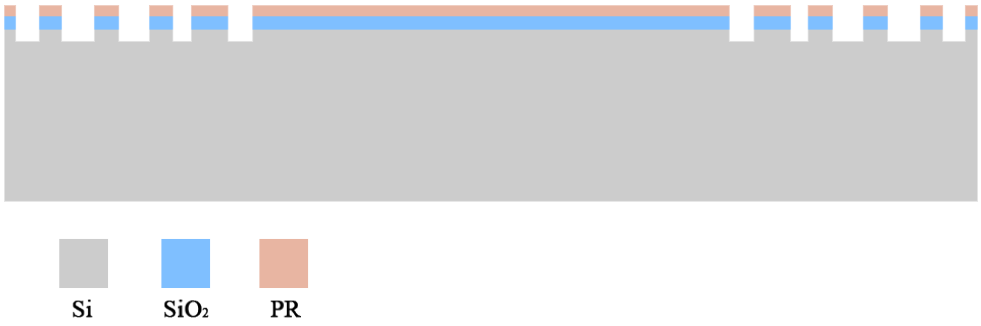


(e) The Si is etched using DRIE method

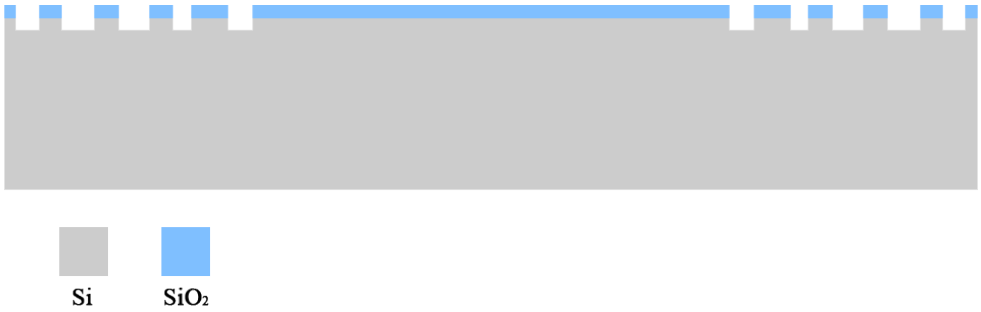


(f) The PR is removed in acetone.

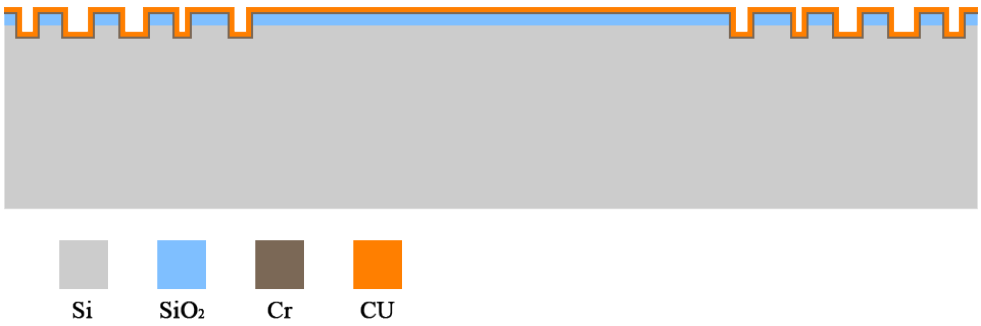


(g) A thin layer of Cr and Cu is deposited as seed layer.

Figure 4.8: Continued

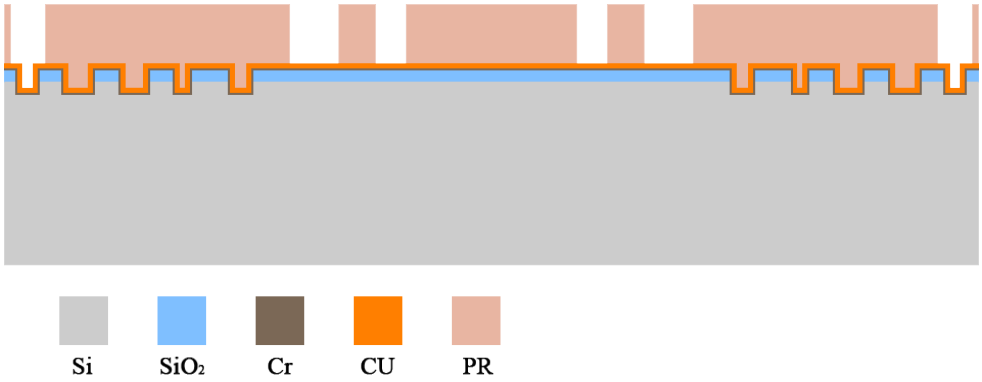


(h) A thick layer of positive PR is patterned through 2nd mask on top of the seed layer.

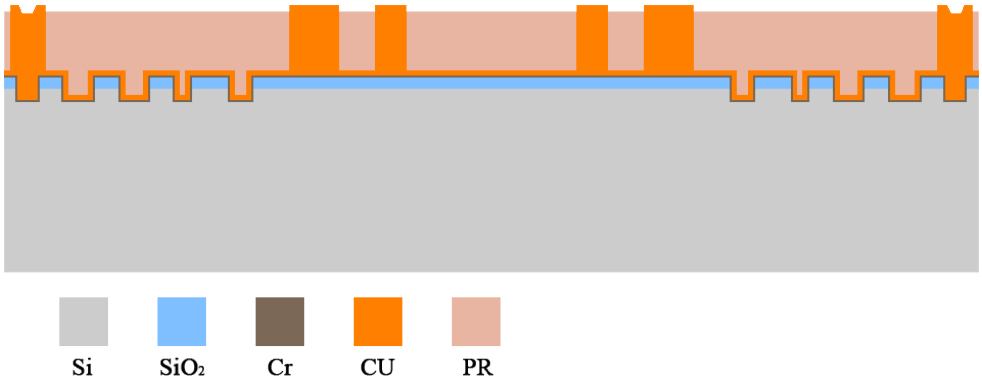


(i) The Cu is deposited through electroplating.

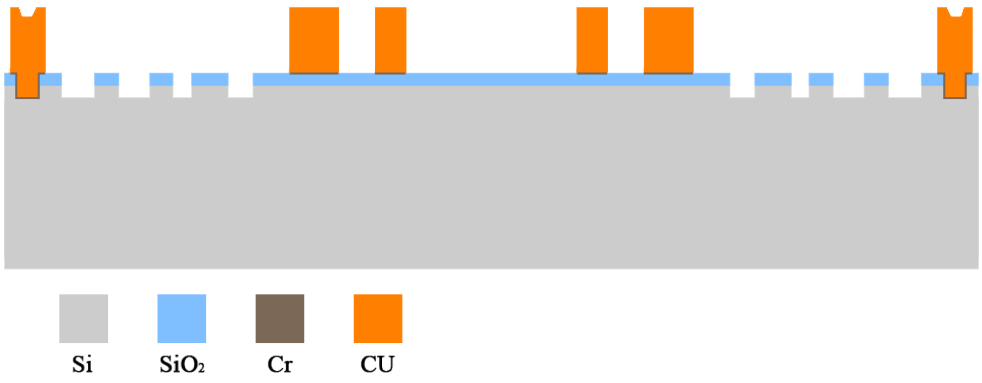


(j) The PR is removed in acetone and a thin layer of Cu is etched by wet etching.

Figure 4.8: Continued

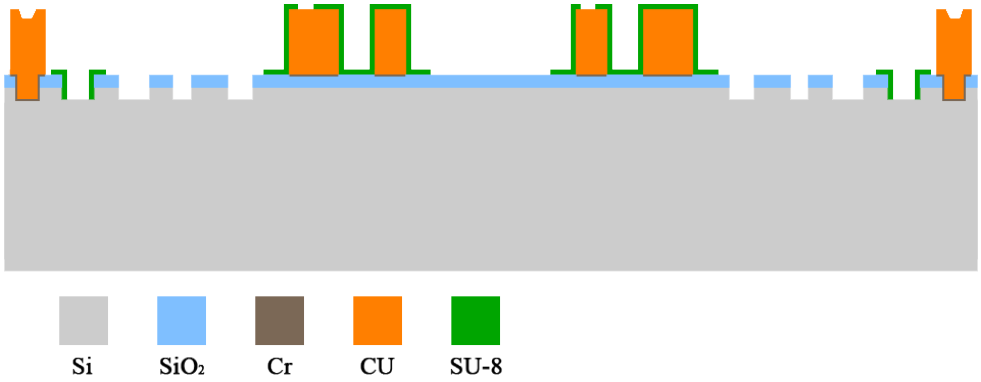


(k) The SU-8 is deposited and patterned as insulation layer using 3rd mask.

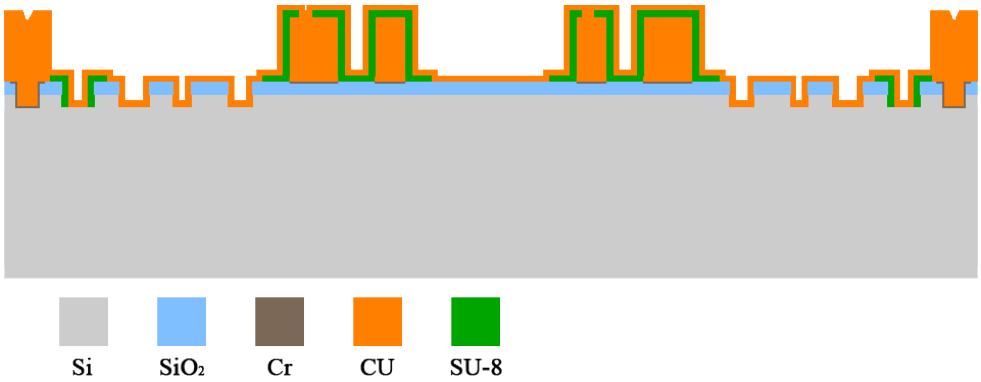


(l) A layer of Cu is deposited on the wafer as the electrical pad layer.

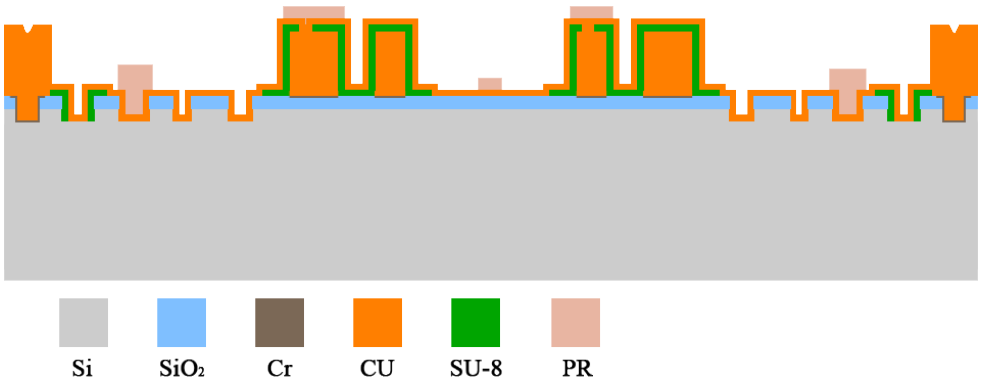


(m) The deposited positive PR as sacrificial layer is patterned through 4th mask.

Figure 4.8: Continued

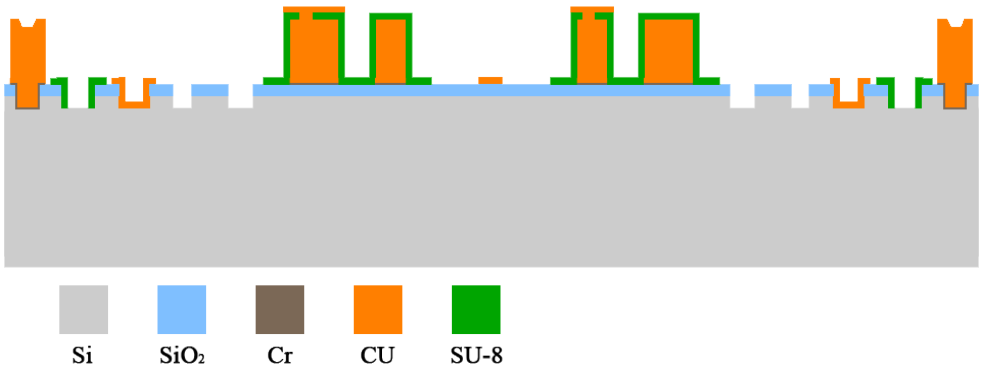


(n) The top Cu layer is patterned by wet etching and the PR is removed in acetone.

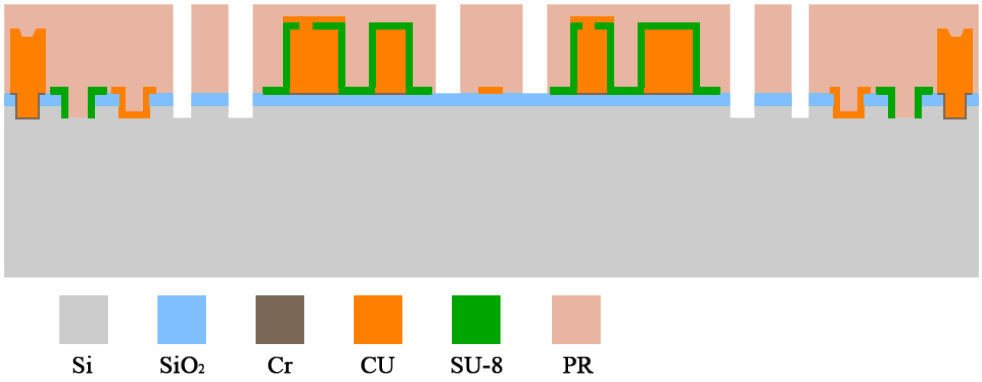


(o) A thick layer of positive PR is deposited and patterned as the mask for DRIE.

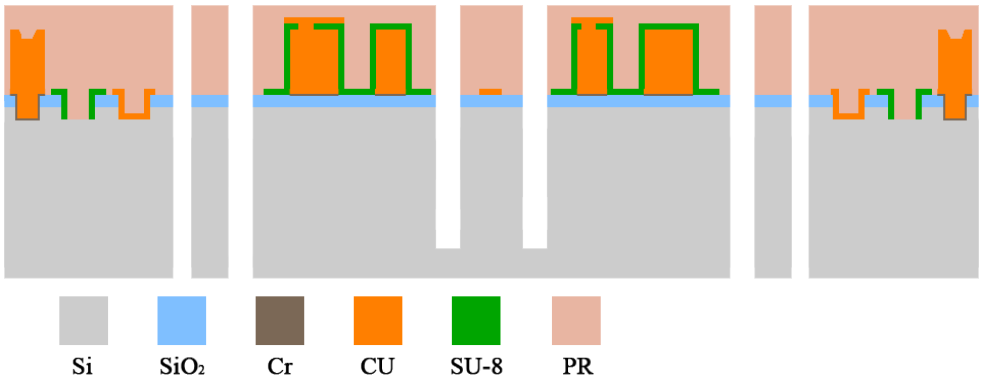


(p) The Si is etched by means of DRIE.

Figure 4.8: Continued

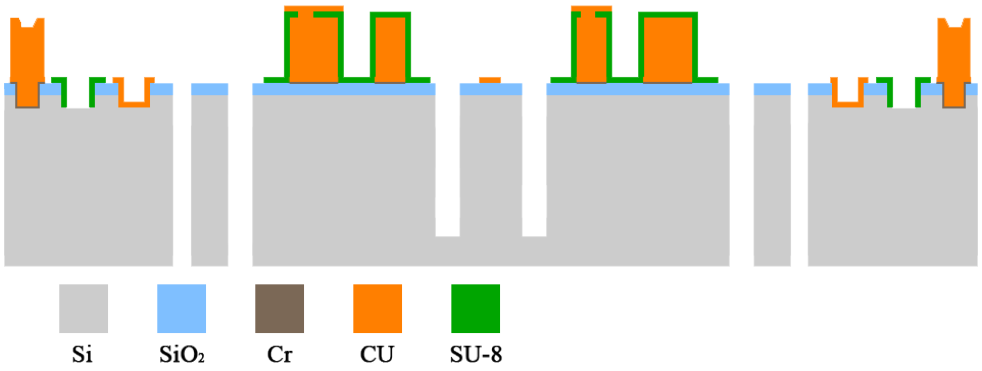


(q) The PR mask is removed in acetone

Figure 4.8: Designed fabrication flow process. Continued

## 4.3 Stator masks design process

Five masks were designed for these processes initially; however, one of them re-designed laterin middle of the fabrication to simplify the device structure at the expense of performance in order to demonstrate the first working device.The masks are designed in AutoCAD due to the complex pattern of the coils. Each mask is drawn in a separate layer in AutoCAD.

The first masks contain the outer frames and aligning marks. The alignment marks, which are used to align different mask patterns on the wafer during fabrication process, are designed to provide at least 5$\mu$m accuracy. The patterns are all made of drawing different polyline squares and rectangles.

The coils mask is the most complicated one. To obtain the coils pattern, first the smallest inner circle, which is tangential to the smallest inner arc, has been drawn and then using Offset command other inner circles are drawn. The same process is done for outer circles, which are tangential to outer arcs, as well. To draw the radial parts, one of the radii of largest circle is drawn and by employing the 'Array' command 1200 radii are drawn in 360°. Afterwards, by means of the 'Trim' command the radii are cut in which the first radius starts from the smallest inner circle to the smallest outer circle and the last radius on one pole of stator coils begins from the largest inner circle to the largest outer circle. By means of the 'Mirror' command the radii of

neighbor pole can be drawn. Next, the inner and outer connections along with radial lines are drawn as the 'Polylines' for a pair of poles. Finally, the drawn Polylines are being arrayed in 360°.

The other masks have much more simple patterns than the coils mask. In all other masks, first the patterns are drawn and finally different regions are being converted to polylines. It is important to ensure high accurate and error-free drawings are provided. All five masks are depicted through Figures 4.9 to 4.13.

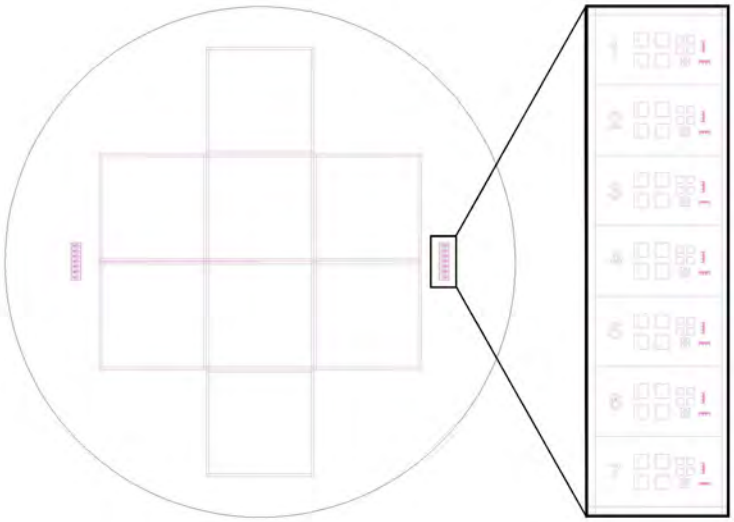

Figure 4.9: The layout of the 1st mask, which contains patterns of the stators' outer frame and alignment marks. Features are clear.

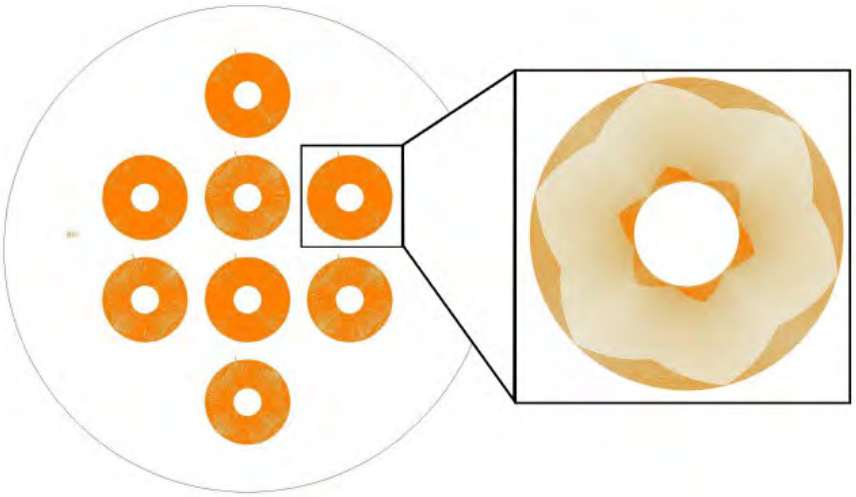

Figure 4.10: The layout of the 2nd mask, which contains patterns of the coils. Features are clear.

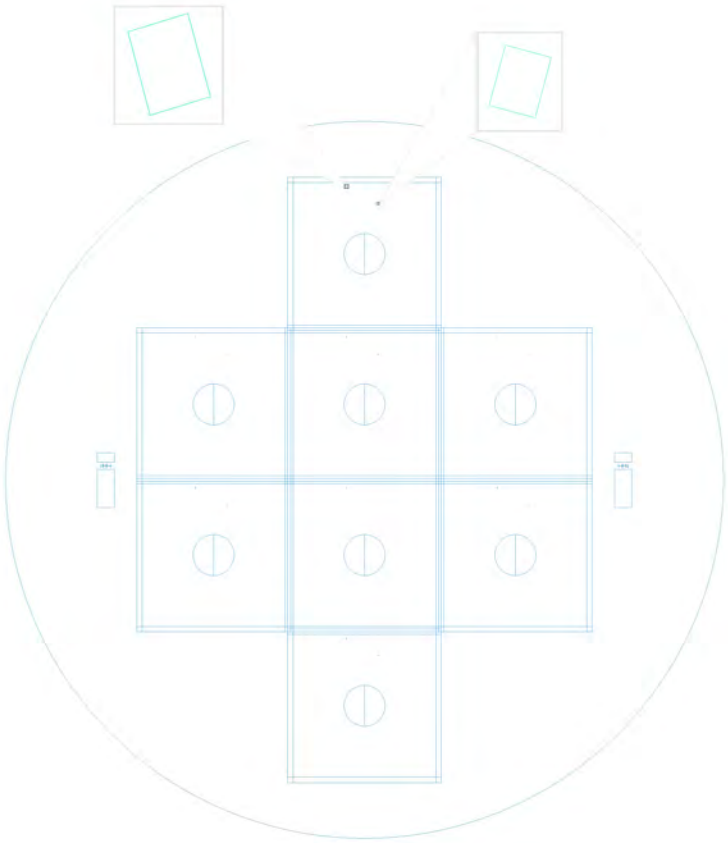

Figure 4.11: The layout of the 3rd mask, which is pattern of the insulation layer. Features are dark.

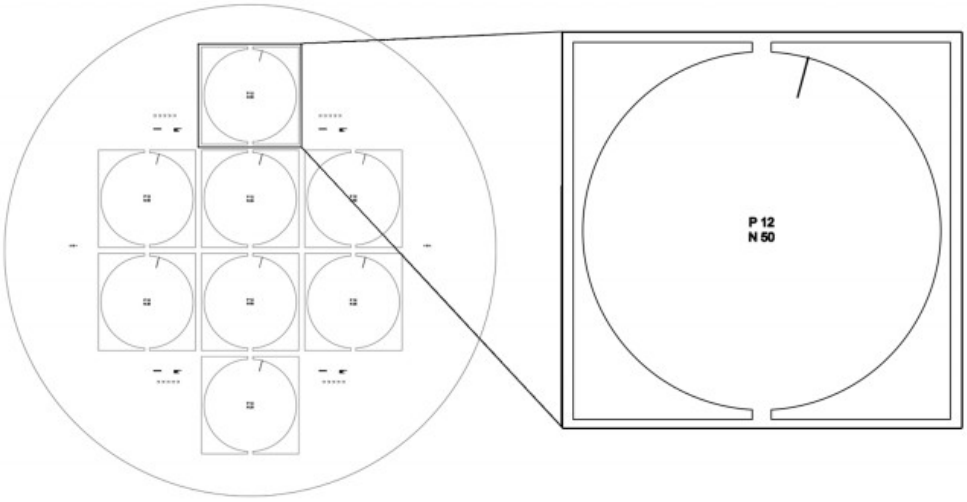


Figure 4.12: The layout of the 4th mask, which contains the patterns of the electrical pads and devices names.

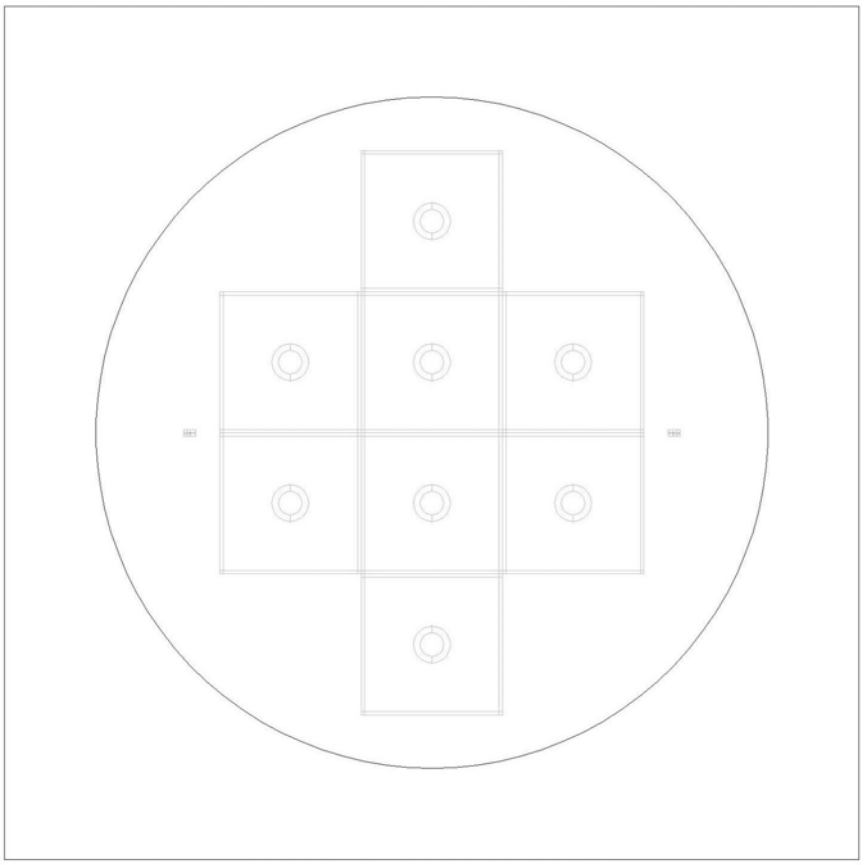

Figure 4.13: The layout of the 5th mask, which contains the patterns of the ball grooves and stators' outer frames.

## 4.4 Alignment marks and stators' outer frame patterning

The process starts with patterning a positive photoresist layer on top of the SiO2 using the 1st mask. The patterned photoresist would act as a mask for wet etching of the SiO2 layer which will be then etched in a 7:1 volumetric mixture of hydrofluoric acid (HF) and ammonium fluoride ($NH_4F$). The silicon substrate is then dry-etched to a depth of $50\mu m$ using DRIE.The patterned SiO2 layer and photoresistare used as the etch-mask during DRIE.Whilst using DRIE at this step was planned to eliminate dicing the stators at the end, this step later modified as discussed towards the end of this section.

Although the process seems to be very straightforward, many problems occurred during each step that we dealt with. First of all AZ5214, the most common photoresist in

the lab, was used as the etch mask; however, its stability inside the buffered HF was insufficient and large scale resist peeling was observed after 15 min etching.

### 4.4.1 Challenges with lithography

In order to etch $2\mu m$ SiO2 the wafer needs to remain in BOE for about 35 to 40 minutes, therefore a thicker photoresist had to be used. Since at the beginning the only available thick photoresist was AZ4562, it was chosen as the masking layer for wet etching. Although it had a very good adhesion during etching process, the problem with this photoresist was bubbles formation after exposure. By decreasing the exposure dose, using sloped softbaking method, and much longer softbaking period, bubble formation was minimized (see Figure 4.14).

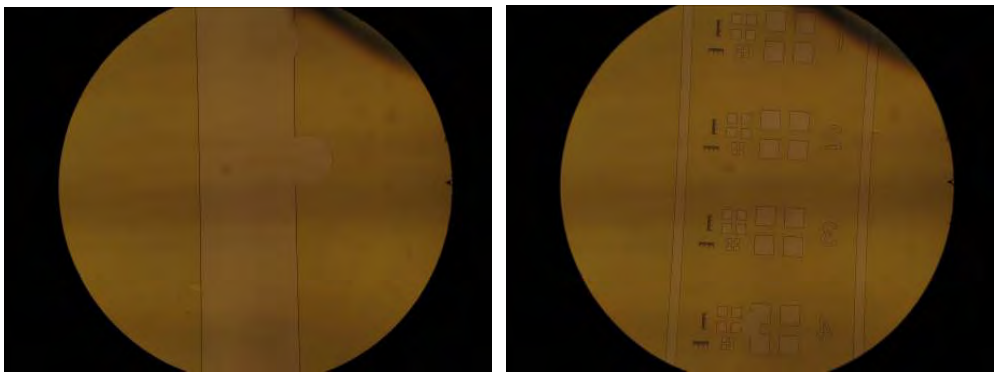

(a) (b)

Figure 4.14: Bubble formation after UV exposure

The AZ4562 was later replaced by AZ4533 photoresist. We again faced with a few bubbles formation, which was completely tolerated after lowering the exposure dose and extending the softbaking time. In addition, although at the beginning it was not adhesive enough during wet etching, a hardbake at $140^{\circ}C$ improved resist adhesion by further formation of chemical bonds between the resist and substrate (see Figure 4.15).

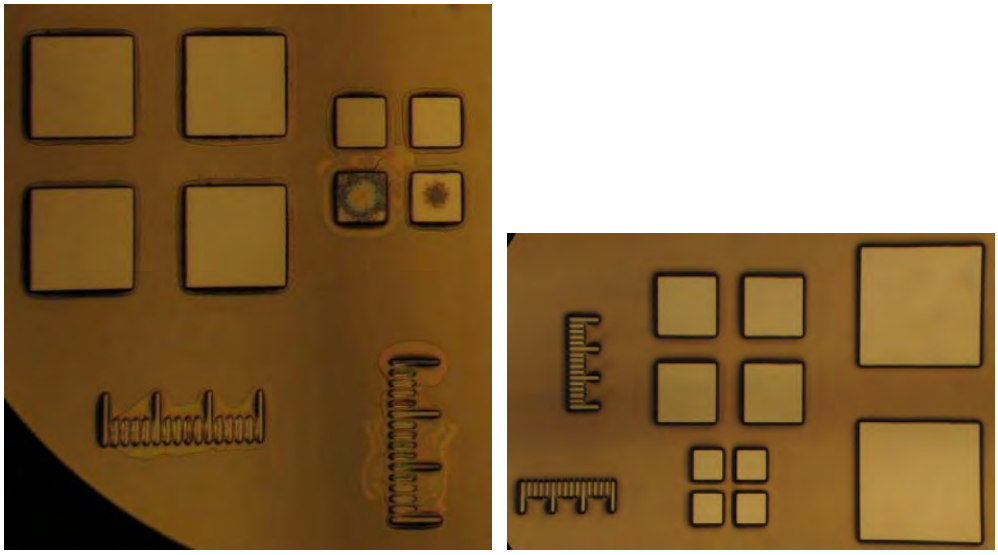

(a) (b)

Figure 4.15: Adhesion of the AZ4533 during wet etching a) without hard baking b) The PR is hardbaked at $140^{\circ C}$

### 4.4.2 Challenges with $SiO_2$ wet etching

It was also observed that to optimize the Buffered Oxide etching process, the BHF should be used between 22 to about 60 hours after preparation. In addition, to obtain a uniform etching the wafer should remain in the solution uninterruptedly until a complete etching.

### 4.4.3 Challenges with DRIE

Since DRIE at this step is being used only to easily separate the stators from the wafer, many DRIE etching features such as aspect ratio dependent etch (ARDE) rate, loading effect, and scalloping are not important. Nonetheless, as alignment marks are being etched in this step as well, minimum undercut was an issue which we dealt with it. The optimization process on chip scale showed that the observed undercut was due to imperfect bonding of chips to the carrier wafer. The imperfect bonding leads to weak cooling and since the passivation deposition rate is directly related to the wafer temperature, the sidewall passivation decreases and hence undercut increases. Consequently using no carrier wafer or perfect bonding overcame the problem (see

Figure 4.16).

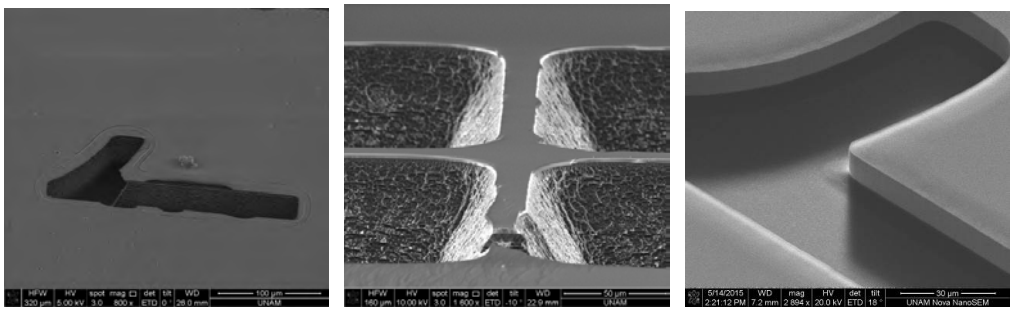

(a) (b) (c)

Figure 4.16: (Scanning Electron Microscopy) SEM image of DRIE results: In (a) and (b) huge undercut and positive profile angle is observed. c) Almost vertical sidewalls are observed after bonding optimization.

Due to the fact that the wafer thickness is $500\mu m$ and ball trenches along with outer frames were going to be etched for $450\mu m$ in the last fabrication step, by etching the outer frames for about $50 - 60\mu m$ at this step there would be needless to dice the stators at the end. But in the next generations ball grooves were decided to be etched for $300\mu m$. The plan was modified mostly because of DRIE variation in turbine etching process which led to having a deeper ball groove in turbines. Consequently, depth of the ball trenches in the stators should be reduced. Furthermore, the thicker the bottom of microball trenches is, the stronger it is, and so it will not break easily. Moreover, the etched stator frames made it difficult to deposit uniform photoresist during the next fabrication steps. Consequently, the first DRIE step was decided to be eliminated for the next generations.

**Coils deposition** Although the coils were planned to be electrodeposited copper with thickness of $20\mu m$, since the electroplating system at UNAM had not been installed yet, it was replaced with a 300nm-thick evaporated copper layer which is patterned using lift-off.

**Challenges with copper wet etching** Since wet etching was an alternative for patterning the evaporated copper that due to the lack of Cu etchant, Cr etchant was used as etching solution. The etching rate using pure Cr etchant was too high (280 nm/s)

along with non-uniform etching profile. Hence, to have a better control over etching process a diluted Cr etchant was used. Using 1:10 dilution of Cr etchant resulted in a slower and more uniform etching. However, non-uniformity problem was not perfectly solved and while some parts were not etched well, some copperwires got too narrow due to the huge undercut (see Figure 4.17).

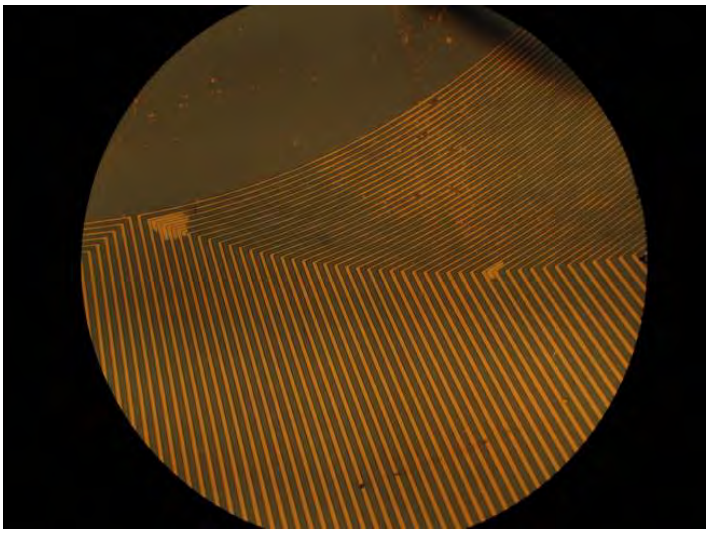

Figure 4.17: Illustration of non-uniform etching of Cu using Cr etchant.

### 4.4.4 Challenges with lift-off process

Due to the fact that the mask was designed for electroplating process, at first there was no choice but using positive photoresist (AZ4533) for lift-off process. In spite of depositing a very thin layer of Cu (150nm), because of using positive photoresist the lift-off was unsuccessful. Meanwhile, some lift-off trials using image reversal AZ5214 showed much better results. Therefore, we decided to write a new coils mask whose features would be compatible with negative photoresists. Although the written mask in UNAM had some issues due to the mask writer machine errors, until receiving the perfect written mask from US some more lift-off trials were done using the temporary mask. We observed that thermally evaporated copper does not possess good adhesion, whilst utilizing Cr and Ti as adhesion layer caused a worse result during the lift-off. This can be due to the high melting point of such metals that makes the resist profile start rounding and hence allow the metals to cover the resist profile side-walls as well. Consequently, the best lift-off result achieved by thermally

evaporated copper without using any adhesion layer and doing the lift-off so gently (see Figure 4.18).

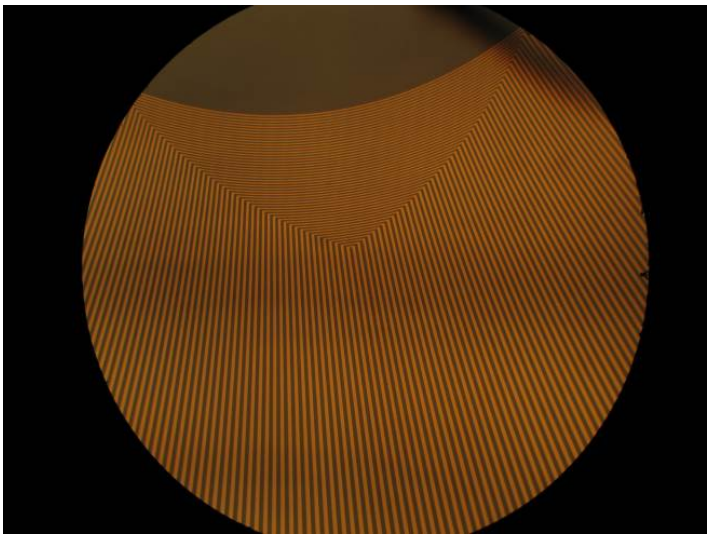

Figure 4.18: Lift-off result of 300nm-thick evaporated Cu

For next generations, we had access to Cr and Cu sources for sputtering machine and so we tried to deposit 20nm-thick Cr as adhesion layer followed by Cu deposition and do patterning by means of lift-off process. Although sputtering is not a sophisticated technique for lift-off, the result was good.It is most probably due to the deposition of thin metal layer (300 nm) along with strong adhesion (see Figure 4.19).

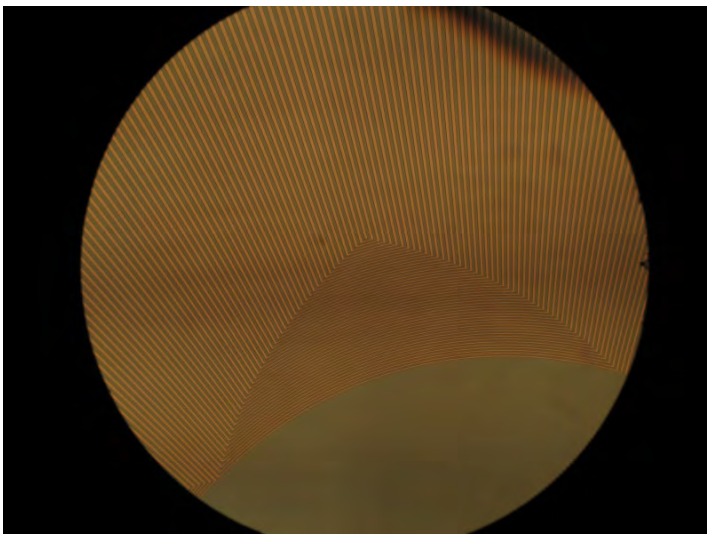

Figure 4.19: Lift-off result of 300nm-thick sputtered Cu. 20 nm-thick sputtered Cr is used as adhesion layer.

## 4.5 Insulator layer deposition

$5\mu m$ SU-8 3005 is used to provide the electrical isolation between the coils and electrical pads. What matters at this step is consideration of residue layer that could result in disconnection of electrical pads from coil ends. As a result, short $O_2$ plasma following with a very thin Cu etching is used. The $O_2$ plasma removes any possible SU-8 residue and wet etching etches a few nm of Cu to assure no copper oxide exist due to the $O_2$ plasma (see Figure 4.20).

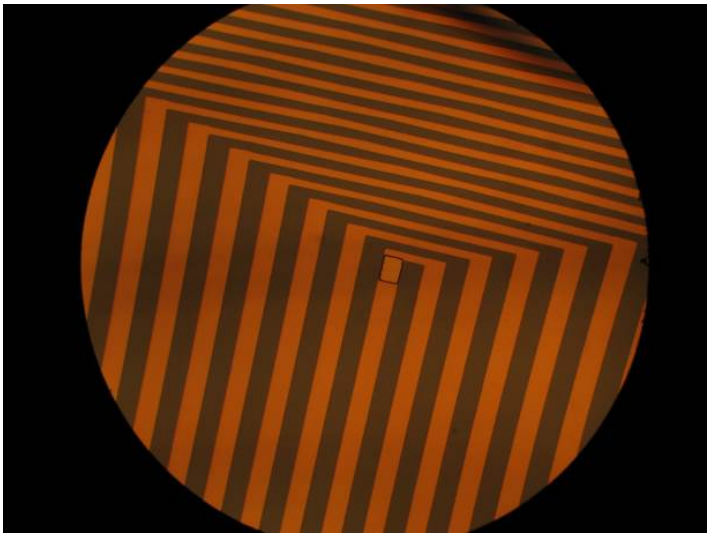

Figure 4.20: SU-8 lithography, which is covered everywhere on top of the coils except two rectangles on two ends of the coil.

## 4.6 Electrical pads connection

This step includes deposition of pad-layer metals following with patterning the pad structure. The copper pads at first were deposited using thermal evaporator and patterned through wet etching. Although we had not observed any problem during chip scale trials, in wafer scale experiments we faced with loose connection issue between the pads and coils ends. Optimization of SU-8 lithography to obtain vertical sidewalls, thinning the SU-8, and deposition of a thicker copper were considered to address the problem. To achieve vertical sidewalls using a long pass filter is highly recommended to eliminate UV radiation below 350 nm.However, since no filter was available in the

lab, exposure dose was almost the only effective parameter we could change. In addition, deposition of copper with thickness of more than 600nm resulted in adhesion problem on top of the SU-8 due to the occurrence of higher stress in deposited film (see Figure 4.21).

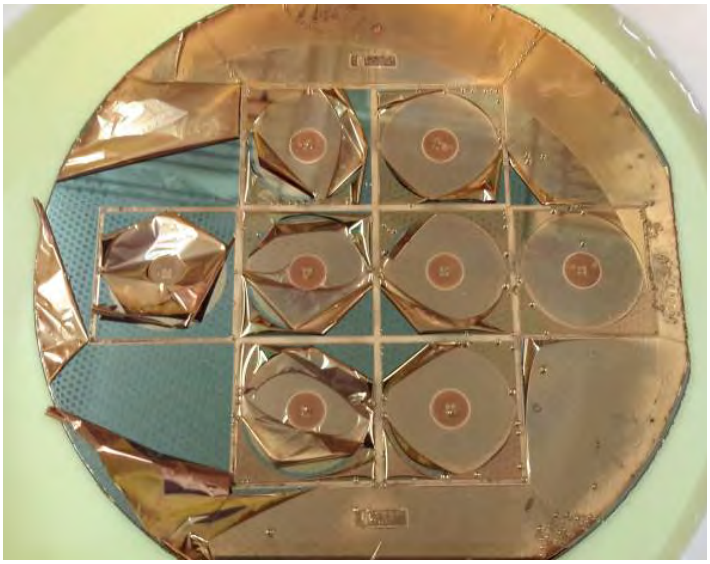

Figure 4.21: The adhesion loss of 700nm-thick evaporated Cu on top of the SU-8 during wet etching in Cr echant.

Accessing to the Cr and Cu sources for sputter machine resolved the loos connection issue; however, then we had to tackle with the patterning step. In spite of the fact that patterning the thermally evaporated copper pads could be easily done using Cr etchant, wet etching process of 500nm-thick sputter-coated layer of Cr and Cu became much slower along with appearance of huge non-uniform etching (see Figure 4.22).

We later found that this happens in case of existence of chromium as adhesion layer. As an alternative we could use Al etchant to etch the copper following with Cr etchant to etch the chromium layer. Nonetheless, to prevent any unexpected issues, lift-off technique was tried for patterning the deposited metals which led to a perfect patterning (see Figure 4.23).

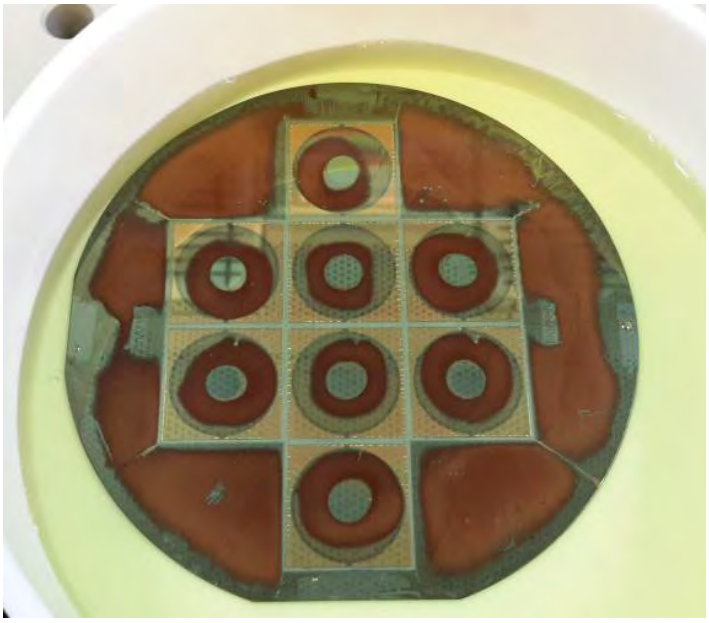

Figure 4.22: Illustration of the non-uniform sputtered Cr and Cu wet etching.

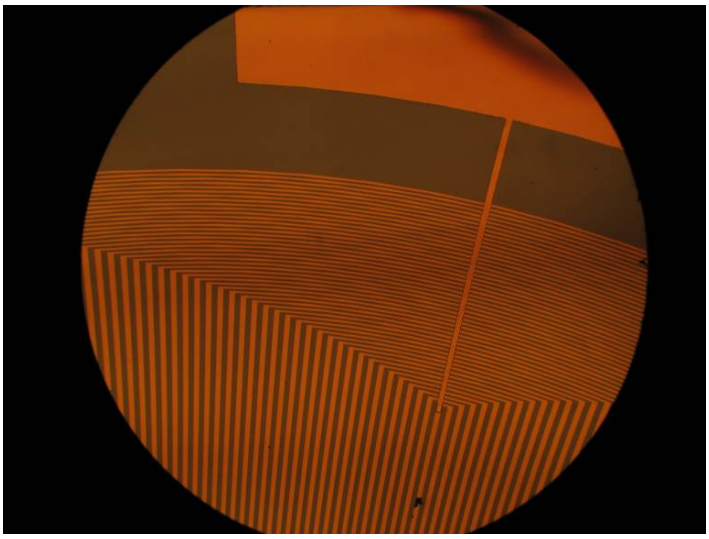

Figure 4.23: Illustration of lifted-off sputtered Cu pads.

## 4.7 Ball grooves etching

Finally, the last step is patterning the ball trenches. As mentioned before, first the ball grooves were decided to be etched for $450\mu m$ and then modified to $300\mu m$. Through-etching of the silicon substrate is performed by DRIE. Since a good DRIE recipe had been found during 1st fabrication step, for $450\mu m$ etching we mostly focused on masking layer. A thick photoresist layer is being used as the etch mask. At the

beginning, $10\mu m$ thick AZ4562 photoresist was successfully used as masking layer for DRIE tests. However, later due to the unavailability of AZ4562, it was replaced with 5$\mu$m AZ4533 which could not tolerate $450\mu m$ depth DRIE. Finally, AZ9260 photoresist was provided that enabled us to achieve $14\mu m$-thick photoresist in a single coat, which makes it a perfect etch mask (see Figure 4.24).

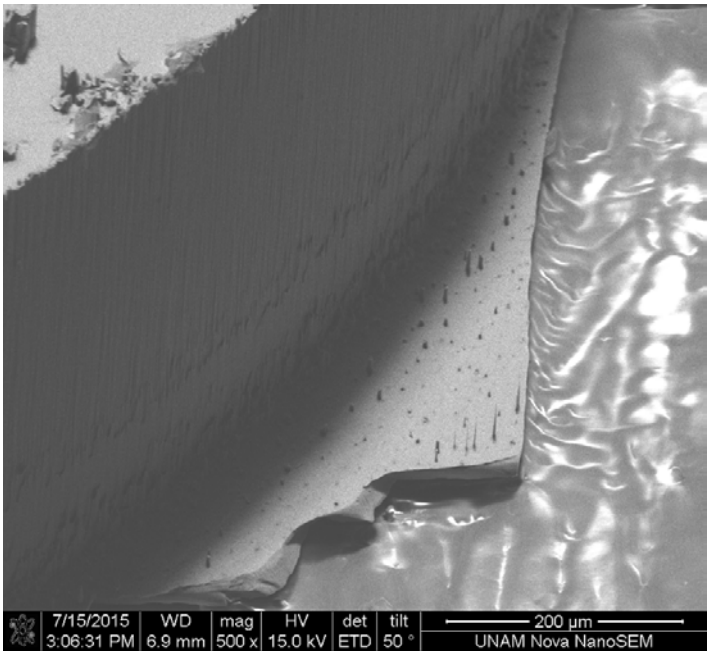


Figure 4.24: Illustration of $480\mu m$ DRIE etch of the stator outer frame.

Although sophisticated results were obtained during the tests, when we were going to etch the main devices after a few months, we faced with new issues. Not only the etch rate was different in the same patterns but different parts of the wafer, also about $50\mu m$ grass is observed (see Figure 4.25).

## 4.8 Summary and suggestions

This chapter presented the fabrication of the MEMS stators and several of its complications. The selected fabrication processes are the both bulk and surface micromachining. A comprehensive overview of each step of the micromachining processes are provided, including the designed process flows, encountered problems, and the final solutions.

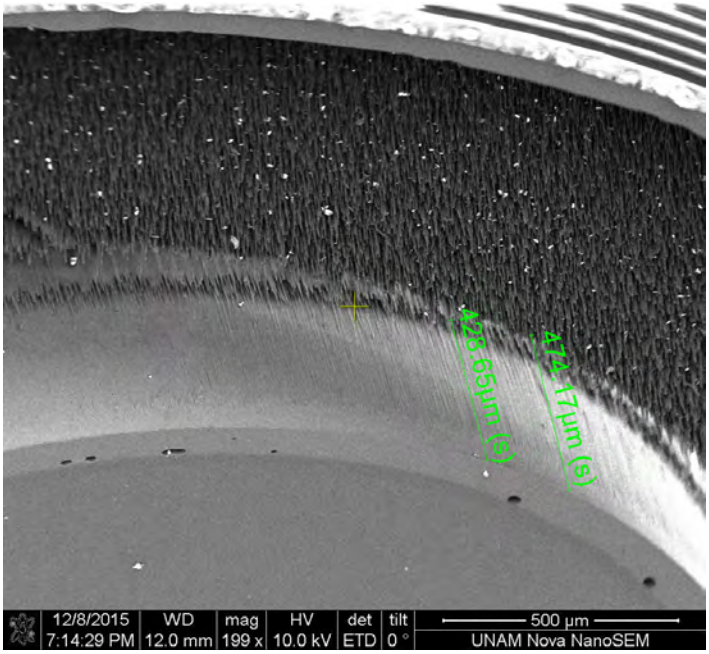


Figure 4.25: SEM image of the grassing at the bottom of the DRIE etched ball trench.

The fabricated stators have a 300nm-thick copper coils, which are covered with a $5\mu m$-thick SU-8 as the insulation layer. The insulation layer includes two rectangular openings on the two end of the coils, where the 500nm-thick electrical pad layers are connected to the coils. A 300nm-depth circular shape trench is etched through the stators to contain the microballs. The summary of the performed fabrication is illustrated in Figure 4.26.

(a) The PR is patterned by through 1st mask.

(b) The SiO2 is patterned using wet etching.

Figure 4.26: Fabrication flow of the stator.

(c) The alignment marks and stator's outer frames are etched using DRIE.

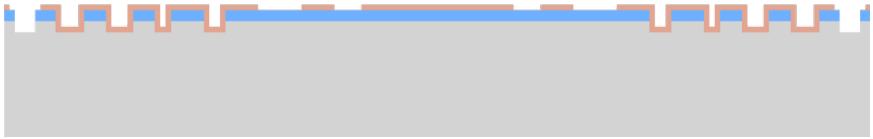

(d) A layer of PR is patterned through coils mask.

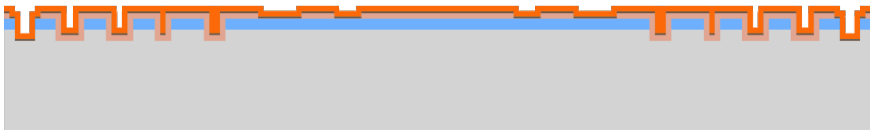

(e) Thin layer of Cr and Cu are deposited on top.

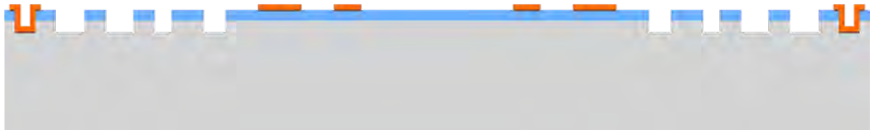

(f) The metal layers are patterned through lift-off.

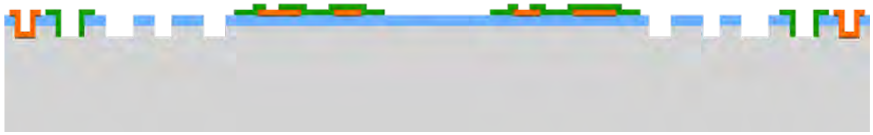

(g) SU-8 lithography is performed through the 3rd mask.

(h) PR layer is patterned through electrical pads mask.

(i) Cr and Cu are deposited on top.

Figure 4.26: Continued

(j) the metal layers are patterned via lift-off.

(k) Thick layer of PR is deposited and patterned through 5th mask.

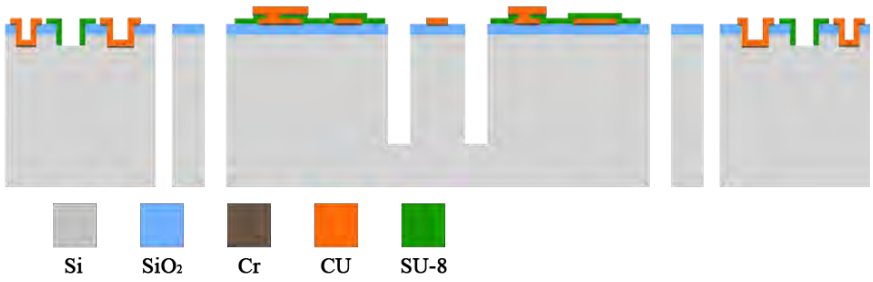


(l) Ball grooves and stators outer frame are etched using DRIE.

Figure 4.26: Fabrication flow of the stator. Continued

To address the grassing issue of the etched trenches at the last step, The DRIE process parameters need to be optimized. Considering previously studies, the grassing formation mostly occurs in large trenches and several parameters such as micromasking, passivation rate, platen power, $SF_6$ flow rate and etching cycle time. However, since in our study pre-cleaning was done during $SiO_2$ wet etching, micromasking cannot be the issue of grassing formation [68]. Due to the fact that insufficient etching radicals in etch step and too much passivation deposition can lead to the formation of grass at the bottom of etching, increasing the platen power along with decreasing the passivation component by lowering the polymer flow, can minimize the grassing problem [69]. In addition, regarding the research conducted by [70], if the etch cycle time is less or more than an optimum amount, The grasses will be appeared at the bottom of the trench. That is why etch cycle time parameters are crucial for getting satisfactory DRIE results. Furthermore, they have obtained that amount of bottom silicon grass increases when the $SF_6$ flow rate is gradually increased.

# CHAPTER 5

# TEST AND RESULTS

This chapter presents the electrical characterization of the successfully fabricated microcoils. Furthermore, the sensitivity of the induced voltage with respect to the gas velocity is calculated.

As mentioned in the previous chapters, two design of micro coils are fabricated, which are 12 poles 50 turns per pole and 12 poles 25 turns per pole. The resistance and inductance of the coils have been tested for electrical power delivery. Experimental results are compared with the theoretical analysis and are discussed at the end of this chapter.

The resistances of both 25-turn and 50-turn microcoils were measured with a simple multimeter. Although there were some variations across the wafer, the coils resistances obtained as 3.9kΩ for 25-turn coils and 15.8kΩ for 50-turn coils. Based on theoretical calculations for 300nm-thick copper coils, the resistances of 25-turn and 50-turn coils were expected to be 2.9kΩ and 11.5kΩ respectively, which are lower than the measured values. One reason is the non-uniform metal deposition, which also resulted in resistance variations between the similar designed coils on the same wafer. Furthermore, the connections between the electrical pads and two ends of the coil, which expected to be very thin, are not included in calculations. In addition, copper oxidation and narrower copper coils caused by imperfect lithography can be considered as further reasons.

The inductance of the coils have been also measured using Probe Station. For 25-turn and 50-turn coils, the inductance of the coils are measured as 2.6mH and 10.3mH

respectively. Considering the maximum frequency of 1kHz, the maximum inductive reactance of the 25-turn and 50-turn coils ($X_L = 2\pi f L$) will be 16.33$\Omega$ and 64.71$\Omega$, which are negligible compared to the coil resistances. Therefore the coil equivalent circuit resulting from this analysis can be simplified, which is given in Figure 5.1.

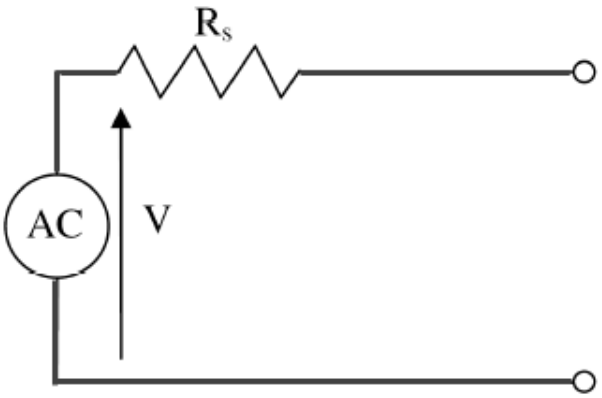


Figure 5.1: Equivalent circuit model for microcoil.

As discussed in Chapter 3, the maximum power generation will be obtained when $Z_L = Z^*_{coil}$. Considering the practical values, at $Z_L = R_{coil}$ and speed of 10krpm during normal breathing, the maximum output power will be 0.32mW and 0.34mW in 50-turn and 25-turn coil devices respectively. However, fabricating the coils using electroplating would lead to a much less coil resistance and so boost the output power to 30mW.

Goreke et al manufactured the plastic version of the turbines using CNC machine and speed performance of the different turbine designs with respect to the input flow rate were tested [26]. The rotational speed of the designed turbines versus volumetric flow rate was plotted in Figure 5.2.

Afterwards, using eq. 3.5 the induced voltage amplitude with respect to the input gas velocity is calculated and obtained graph is shown in Figure 5.3.

As can be seen in Figure 5.3, there is a linear relation the flow rate and induced voltage that results in sensor linearity. Moreover, the sensitivity of device, which is the ratio of output voltage for a unit flow rate, is obtained as 0.2 V/L/min in 50-turn coil and 0.1 V/L/min in 25-turn coil.

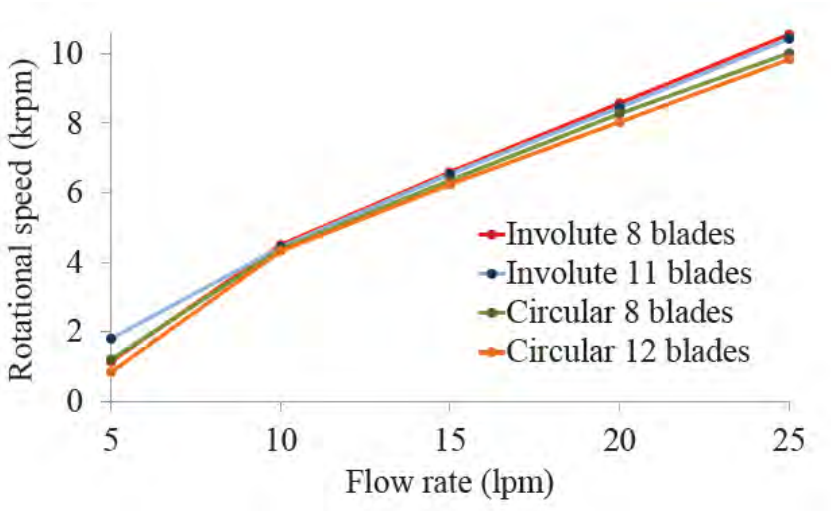


Figure 5.2: Rotational speed vs flow rate for different turbine designs [26].

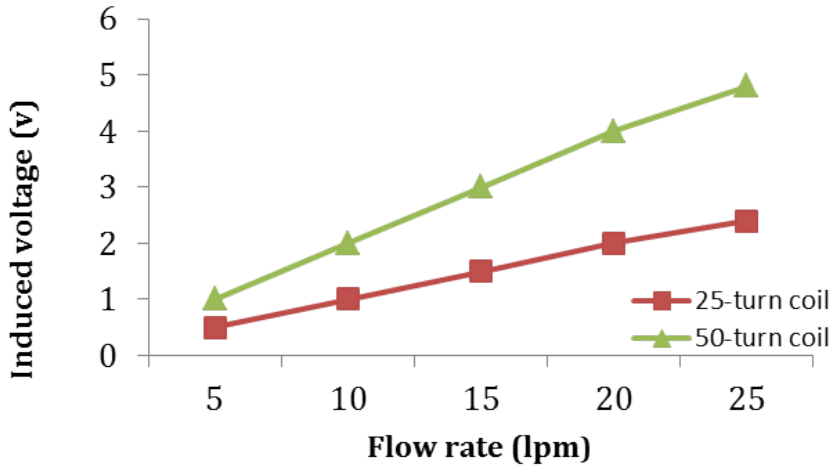


Figure 5.3: induced voltage vs flow rate for different coil designs.

In order to find the spirometric curves, the volumetric flow can be easily obtained by multiplying the flow rate by tube cross sectional area. Consequently, the volume-time and flow-volume curves can be achieved.

Although the calculated values are based on the test results of the plastic turbine, we expected to archive enhanced performance using microfabricated turbines. This is due to the fact that the turbines were manufactured using CNC milling on PMMA with $\pm 50 \mu$m precision. Since the CNC was not able to perform backside alignment, the microballs trench has been only etched on one side of the turbine. Consequently, the gap between the inner package surface and one side of the turbine is higher than

that of the other sides. This reduces the efficient flow of the fluid inside the package that results in less efficient collision between the fluid and turbine blades. Furthermore, using MEMS technology would boost the manufacturing precision from $\pm 50\mu$m to less than $\pm 5\mu$m. Besides micromachined turbines will have a smoother surface, which results in a lower friction. On the other hand, magnets were not embedded in the PMMA turbines so that the tests were carried out using lighter turbines; however, the mentioned advantages of microfabricated turbines are believed to overcome this issue and show a better performance.

# CHAPTER 6

# SUMMARY, CONCLUSIONS AND FUTURE WORKS

## 6.1 Summary

Based on WHO estimates, there is a significant number of patients suffering from asthma and COPD worldwide. These statistics demonstrate a high demand for facilities to help remote monitoring of patients in a more efficient way. Spirometers, are known as the most popular tools in diagnosing and following the progress of the lung diseases. Various types of spirometeres are available in the market, in which the turbine based spirometer sensors benefits from all the advantages of insensitivity to ambient pressure, temperature, humidity, and gas particles. This study aims to achieve the first turbine based MEMS spirometer sensor with the capability of utilizing human breath to repower itself.

The research done during this study can be summarized as:

- Several designs of plannar microcoils are investigated and gear-shaped design is selected as the coils pattern. Two different coils are designed, which are 12 poles 25 turns per pole and 12 poles 50 turns per pole microcoils.
- The poles number and magnets dimentions are optimized for the geometry of our device. The magnets are designed as ring shaped with 4mm and 7.25mm inner and outer radius respectively. Also number of poles is set to be 12.
- The microfabrication of the stators was performed during the 5-mask micromachining process, which includes DRIE etch of alignment marks, deposition of copper microcoils, insulation layer deposition, electrical pads deposition, and

DRIE etching of microball trenches. However, the bottom of the DRIE etched ball grooves contains grass and needs further optimizations.

- The performance of successfully deposited coils are tested. In addition, tests using PMMA manufactured designed turbines have been provided the information of the speed of turbines in respect with the flow rate which enables to calculate the induced voltage and maximum delivery power of the device. The obtained data are illustrated in Table 6.1.

Table 6.1: Summerized of achieved device performance values.

| | Coil resistance $(k\Omega)$ | Coil inductance $(mH)$ | Max delivered power $(mW)$ | Sensitivity $(v/lmp)$ |
|---|---|---|---|---|
| 12 pole 50-turn coil | 15.8 | 10.3 | 0.34 | 0.2 |
| 12 pole 25-turn coil | 3.9 | 2.6 | 0.32 | 0.1 |

## 6.2 Future work

The microfabrication of the stators was one of the most challenging aspects of this work due to the lack of pre-experience and frequent microfabrication tool breakdowns. Although the fabrication of the device is not completely done, the obtained results shows that this design has a strong potential to be used as spirometer sensor. In our study, in order to achieve the first working device, in some cases the design and fabrication were simplified. The future generations of the micromachined sensorr can be developed by building upon this work to improve the mechanical and electrical performance. Fabricating electroplated and multi-layer coils are such cases.

# REFERENCES


[1] V Lopata, Son-Cheol Yu, M ElShabbah, and I Myasnyi. On the spirometry and spirometers standardization. In *Electronics and Nanotechnology (ELNANO), 2013 IEEE XXXIII International Scientific Conference*, pages 316–318. IEEE, 2013.

[2] CDC. Respiratory health spirometry procedures manual, 2008. URL `http://www.cdc.gov/nchs/data/nhanes/nhanes_07_08/spirometry.pdf`. [Last accessed on 2016-02-10].

[3] John E Hall. *Guyton and Hall textbook of medical physiology*. Elsevier Health Sciences, 2010.

[4] CDC. Chronic obstructive pulmonary disease, 2015. URL `http://www.cdc.gov/copd/index.html`. [Last accessed on 2016-02-10].

[5] British lung foundation. Causes of asthma, 2008. URL `https://www.blf.org.uk/support-for-you/asthma/causes`. [Last accessed on 2014-03-10].

[6] Rolf M Schlegelmilch and Rüdiger Kramme. Pulmonary function testing. In *Springer Handbook of Medical Technology*, pages 95–117. Springer, 2011.

[7] Raghbir Singh Khandpur. *Handbook of biomedical instrumentation*. Tata McGraw-Hill Education, 1992.

[8] Interactive Learning Toolkit. Instrumentation for mechanics of breathing, 2013. URL `https://galileo.seas.harvard.edu/images/material/3794/1321/InstrumentationforMechanicsofbreathing.pdf`. [Last accessed on 2016-02-10].

[9] M Laghrouche, L Montes, J Boussey, and S Ameur. Low-cost embedded

spirometer based on micro machined polycrystalline thin film. *Flow Measurement and Instrumentation*, 22(2):126–130, 2011.

[10] QZ Wei, R Zhu, RY Que, and Z Cao. Hybrid system for airspeed measurement using dual mems sensors. In *Nano/Micro Engineered and Molecular Systems (NEMS), 2011 IEEE International Conference on*, pages 1224–1228. IEEE, 2011.

[11] PFTBlog. Pneumotach accuracy, 2014. URL `http://www.pftforum.com/blog/pneumotach-accuracy/`. [Last accessed on 2016-02-10].

[12] engineeringtoolbox. Types of fluid flow meters, 2010. URL `http://www.engineeringtoolbox.com/flow-meters-d_493.html`. [Last accessed on 2016-02-10].

[13] Riccardo Carta, David Turgis, Bart Hermans, Philippe Jourand, R Onclin, and Robert Puers. A differential pressure approach to spirometry. In *Biomedical Circuits and Systems Conference, 2007. BIOCAS 2007. IEEE*, pages 5–8. IEEE, 2007.

[14] NG Mandal. Respirometers including spirometer, pneumotachograph and peak flow meter. *Anaesthesia & intensive care medicine*, 7(1):1–5, 2006.

[15] Niklas Svedin, Erik Stemme, and Göran Stemme. A static turbine flow meter with a micromachined silicon torque sensor. *Microelectromechanical Systems, Journal of*, 12(6):937–946, 2003.

[16] W Blumenfeld, SZ Turney, and RJ Denman. A coaxial ultrasonic pneumotachometer. *Medical and biological engineering*, 13(6):855–860, 1975.

[17] David I. Plaut and J.G. Webster. Ultrasonic measurement of respiratory flow. *Biomedical Engineering, IEEE Transactions on*, BME-27(10):549–558, Oct 1980. ISSN 0018-9294. doi: 10.1109/TBME.1980.326576.

[18] Pawel Jalocha. Vortex flow meters, 2015. URL `https://indico.cern.ch/event/287285/contribution/1/attachments/534381/736801/PawelJalocha_Hamburg_30jun2014.pdf`. [Last accessed on 2015-03-4].

[19] H Nakesch et al. Alternative sensor principles for the detection of human respiration using amorphous ferromagnetic materials. In *Engineering in Medicine and Biology Society, 1995 and 14th Conference of the Biomedical Engineering Society of India. An International Meeting, Proceedings of the First Regional Conference., IEEE*, pages 1–17. IEEE, 1995.

[20] Chia-Ling Wei, Chien-Fu Lin, and I-Ta Tseng. A novel mems respiratory flow sensor. *Sensors Journal, IEEE*, 10(1):16–18, 2010.

[21] KS Rabbani, Suravi Islam, and Shumon Alam. A novel gas flow sensor based on sound generated by turbulence [and spirometry application]. In *Instrumentation and Measurement Technology Conference, 1997. IMTC/97. Proceedings. Sensing, Processing, Networking., IEEE*, volume 2, pages 1386–1388. IEEE, 1997.

[22] Shuhui Wang, Zwe-Lee Gaing, Raul Garcia, Peter Chang, and Ci Chen. A self-power peak expiratory flow meter. In *Orange Technologies (ICOT), 2013 International Conference on*, pages 172–176. IEEE, 2013.

[23] David P Arnold, Sauparna Das, Jin-Woo Park, Iulica Zana, Jeffrey H Lang, and Mark G Allen. Microfabricated high-speed axial-flux multiwatt permanent-magnet generators&# 8212; part ii: Design, fabrication, and testing. *Microelectromechanical Systems, Journal of*, 15(5):1351–1363, 2006.

[24] CT Pan and YJ Chen. Application of low temperature co-fire ceramics on in-plane micro-generator. *Sensors and Actuators A: Physical*, 144(1):144–153, 2008.

[25] R Cordero, A Rivera, M Neuman, R Warrington, and E Romero. Micro-rotational electromagnetic generator for high speed applications. In *Micro Electro Mechanical Systems (MEMS), 2012 IEEE 25th International Conference on*, pages 1257–1260. IEEE, 2012.

[26] U. Goreke, S. Habibiabad, K. Azgin, Y.S. Dogrusoz, and M.I. Beyaz. The development and performance characterization of turbine prototypes for a mems spirometer. *Sensors Journal, IEEE*, 16(3):628–633, Feb 2016. ISSN 1530-437X. doi: 10.1109/JSEN.2015.2488104.

[27] Jonathan Lueke, Ahmed Badr, Edmond Lou, and Walied A Moussa. Microfabrication and integration of a sol-gel pzt folded spring energy harvester. *Sensors*, 15(6):12218–12241, 2015.

[28] Partnering with Australasia. Evaporative co2 cooling in silicon microchannels for the lhcb velo, 2015. URL `http://www.pwagroup.com.au/equipment/mass-flow-meters/vortex`. [Last accessed on 2015-03-4].

[29] The trembling uterus.

[30] Reza Ghodssi and Pinyen Lin. *MEMS materials and processes handbook*, volume 1. Springer Science & Business Media, 2011.

[31] M Ashauer, H Glosch, F Hedrich, N Hey, H Sandmaier, and W Lang. Thermal flow sensor for liquids and gases based on combinations of two principles. *Sensors and Actuators A: Physical*, 73(1):7–13, 1999.

[32] Guilherme AL Araujo, Raimundo Freire, José F Silva, Amauri Oliveira, and Emerson F Jaguaribe. Breathing flow measurement with constant temperature hot-wire anemometer for forced oscillations technique. In *Instrumentation and Measurement Technology Conference, 2004. IMTC 04. Proceedings of the 21st IEEE*, volume 1, pages 730–733. IEEE, 2004.

[33] John G Webster. Medical instrumentation-application and design. *Journal of Clinical Engineering*, 3(3):306, 1978.

[34] Alick Hobbes. A comparison of methods of calibrating the pneumotachograph. *British Journal of Anaesthesia*, 37(12):987–987, 1965.

[35] PJ Chowienczyk and CP Lawson. Pocket-sized device for measuring forced expiratory volume in one second and forced vital capacity. *BMJ*, 285(6334): 15–17, 1982.

[36] KamilYunus Özkaya and Mustafa İlker Beyaz. An investigation on the electromagnetic design optimization of rotary micromachines with double-layer permanent magnets. *Sensors and Actuators A: Physical*, 222:335–340, 2015.

[37] WHO. Chronic respiratory diseases, asthma, 2013. URL http://www.who.int/mediacentre/factsheets/fs307/en/. [Last accessed on 2016-02-10].

[38] Cope with asthma. What is a peak flow meter, 2010. URL http://www.copewithasthma.com/what-is-a-peak-flow-meter/. [Last accessed on 2016-03-4].

[39] Zuzana Šnajberková. Physiotherapy for bronchial asthma, 2014. URL https://www.google.com.tr/url?sa=i&rct=j&q=&esrc=s&source=images&cd=&ved=0ahUKEwi-zqCR8rLLAhVqAZoKHcMiDikQ5TUICQ&url=https%3A%2F%2Fis.cuni.cz%2Fwebapps%2Fzzp%2Fdownload%2F130127740&psig=AFQjCNHhaWDcJN6oVxzZmUm1utbnZJRHxg&ust=1457535044986202. [Last accessed on 2015-03-4].

[40] Martin R Miller, JATS Hankinson, V Brusasco, F Burgos, R Casaburi, A Coates, R Crapo, P Enright, CP Van der Grinten, P Gustafsson, et al. Standardisation of spirometry. *Eurrespir J*, 26(2):319–38, 2005.

[41] Peter Breen. Stand-alone circle circuit with co2 absorption and sensitive spirometry for measurement of pulmonary uptake, October 14 2003. US Patent App. 10/530,603.

[42] David M Shade. Design of respiratory devices in biomedical engineers' handbook. *McGraw-Hill*, 2003.

[43] welchallyn. Wa/schiller spirometry sales sheet, 2009. URL http://goo.gl/G2s50c. [Last accessed on 2016-02-10].

[44] MDSpiro. Simple screening spirometer, 2016. URL https://mdspiro.com/spirocheck-spirometer?search=SpiroCheck. [Last accessed on 2016-02-10].

[45] cardiacdirect.

[46] R Alejos-Palomares, J Manuel Ramirez Cortes, and N Domínguez-Martinez. Digital spirometer with labview interface. In *Electronics, Communications and*

*Computers, 2008. CONIELECOMP 2008, 18th International Conference on*, pages 105–110. IEEE, 2008.

[47] Vivek Agarwal and NCS Ramachandran. Design and development of a low-cost spirometer with an embedded web server. *International journal of biomedical engineering and technology*, 1(4):439–452, 2008.

[48] Jeremy Glynn, Jeremy Schaefer, Andrew Bremer, Andrew Dias, David Van Sickle, and Mitchell Tyler. Low-cost spirometer, 2009.

[49] Sergio Silvestri and Emiliano Schena. Micromachined flow sensors in biomedical applications. *Micromachines*, 3(2):225–243, 2012.

[50] Hans H Bruun. Hot-wire anemometry: principles and signal analysis. *Measurement Science and Technology*, 7(10):null, 1996.

[51] MA Ardekani and M Masoudi Motlagh. Ordinary hot-wire/hot-film method for spirography application. *Measurement*, 43(1):31–38, 2010.

[52] Adam Huang, James Lew, Yong Xu, Yu-Chong Tai, and Chih-Ming Ho. Microsensors and actuators for macrofluidic control. *Sensors Journal, IEEE*, 4(4): 494–502, 2004.

[53] Peng Liu, Rong Zhu, and Ruiyi Que. A flexible flow sensor system and its characteristics for fluid mechanics measurements. *Sensors*, 9(12):9533–9543, 2009.

[54] JJ Van Baar, RJ Wiegerink, TSJ Lammerink, GJM Krijnen, and M Elwenspoek. Micromachined structures for thermal measurements of fluid and flow parameters. *Journal of micromechanics and microengineering*, 11(4):311, 2001.

[55] Lidai Wang, Shenshu Xiong, and Zhaoying Zhou. Miniature airspeed meter based on mems pressure sensor. *QinghuaDaxueXuebao/Journal of Tsinghua University(China)*, 45(8):1066–1068, 2005.

[56] John Webster. *Medical instrumentation: application and design*. John Wiley & Sons, 2009.

[57] AFT Hobbes. A comparison of methods of calibrating the pneumotachograph. *British journal of anaesthesia*, 39(11):899–907, 1967.

[58] Luis Carretié, Jaime Iglesias, and Pedro Aguilar. Photoelectric-helicoidal spirometer. *Behavior Research Methods, Instruments, & Computers*, 29(4): 582–585, 1997.

[59] JL McShane. Ultrasonic flowmeters. In *Flow: Its measurement and control in science and industry*, volume 1, pages 897–915, 1974.

[60] Haya Hasan, Basel Safieh, Fadi Aloul, and Assim Sagahyroon. Diagnosing copd using mobile phones. 2015.

[61] Omar Yahya and Miad Faezipour. Automatic detection and classification of acoustic breathing cycles. In *American Society for Engineering Education (ASEE Zone 1), 2014 Zone 1 Conference of the*, pages 1–5. IEEE, 2014.

[62] Ahmad Abushakra and Miad Faezipour. Augmenting breath regulation using a mobile driven virtual reality therapy framework. *Biomedical and Health Informatics, IEEE Journal of*, 18(3):746–752, 2014.

[63] Ahmad Abushakra and Miad Faezipour. Lung capacity estimation through acoustic signal of breath. In *Bioinformatics & Bioengineering (BIBE), 2012 IEEE 12th International Conference on*, pages 386–391. IEEE, 2012.

[64] Andrew S Holmes, Guodong Hong, and Keith R Pullen. Axial-flux permanent magnet machines for micropower generation. *Microelectromechanical Systems, Journal of*, 14(1):54–62, 2005.

[65] S Das, DP Arnold, I Zana, JW Park, JH Lang, and MG Allen. Multi-watt electric power from a microfabricated permanent-magnet generator. In *Micro Electro Mechanical Systems, 2005. MEMS 2005. 18th IEEE International Conference on*, pages 287–290. IEEE, 2005.

[66] Mustafa Ilker Beyaz, B Hanrahan, J Feldman, and R Ghodssi. An integrated electromagnetic micro-turbo-generator supported on encapsulated microball bearings. In *Micro Electro Mechanical Systems (MEMS), 2012 IEEE 25th International Conference on*, pages 1209–1212. IEEE, 2012.

[67] Paul C-P Chao, CI Shao, CX Lu, and CK Sung. A new energy harvest system with a hula-hoop transformer, micro-generator and interface energy-harvesting circuit. *Microsystem technologies*, 17(5-7):1025–1036, 2011.

[68] P. Verdonck, M. Van Cauwenberghe, A. Phommahaxay, R.C. Teixeira, and N. Tutunjyan. Method for etching 3d structures in a semiconductor substrate, including surface preparation, 2010. URL https://www.google.com/patents/US20100216308. US Patent App. 12/711,544.

[69] Akın Aydemir. *Deep-trench RIE Optimization for High Performance MEMS Microsensors*. PhD thesis, Citeseer, 2007.

[70] Pradeep Dixit and Jianmin Miao. Effect of sf6 flow rate on the etched surface profile and bottom grass formation in deep reactive ion etching process. In *Journal of Physics: Conference Series*, volume 34, page 577. IOP Publishing, 2006.

# APPENDIX A

# DETAILED PROCESS TRAVELERS

- Photolithography with AZ4533 (4$\mu$m)
  - Cleaning:
    - Acetone 10 min
    - Isopropanol 5 min
  - Spin coating:
    - HMDS: 40 sec 4000 rpm 2000 rpm/sec
    - AZ4533: 30 sec 2000 rpm 1000 rpm/sec
  - Soft bake: 100°c 13 min
  - UV exposure: 110 mJ/cm2
  - Developer: AZ400K:Deionized water 1:4, 7 min
  - Hard bake: 140°c 5 min
- Photolithography with AZ5214 (1.4$\mu$m)
  - Cleaning:
    - Acetone 10 min
    - Isopropanol 5 min
  - Spin coating:
    - HMDS: 40 sec 4000 rpm 2000 rpm/sec
    - AZ5214: 40 sec 4000 rpm 2000 rpm/sec
  - Soft bake: 110°c 75 sec
  - UV exposure: 40 mJ/cm2

  - Developer: AZ400K:Deionized water 1:4, 40 se

- Photolithography with IR5214 (1.4$\mu$m)
  - Cleaning:
    * Acetone 10 min
    * Isopropanol 5 min
  - Spin coating: AZ5214: 40 sec 4000 rpm 2000 rpm/sec
  - Soft bake: 110°c 75 sec
  - UV exposure: 30 mJ/cm2
  - Reversal bake: 120°c 75 sec
  - Flood exposure: 250 mJ/cm2
  - Developer: AZ726 MIF 40 sec

- Photolithography with AZ9260 (15$\mu$m)
  - Cleaning:
    * Acetone 10 min
    * Isopropanol 5 min
  - Spin coating:
    * HMDS: 40 sec 4000 rpm 2000 rpm/sec
    * AZ9260:
      · 1st: 3 sec 300 rpm 1000 rpm/sec
      · 2nd: 80 sec 900 rpm 1500 rpm/sec
  - Soft bake: 110°c 8 min
  - UV exposure: 1500 mJ/cm2
  - Developer: AZ400K:Deionized water 1:4 8 min

- Photolithography with SU-8 3005 (5$\mu$m)
  - Cleaning:
    * Acetone 10 min
    * Isopropanol 5 min

  - Spin coating:
    * SU8:
      · 1st: 10 sec 500 rpm 100 rpm/sec
      · 2nd: 30 sec 4000 rpm 300 rpm/sec
  - Soft bake: 95°c 4 min
  - UV exposure: 150 mJ/cm2
  - Post exposure bake (PEB): 95°c 2 min
  - Developer: SU-8 developer 4 min
- Thermal Deposition of Cu
  - Pressure: 5$\mu$Torr
  - Tooling factor: 85
  - Deposition rate: 0.8 A°/sec
- Oxygen plasma:
  - O2 flow rate: 30 sccm
  - N2 flow rate: 5 sccm
  - power: 450 W
  - Duration: 15 min
  - chamber temperature: 30°c
  - substrate temperature: 30°c
- Deep Reactive Ion Etching
  - Etch cycle:
    * Gases: SF6: 125sccm, O2: 13sccm
    * Power: Coil: 600W, Platen: 20W
    * Cycle time: 10 seconds
  - Passivation cycle:
    * Gases: C4F8: 80 sccm
    * Power: Coil: 600W, Platen: 0W

        * Cycle time: 7 seconds

- Metal Sputtering (Cr and Cu):
    - Cr Deposition:
        * AC Power: 150W, Time: 20 min, Ar flow rate: 70 sccm, Pressure: 20mTorr
    - Cu Deposition:
        * DC Power: 150W, Time: 17 min, Ar flow rate: 50 sccm, Pressure: 20mTorr